NASA Contractor Report 182256

Experiment Plans to Study Preignition Processes of a Pool Fire in Low Gravity

David N. Schiller

University of California—Irvine
Irvine, California

March 1989

Prepared for
Lewis Research Center
Under Grant NAG3-627

National Aeronautics and
Space Administration

Contents

Table of Symbols

Gr	Grashof number.
Ma	Marangoni number.
Re	Reynolds number.
Pr	Prandtl number.
Eu	Euler number.
Ec	Eckert number.
β	Volume expansion coefficient.
g	Gravitational acceleration (or effective acceleration with respect to an accelerating frame of reference).
g	Gravitational acceleration at sea level (9.81 m/s^2).
L	Characteristic length (typically taken to be the radius of the test cell).
T_f	Maximum fuel temperature at the liquid surface.
T_o	Bulk temperature of the fluid.
T_h	Heater temperature.
ρ	Density of the fluid.
ν	Thermal diffusivity of the fluid.
α	Kinematic viscosity of the fluid.
σ	Surface-tension coefficient.
U	Reference velocity.
θ	Local angle of the liquid surface.
δ	Liquid surface deformation with respect to the height of the liquid in contact with the side walls.
ΔT	Temperature difference $T_h - T_o$.

Note: Many other symbols are used and defined in Chapter 6.

Acknowledgements

I would like to sincerely thank my committee members for assisting me in my work. Dr. Elghobashi always found time from his very demanding schedule to help me with my computer program. Without his patience, I would have certainly lost mine long ago. Dr. Edwards contributed great foresight into the future design of the experiments and provided several suggestions for improving the accuracy of both the experiment and the computational model. As for my advisor, Dr. Sirignano, I cannot give enough thanks for his wisdom, guidance, and support.

I would also like to thank Dr. Boris Abramzon for his work on this project before and after I came to U. C. Irvine. He contributed greatly to this Science Experiments Plan through his development of the computational model. I am very grateful to him for helping me understand both the physics and the modelling of the problem. I wish him luck and happiness in Israel.

Finally, this thesis was aided most of all by the work of Dr. Howard Ross at the NASA-Lewis Research Center. Dr. Ross leads the experimental effort at NASA and has been instrumental in designing and conducting the experiments. He has given me valuable feedback on my suggested science requirements and test plans. Dr. Ross also contributed the photographs shown in Chapter 7 and Appendix A.

I am deeply grateful for the financial support received from the Division of Graduate Studies and Research of the University of California at Irvine, under which I worked as a Research Assistant. I am also very grateful to the NASA-Lewis Research Center for their funding of this project.

Chapter 1

Introduction

The purpose of this document is to specify requirements to guide experimental studies of the fundamental behavior of a liquid pool fire prior to ignition. These specifications are provided for experiments in three separate settings: (a) a normal gravity laboratory; (b) the NASA-LeRC drop towers, and (c) a space-based laboratory (e.g., Shuttle, Space Station). A rationale is developed for both minimum and desired requirement levels. In general the requirements are most stringent in the normal gravity experiments.

In Chapter 2, the scientific problem is described with the intention of justifying the need for low gravity experimentation. Chapter 3 identifies the test matrix and measurement requirements for each experimental setting. Chapter 4 provides a typical operational sequence for the experiments. The planned data analysis is described in Chapter 5. Preliminary hardware concepts are described in Appendix A. The numerical model is described in Chapter 6, which also includes the governing equations and source term approximations used in the code. Preliminary numerical and experimental results are then given in Chapter 7.

All experiments in this document are intended to collect scientific data. The requirements specified herein will be reviewed and updated periodically (e.g., annually) as appropriate.

Chapter 2

Summary of the Science

2.1 Background

Fire safety problems of ignition and flame spread above a pool of liquid fuel arise in many accident situations where liquid fuel spills in the vicinity of hot ignition sources. Another prototypical hazard situation might be the rupture of a fuel tank when hot engine parts or exhaust gases may appear in close proximity of liquid fuel. Heat and mass transport which control ignition delay and flame spread rates are complicated by multiple energy and mass transport processes, phase change, and chemical reaction. It is believed that reduced gravity will remove or isolate some of these complications. However, the scientific literature is devoid of experimental study of these characteristics under conditions of reduced gravity.

The literature of liquid pool burning theory has for the most part neglected the gas and liquid phase coupling, and concerned itself solely with liquid motion. However, the most interesting scientific situation (and one of very practical importance) involves not-so-volatile fuels whereby the coupling between the liquid and gas phases is of critical importance. That is, heat from the gas phase is required to vaporize some portion of the liquid fuel in order to provide a combustible mixture

in the gas phase. Convective heat and mass transport between the liquid and gas phases is critical and often dominant during the preignition period. Other modes of heat transfer, such as thermal radiation from the ignition source, may also play a very important role in the liquid heating. Temperature gradients in the gas and liquid phases, as well as concentration gradients in the gas mixture, create natural convection currents. Temperature gradients in the liquid surface initiate "surface-tension-driven convection" which can be a critical factor in the ignition delay and flame spread phenomenon. On account of nonuniform heating from above due to the ignition source or the flame, liquid motion will be driven by both surface-tension gradients and by buoyancy. These driving forces generally support in concert surface fluid motion away from the heat source. Therefore this motion tends to delay ignition as heat from the source is convected rather than concentrated. On the other hand, the motion supports flame spread as the convection assists the preheating process ahead of the flame. The gravity effect on ignition and flame spread is, in general, opposite to that of surface tension. As gravity decreases, the fluid mixing due to natural convection in both phases is retarded and the liquid at the surface is heated and vaporized more rapidly. Therefore the reduction in gravity should lead to shorter ignition delay and slower flame spread. However, the final result depends on the relative strengths of buoyancy versus surface tension. Surface-tension effects will tend to dominate over buoyancy at reduced gravity and smaller characteristic lengths. It is obvious, therefore, that the magnitude of the gravitational acceleration is one of the most important parameters that can be studied.

In order to understand the physical phenomena involved in ignition and flame spread, W. Sirignano et al., under NASA/OSSA sponsorship, developed a computational code which has been used to study the preignition motion of a deep liquid

fuel pool in an enclosed container heated unevenly from above. The key findings of the research are contained in References [1] and [2]. If the effect of radiation is not considered, then as the Grashof number decreases (or as the gravity force diminishes) the number of circulatory cells and the maximum value of the velocity in both the liquid and the gas phase decrease markedly. The convective heat transfer dominates conduction and the buoyancy-driving of the flow is greater than the surface-tension effect at high Grashof numbers (higher than 10^6). At lower Grashof numbers (10^3 and less) conduction is dominant. Surface tension dominates buoyancy in inducing liquid motion at lower Grashof numbers, but this motion is itself not as important as gas phase conduction. These conclusions apply to pools of depths comparable to their widths. It is expected that surface tension will be more important in shallow pools. Radiation and thermal inertia of the walls were shown to produce significant quantitative modifications. An important qualitative difference is that as the container walls are heated by radiation from the primary heat source, strong natural convection currents are initiated near these hot surfaces. The circulatory cells nearest the primary source need not be the strongest vortical structures when buoyancy is present.

The geometry of the problem is shown on Figure 2.1. The initially quiescent fluid in the container consists of two phases: liquid and gas. A constant-temperature[1] heater surrounded by a water-cooled jacket provides nonuniform heating from above. Once heating begins, the response of the system in terms of velocity and temperature is simulated at 400 node points (or 1600 node points using the CRAY computer) in both the gas and liquid phases. The effects of gravity are accounted for by varying

[1]The heater actually need not be exactly constant temperature as long as the radial temperature profile of the heater is known.

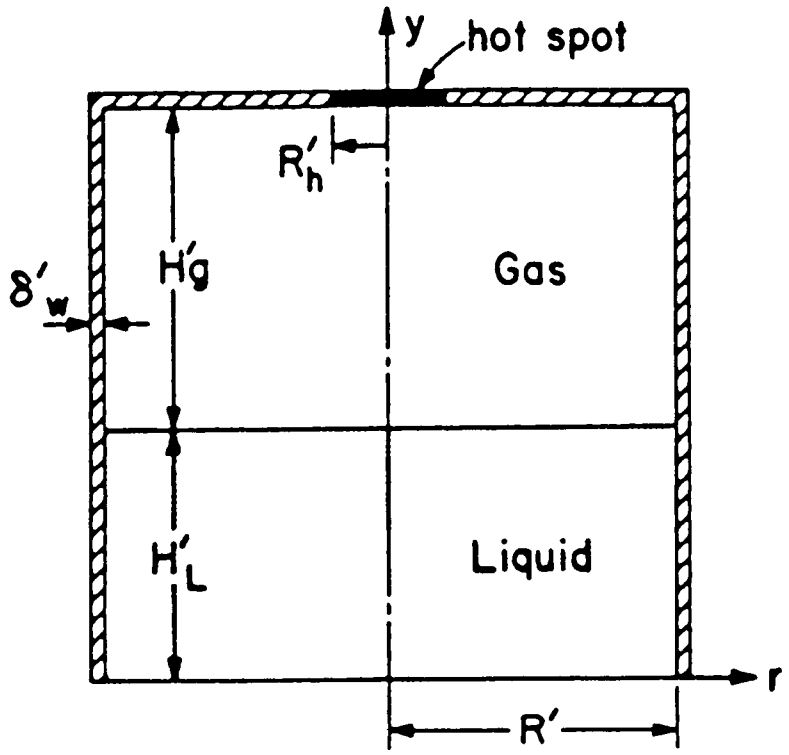

Figure 2.1: Geometry of the problem (taken from Reference [1]).

the Grashof number. Because the prediction of the liquid-vapor interfacial shape is complex, the model presently considers only a flat liquid-vapor interface. Thus, as discussed later, provisions must be made in designing reduced gravity experiments to maintain a flat liquid-vapor interface.

The general philosophy of the computational effort has been to simulate the more tractable aspects of the problem initially, and to increase the complexity of the computer program in small steps to approach the real case. First, heat transport in a one-phase fluid within an enclosure was studied using the Los Alamos SOLA code [2]. This code was modified to account for natural convection. Then, transient natural convection in a two-layer gas-and-liquid system without surface tension

was studied. Next, surface-tension effects were added. In the fourth iteration, radiation was added. Inclusion of radiation effects caused the necessity of revision of the thermal boundary condition at the walls of the container. Thus, the effects of thermal inertia and one-dimensional conduction along the walls were added. The following steps in the research were to include the effects of variable properties in the gas and liquid phases, evaporation and mass transfer, and two-dimensional thermal conduction along the walls. This task, however, required a complete change of the numerical approach and the computer code. The incompressible SOLA code could not be employed to solve the variable property fluid phenomena. A new computer code therefore was developed based on the SIMPLE algorithm which originated at London Imperial College [3]. This computer program has a capability to solve transient, multicomponent flows at low Mach numbers including the effects of variable thermophysical properties (density, viscosity, etc.). Variable density is important in the gas phase because during preignition heating, high temperature gradients are expected near the ignition source (i.e., the heater). In such a situation, the use of the constant density approach along with the Boussinesq approximation may produce very serious quantitative errors in the analysis of the phenomenon. The incorporation of variable thermophysical properties in the liquid phase is also very important since the viscosity and volume expansion coefficient of many liquids vary considerably with temperature. The numerical method used in the current computational model is described in Chapter 6. In the following section a literature review of ignition and flame spread at normal and reduced gravity conditions is presented.

2.2 Literature Review

Comprehensive reviews of the state-of-the-art on flame spreading across liquid fuels have been made by Glassman and Dryer [4] and Kanury [5]. Systematic experimental studies of the ignition phenomenon were undertaken by Princeton researchers in the seventies [6,7,8]. It was found that the factors affecting the ignition and the flame spread depend strongly on whether the bulk fuel temperature is above or below its flash point. Conceptually, the flash point is the liquid temperature which creates a lean flammability limit mixture of fuel vapor and air over the liquid surface. The flash point can be calculated for pure fuels if the lean flammability limit and the saturated vapor pressure are known as a function of temperature. However, the experiments with open pools generally give the flash point temperature (T_{flash}) several degrees higher than the theoretical value. The experimental values of T_{flash} are strongly affected by the height of the ignition source above the liquid surface.

When the liquid fuel temperature is below the flash point, the ignition delay depends upon many factors, such as the initial liquid temperature, liquid viscosity, depth of the pool, and surface tension of the liquid. The heat flux from the ignition source to the liquid is usually maximum just beneath the source and decreases monatonically with the distance from the igniter. The nonuniform heating causes a temperature gradient along the fuel surface. Since the surface tension of liquid varies inversely with temperature, the gradient of surface tension will induce a surface flow from the warmer temperature to the cooler temperatures. Experimentally observed surface velocities have been reported of the order of several centimeters per second. The hot liquid fuel below the igniter is continuously carried away by fluid motion

and replaced by the cold liquid from the volume of the pool. Therefore, the surface-tension-driven convection results in a considerable retardation of the ignition process. Suppression of the motion by artificially reducing surface tension or increasing liquid viscosity enhances the ignitability markedly [4,6].

In contrast with the ignition phenomenon, flame spread across the pool is assisted by the surface-tension-driven convection which can be a dominant factor controlling the flame spreading rate [4,8]. In this case, the flame above the pool plays the role of the ignition source. Hot liquid moves ahead of the flame front thus promoting the ignition of the fuel vapor. Theoretical studies of steady-state flame propagation controlled surface-tension flows have been made by Sirignano and Glassman [8] and Torrance [9,10]. Torrance considered also the influence of natural convective motion in the liquid induced by nonuniform heating from above. The buoyancy effects interact with the surface-tension flows. Furthermore, in flows where the Reynolds number is greater than approximately 10^2 or 10^3, inertial forces balance the buoyancy force. The relative importance of buoyancy, surface-tension, and inertial effects can be analyzed using the nondimensional Grashof (Gr), Marangoni (Ma), and Reynolds (Re) numbers:

$$
\begin{aligned}
Gr &= \frac{\beta g L^3 (T_f - T_o)}{\nu^2} \\
Ma &= \frac{L^2}{\rho \nu \alpha} \left(\frac{d\sigma}{dT} \right) \cdot \left(\frac{dT}{dx} \right)_s \\
Re &= \frac{UL}{\nu}
\end{aligned}
$$

Here L is the characteristic dimension of the pool; ρ, ν, α are the density, kinematic viscosity and thermal diffusivity of the liquid, respectively; T_o is the bulk liquid temperature; T_f is the maximum fuel temperature at the liquid surface (may be replaced by the heater temperature, T_h, when the effect of radiation is included); σ

is the surface-tension coefficient; β is the volume expansion coefficient; and U is a reference velocity. Note that the Grashof and Reynolds numbers may similarly be defined for the gas phase. In this case gas phase properties are used, T_f is replaced by T_h, and T_o denotes the bulk gas phase temperature. The nondimensional vector form of the Navier-Stokes equations using the Boussinesq approximation for scaling purposes may be written as

$$\frac{\partial \vec{u}}{\partial t} + (\vec{u} \cdot \vec{\nabla})\vec{u} = -\frac{Gr}{Re^2}\left(\frac{\vec{g}}{g}\right)T - Eu\nabla P + \frac{1}{Re}\nabla^2\vec{u}$$

Thus when inertial forces balance the buoyancy force one obtains

$$Gr \sim Re^2$$

The order of magnitude of the liquid surface velocity caused by the buoyancy force may therefore be estimated as

$$U_{\text{ref}} \sim \nu\sqrt{Gr}/L = \sqrt{\beta g L \Delta T}$$

Alternatively, a reference velocity may be derived by balancing the tangential shear stresses with the surface-tension gradients at the free surface. For $Re \gg 1$ a boundary-layer flow will occur and the resulting reference velocity, U_σ, may be estimated as [11]

$$U_\sigma \sim \frac{\nu(Ma/Pr)^{2/3}}{L}$$

It should be noted, however, that scaling of the phenomenon is a difficult task because the values of T_f and $(dT/dx)_s$ are not generally known a priori. This is especially true for the ignition problem which is transient by its nature and where the Grashof and Marangoni number vary with time. For this reason, the above reference velocities cannot be used in the computational model. However if T_f is replaced by T_h in the definition of the Grashof number, then U_{ref} may be estimated a priori by its

above definition. A very rough estimation of Gr for liquid R113 in 10^{-4}g with the arbitrarily chosen values of $L = 10$ cm and $T_h - T_o = 500°C$ yields: $Gr = 1$ x 10^5 and $U_{\text{ref}} \sim 2$ mm/s. Torrance [9] found that in a liquid-only simulation at $Gr \sim 10^6$, the buoyancy influence on the liquid flow patterns in the subsurface layer is comparable to the surface-tension effect.

Recently, Furuta et al. [12] performed a finite-difference study of a steady laminar flame spread over a shallow fuel pool. The momentum, energy, and mass conservation equations were solved simultaneously both in the gas and liquid phases. The combustion process was modelled using the flame-sheet approximation. The results of the calculations showed that buoyancy and volume expansion effects influence the gas flow in the region ahead of the flame front. The surface-tension effect on the interface induces recirculation motion in both liquid and gas phases. Such a coupled circulation structure at the gas-liquid interface plays an important role in the flame spread process [4].

It should be noted that in contrast to steady-state flame spread, the transient ignition process has not been treated theoretically in the literature. The preignition hydrodynamics and heat transfer phenomena have been numerically studied by Sirignano et al. in work sponsored by NASA [1]. Detatiled descriptions of this study are given in [1] while the most important results are indicated below.

The calculations were made for the cylindrical enclosure (see Figure 2.1) containing a liquid-air two-layer system. Approximations made in the numerical model include the following:

1. The Boussinesq approximation is made with constant thermophysical properties in both the gas and liquid phase.

2. The 1 mm mild steel walls bounding the enclosure are assumed to be so thin that the temperature drop across the thickness is negligible (the "fin" approximation). The top and side walls are adiabatically isolated from the environment; however, the wall temperature may change spatially and with time as a result of the convective heat exchange with the fluids, the radiative transfer between the different surfaces, and the thermal conduction along the walls (one-dimensional transient heat conduction).

3. All of the solid surfaces as well as the gas/liquid interface are assumed opaque and black. Gas radiation is neglected.

4. Liquid vaporization, diffusion, chemical reaction, and radiative absorption in the gas phase are neglected.

5. The liquid surface is assumed to be flat.

The typical streamline and temperature patters are illustrated in Figures 2.2 and 2.3 for a liquid decane-air system at normal gravity conditions. Here, the dimensions of the cylindrical enclosure are: R = 10 cm, H = 20 cm and height of the liquid is 10 cm. The enclosure is heated by a small circular source (r = 2 cm) at the center of the top cover. The hot spot has no thermal contact with the remaining part of the top cover. The initial temperature of the system is 300 K, while the temperature of the heat source is held constant at 1000 K. The bottom wall of the enclosure is maintained at the constant temperature 300 K.

In the liquid phase, the major changes of velocity and temperature occur in a thin region very close to the surface. Below this boundary layer, the liquid motion exhibits the multi-vortex structure which is caused by the interaction between

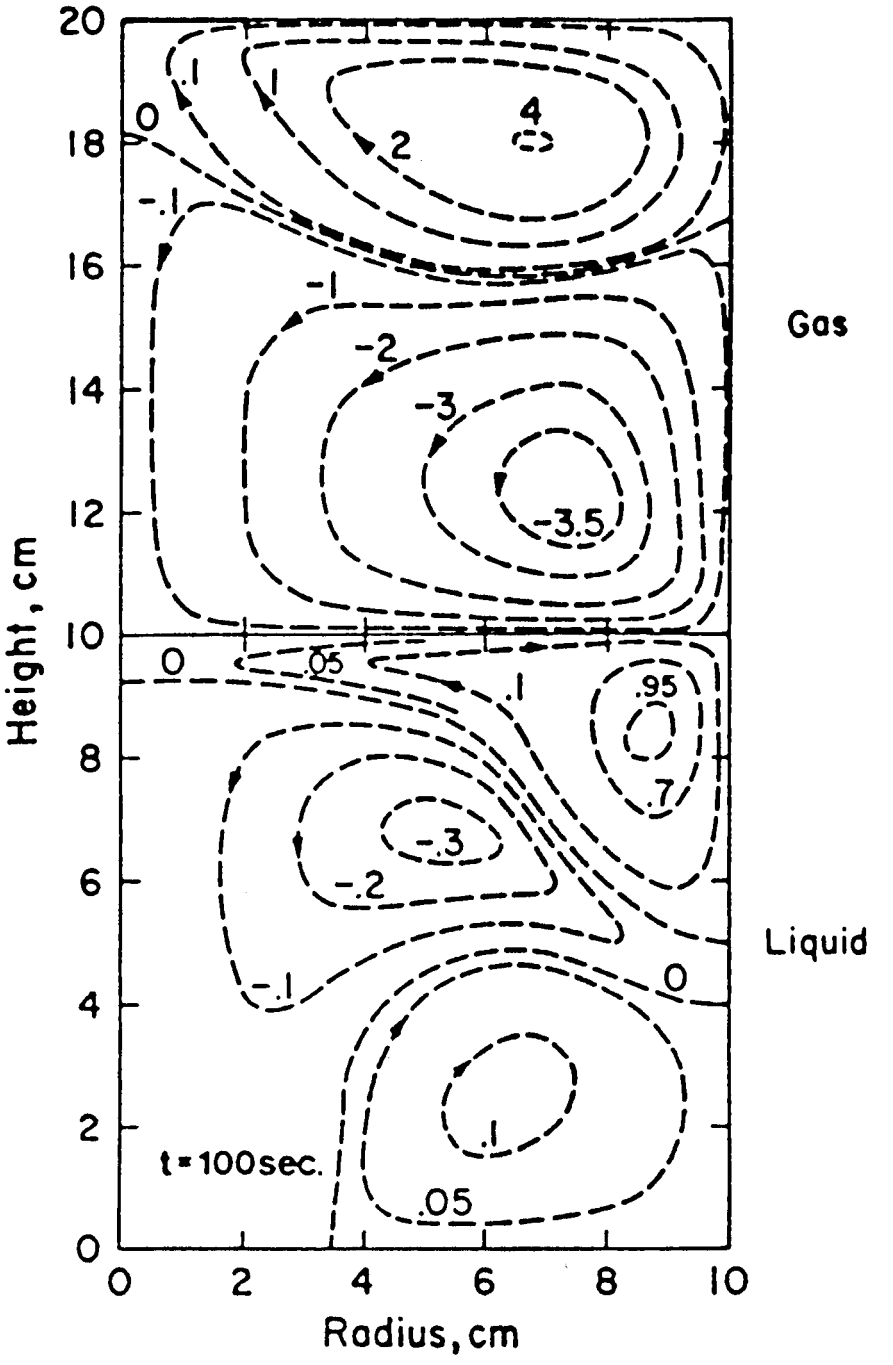

Figure 2.2: Typical streamline patterns for a liquid decane-air system at normal gravity conditions (taken from Reference [1]). Sign convention for nondimensional stream function shown on figure is opposite to equation (7.1).

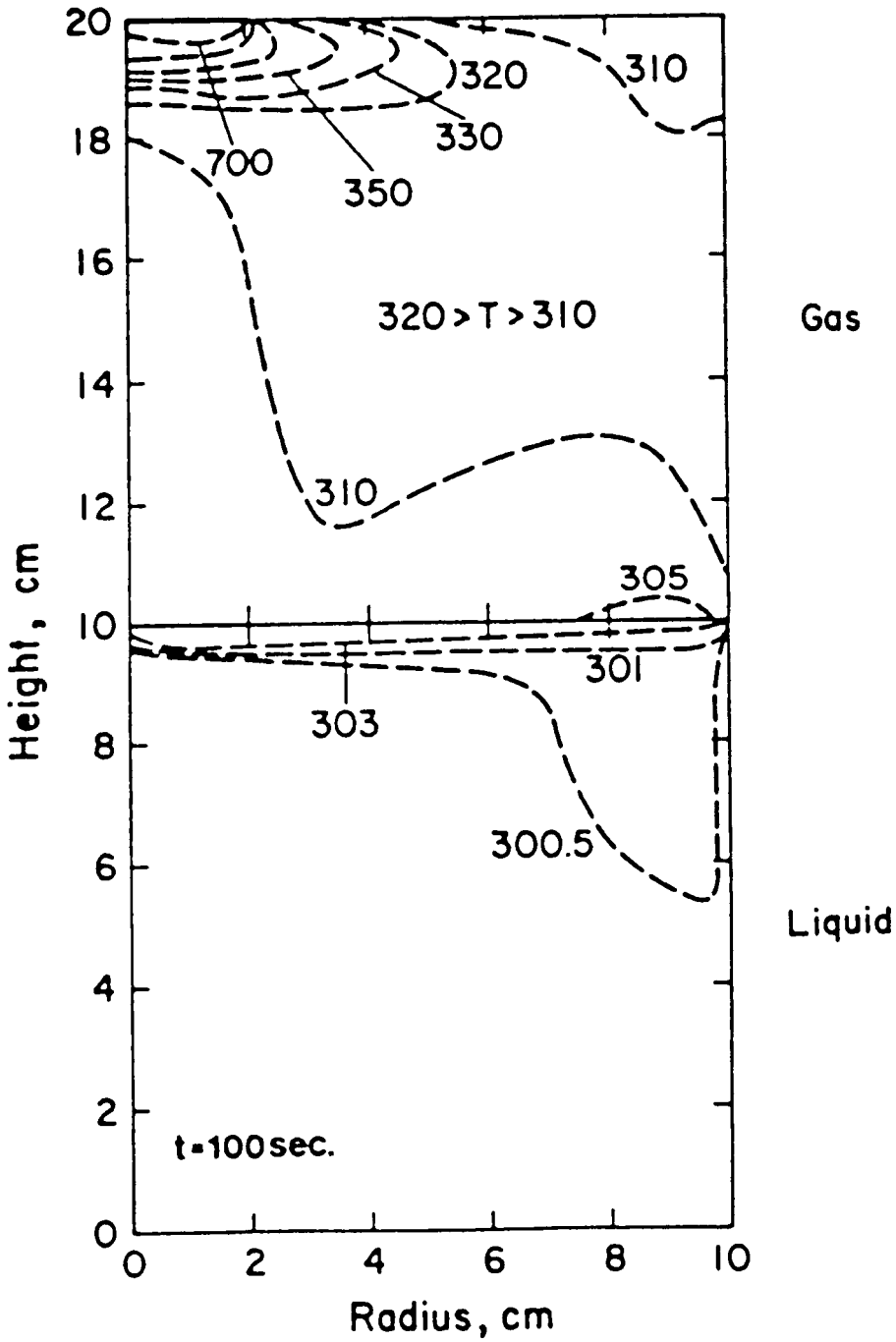

Figure 2.3: Typical temperature contours for a liquid decane-air system at normal gravity conditions (taken from Reference [1]).

the surface-tension-driven and natural convection phenomena. Contrastingly, only single vortices are observed in the gas and liquid phases at low gravity conditions ($g = 10^{-4}$ m/s^2). Figure 2.3 shows that the hot gas zone is concentrated in close proximity to the ignition source. Below this zone the gas remains relatively cold. A slight temperature rise is also observed near the liquid surface which is heated by radiation. Therefore, the ignition of fuel vapor/air mixture will probably be initiated near the hot source rather than close to the liquid fuel surface.

The calculations demonstrated the great importance of including effects of thermal radiation and thermal inertia of the walls bounding the enclosure. Nonuniform radiative heating of a liquid surface appears to be the principal factor in the initiation of a surface-tension-driven convection along the gas-liquid interface. The thermal inertia of the walls controls the temperature growth in the gas phase. The gas and liquid motions are the net results of both surface-tension and buoyancy forces.

2.3 Justification for Space-Based Experiment

As mentioned in the previous section, the scientific literature is devoid of experimental study of ignition and flame spread characteristics under conditions of reduced gravity. It is not clear whether ignition susceptibility and flame speed will increase or decrease in reduced gravity. The only way to change the scale of experiments (particularly to decrease the Grashof number) without affecting other important parameters is to change the gravity level. Currently planned ground-based low gravity (drop tower) experiments, though necessarily transient in nature, should provide an excellent basis for assessing relative effects of various gravity levels and determining the

feasibility of proceeding to a space-based experiment. However, modelling suggests that reduced gravity experiments will require several minutes to reach a quasi-steady state. A quasi-steady state condition is characterized by stabilized thermal and dynamic boundary layers [1]. For a 10 cm height of air at 300 K, the time scale for thermal diffusion may be estimated as

$$T \sim \frac{L^2}{\alpha} = 454 \text{ seconds.}$$

The significance of this is that it would take on the order of 7–8 minutes for heat to conduct through a 10 cm height of air. Therefore the full effect of heat conduction cannot be realized in a 5 second drop tower experiment.

Quasi-steady state is important in both the ignition and flame spread problems. In the current preignition problem the initial liquid temperature is below its vaporization temperature and well below its flash point temperature. Hence a relatively long period of time ($\gg$ 5 seconds) is required to study the asymptotic behavior of the liquid fuel as it vaporizes. The quasi-steady state behavior of the experiment will give insight to the associated flame spread problem, where the primary interest is the asymptotic spreading rate of a flame once it has been established. In order to study the quasi-steady state behavior of the preignition phenomenon under the required range of $\beta g L \Delta T$ and the Grashof number, a space-based facility as offered by the Shuttle is required.

2.4 Objectives

The principal objective of the reduced gravity experimental effort is to verify experimentally the predicted behavior of an enclosed liquid fuel pool during the

preignition phase and to determine via measurement the role of gravity on such behavior. Interesting questions that should be resolved by the research concern: (*i*) the determination of domains where conduction, convection, or radiation are dominant, (*ii*) the time required to reach an ignition, (*iii*) the importance of heat transport through the gas versus heat transport through the liquid, and (*iv*) the domains where surface-tension-driven flow dominates buoyancy-driven flow. Space-based experimentation will be supported by the aforementioned computational research as well as ground-based experimentation. NASA-LeRC will conduct 1-g tests and drop tower tests to support the research program. By varying the majority of experimental parameters in these ground-based tests, the cost of space-based experimentation will be minimized. The science requirements for both the space-based and the ground-based experimentation will be given in this document.

2.5 Use of NASA's Microgravity Facilities

The NASA-LeRC 5.18 and 2.2 second drop tower facilities will be used to obtain low-gravity transient data to support the computational and space flight experimental efforts. Freon 113 (liquid) and air will be used in plexiglass containers of planar and cylindrical geometries. Data from the drop tower tests will be useful in verifying the design and feasibility of a space-based experiment. For example, the hydrodynamics of maintaining a flat gas-liquid interface in reduced gravity may be evaluated in drop tower tests. The effectiveness of flow visualization techniques may also be assessed in these short duration microgravity tests. However, the dynamics of the transient reduction of gravity in the drop tower tests may prevent valid scientific data collection in the available reduced gravity time.

Chapter 3

Identification of Experiments

3.1 Test Matrix

The following section summarizes the test matrix for each of the three experimental settings (1-g, drop tower, and space-based).

The minimum goal of the entire experimental research is to study the problem of interest over at least a three order of magnitude range in the inertia of the flow. When $Re > 10^2$ or 10^3, inertial forces balance the buoyancy force and the inertia of the flow may be estimated by

$$U_{\text{ref}}^2 \sim \beta g L(T_h - T_o) = \beta g L \Delta T$$

where all variables are as before except T_h, which is the heater temperature. This range should cover $Gr = 10^3 - 10^6$ in order to study the relative effects of convection versus conduction and buoyancy versus surface tension on the flow. The transitions of dominating flow effects cited earlier in Section 2.1, namely $Gr \sim 10^3$ and $Gr \sim 10^6$, require experimental validation. Contrary to the previously given definition of Gr

(which used the maximum fuel temperature of the liquid surface as the hotter temperature), the Grashof number cited above is determined by

$$Gr = \frac{\beta g L^3 (T_h - T_o)}{\nu^2}$$

It would be more desirable to cover a four or five order of magnitude range in $\beta g L \Delta T$ to provide more assurance that the key ranges of buoyancy and inertial forces as well as the transitions are studied in the experiments. The characteristic length scale for $\beta g L \Delta T$ and the Grashof number is somewhat arbitrary. In previous simulations of a cylindrical test cell, the radius of the container was chosen. In future experiments with a rectangular test cell, the hydraulic diameter or the half-length of the container may be chosen for the length scale. Whatever length scale is chosen, it is the quantity $\beta g L \Delta T$ ($= U_{\text{ref}}^2$) in combination with other important parameters (e.g., aspect ratio, heater size, etc.) which drive the results. Although the drop tower provides about a five order of magnitude reduction in gravity (and hence $\beta g L \Delta T$), the results of such tests are only transient. Through the use of the Shuttle, one can obtain a reduction of gravity of three or four orders of magnitude. Varying the heater temperature ($\Delta T = T_h - T_o$) will provide an additional order of magnitude variation. Changing L will also linearly affect the inertia of the flow. The test matrix given in Table 1 was designed to (1) provide for the desired variation in $\beta g L \Delta T$ for the quasi-steady state experiments, and (2) investigate issues and effects of parametric variations relevant to the design of the space-based experiment.

Table 1A: Test Matrix

Variable	*1-g*	*Drop Tower*	*Space-Based*
Test Cell Dimensions Note: L is half-length of test cell (see Figure 3.2)	Cylindrical (H. x dia.): • 1 cm x 1 cm • 5 cm x 5 cm • 10 cm x 10 cm Rectangular[a] (H x 2L x W): • 20 cm x 15 cm x 30 cm • TBD	Cylindrical (H. x dia.): • 1 cm x 1cm • 5 cm x 5 cm • 10 cm x 10 cm Rectangular[a] (single phase only) (H x 2L x W): • 10 cm x 7.5 cm x 15 cm • TBD	Cylindrical (H. x dia.): • TBD (10 cm x 10 cm)
Test Cell Material	• Plexiglass, 1/8-1/4" thick • Thin glass[a] (TBD thickness)	• Plexiglass, 1/8-1/4" thick	• TBD (plexiglass, glass, or sapphire)
Liquid Phase Fluid	• Silicon oil • R113 • Water[a]	• Silicon oil • R113	R113 with glass or sapphire test cell
Gas Phase Fluid	Air	Air	Air
Heater Dimensions (not including water-cooled jacket)	Cylindrical (dia.): • 5 mm • 1 cm • 2.5 cm • 5 cm Rectangular (length)[b]: • 2.5 cm • 5 cm	Cylindrical (dia.): • 5 mm • 1 cm • 2.5 cm • 5 cm Rectangular (length)[b]: • 2.5 cm • 5 cm	Cylindrical (dia.): • 2.5 cm • 5 cm
Heater Temperature	• 350 K • 575 K • 800 K	• 350 K • 575 K • 800 K	• 350 K • 800 K
Heater Emissivity	• 1.0 • TBD	• 1.0	• 1.0
Liquid Fill Level (fraction of container height)	• 0.125 • 0.25 • 0.5	• 0.125 • 0.25 • 0.5	• 0.125 • 0.5
Use of Tracers for Flow Visualization	• Yes • No	• Yes • No	• Yes
Use of Thermo-couples for Measurement of Fluid Temperatures	• Yes • No	• Yes • No	• No

[a]Optional.
[b]The rectangular heater strip with water-cooled jacket spans the width of the rectangular container.

Table 1B: Sequential Test Plan

A. Single-Phase, 1-g Tests

Test Cell[a]	*Heater Size*	*Heater Temp.*	*Gas Tracers*
• 10 cm x 10 cm	• 1 cm • 2.5 cm • 5 cm	• 800 K • 575 K • 350 K	Tobacco smoke
• 5 cm x 5 cm	• 1 cm • 2.5 cm	• 800 K • 575 K • 350 K	
• 1 cm x 1 cm	• 5 mm	• 575 K • 350 K	

[a]Test cell is cylindrical, plexiglass unless otherwise specified; dimensions given are Height x Diameter; additional tests with rectangular cells and/or thin glass material are optional.

B. Two-Phase, 1-g Tests

Test Cell[a]	*Heater Size*	*Heater Temp.*	*Liquid*[b]	*Liquid Fill Level*[c]	*Gas/Vapor Tracers*
• 10 cm x 10 cm	• 1 cm • 2.5 cm • 5 cm	• 800 K • 575 K • 350 K	Silicon Oil	• 0.5 • 0.25 • 0.125	• None • Tobacco smoke
• 10 cm x 10 cm	• 1 cm • 2.5 cm • 5 cm	• 800 K • 575 K • 350 K	R113	• 0.5 • 0.25 • 0.125	• None • Tobacco smoke • R113 vapor
• 5 cm x 5 cm	• 1 cm • 2.5 cm	• 800 K • 575 K • 350 K	Silicon Oil	• 0.5 • 0.125	• None • Tobacco smoke
• 5 cm x 5 cm	• 1 cm • 2.5 cm	• 800 K • 575 K • 350 K	R113	• 0.5 • 0.125	• None • Tobacco smoke • R113 vapor
• 1 cm x 1 cm	• 5 mm	• 575 K • 350 K	Silicon Oil	• 0.5	• None • Tobacco smoke
• 1 cm x 1 cm	• 5 mm	• 575 K • 350 K	R113	• 0.5	• None • Tobacco smoke

[a]Test cell is cylindrical, plexiglass unless otherwise specified; dimensions given are Height x Diameter; additional tests with rectangular cells and/or thin glass material are optional.
[b]Additional tests with water as the liquid are optional.
[c]Liquid fill level is expressed as fraction of container height.

Table 1B: Sequential Test Plan (continued)

C. Single-Phase, Drop Tower Tests

Test Cell[a]	*Heater Size*	*Heater Temp.*	*Gas Tracers*
• 10 cm x 10 cm	• 1 cm • 2.5 cm • 5 cm	• 800 K • 575 K • 350 K	Tobacco smoke
• 5 cm x 5 cm	• 1 cm • 2.5 cm	• 800 K • 575 K • 350 K	
• 1 cm x 1 cm	• 5 mm	• 575 K • 350 K	

[a]Test cell is cylindrical, plexiglass; dimensions given are Height x Diameter.

D. Two-Phase, Drop Tower Tests

Test Cell[a]	*Heater Size*	*Heater Temp.*	*Liquid*	*Liquid Fill Level*[b]	*Gas/Vapor Tracers*
• 10 cm x 10 cm	• 1 cm • 2.5 cm • 5 cm	• 800 K • 575 K	Silicon Oil	• 0.5 • 0.25 • 0.125	• None • Tobacco smoke
• 10 cm x 10 cm	• 1 cm • 2.5 cm • 5 cm	• 800 K • 575 K	R113	• 0.5 • 0.25 • 0.125	• None • Tobacco smoke • R113 vapor
• 5 cm x 5 cm	• 1 cm • 2.5 cm	• 800 K • 575 K	Silicon Oil	• 0.5 • 0.125	• None • Tobacco smoke
• 5 cm x 5 cm	• 1 cm • 2.5 cm	• 800 K • 575 K	R113	• 0.5 • 0.125	• None • Tobacco smoke
• 1 cm x 1 cm	• 5 mm	• 575 K	Silicon Oil	• 0.5	• None • Tobacco smoke
• 1 cm x 1 cm	• 5 mm	• 575 K	R113	• 0.5	• None • Tobacco smoke

[a]Test cell is cylindrical, plexiglass; dimensions given are Height x Diameter.
[b]Liquid fill level is expressed as fraction of container height.

E. Two-Phase, Space-Based Tests

Test Cell[a]	*Heater Size*	*Heater Temp.*	*Liquid*	*Liquid Fill Level*[b]	*Gas/Vapor Tracers*
• TBD (10 cm x 10 cm)	• 2.5 cm • 5 cm	• 800 K • 350 K	R113	0.125 0.5	• TBD (R113 vapor)

[a]Test cell is cylindrical; dimensions given are Height x Diameter.
[b]Liquid fill level is expressed as fraction of container height.

As indicated in Table 1A, many parametric studies need to be conducted in the 1-g experiments. The order in which these tests should be performed is given in Table 1B. This table specifies a large number of 1-g tests since there are several possible combinations for each test cell in the table. For example, nine tests are specified for the single-phase, 1-g experiments with the 10 cm x 10 cm test cell because three heater temperatures are specified for each of the three heater sizes. Even more combinations are specified for the two-phase, 1-g tests. However, some of these tests may be omitted from the matrix if experiments indicate that they may be superfluous for completing a parametric study. The following three guidelines should be adhered to for each test conducted:

1. Each test should be repeated at least twice to assure reproducibility. Success is measured by achieving approximately equal results (differing by no more than 10%) two consecutive times.

2. Some tests need to be done where the laser path is modified (i.e., reduce the laser power or bring the laser in from the bottom).

3. Scale measurements are required prior to the two-phase tests in order to correct for parallax error.

The heater temperatures 350 K and 800 K were selected to provide an order of magnitude range of $\beta g L \Delta T$. The 575 K heater temperature was selected as an intermediate setting. Two heater sizes or two different heater emissivities should also be used with the test cells to obtain a variation of the radiation heat transfer effect. The interaction of droplet/particle tracers and thermocouples with the fluid flow will be evaluated in the 1-g tests. Single-phase experiments will also be conducted in the 1-g tests to help

verify the computational code. The same test cells can be used for these experiments as will be used for the two-phase tests.

Only three variables will be changed in the space-based experiments: Heater temperature, heater size, and liquid fill level. Of these, only the former is deemed a minimum requirement (in order to study the required range in $\beta g L \Delta T$). Varying the other two parameters is desirable. Two options for each of these three variables implies eight different tests planned for the Shuttle experiment.

3.2 Measurement Requirements

Measurement requirements vary between the three experiment settings and are summarized in Table 2. While it is highly desirable to obtain detailed temperature and velocity field measurements throughout the flow field, it is also very difficult and expensive to do so. Furthermore, such detail is not necessary to achieve the goal of the experimentation: to verify experimentally the results of the computational research. For this reason both "minimum" and "preferred" requirements are specified in this section. Most of the detailed measurements will be taken in the 1-g experiments. The reduced gravity tests therefore will require a minimum of flow visualization and temperature measurements to validate the simulated results. The measurement requirements below were developed for the minimum and maximum heater temperatures which will be used in the experiments (namely 350 K and 800 K). Requirements for intermediate heater temperatures (such as 575 K) may be linearly interpolated.

Table 2: Science Requirements

Design of experimental apparatus:

Item	*Minimum Requirement*	*Preferred Requirement*
Range of Grashof number covered	10^3–10^6	10^2 or 10^3 - 10^7
Range of $\beta g L \Delta T$ covered	3 orders of magnitude	5 orders of magnitude
Recommendation: Vary	(1) G-level by different experiment settings to obtain 3 order of magnitude range. (2) Heater temperature. (3) Size of test cell.	
Temperature variation of heater	±1%/second at 1 heater temperature	Same for 2–3 heater temperatures
Liquid fill level	1 setting at 50% of cell height	2–3 settings to study effect of σ in shallow versus deep pools
Size and/or emissivity of heater	1 setting	2–3 settings to vary radiation heat transfer effect

Measurement requirements:

Item	*Minimum Requirement*	*Preferred Requirement*
Velocity	Qualitative full field flow visualization. Film synchronized to 0.5 second with the run time of the experiment.	Quantified flow velocities; • With 800 K heater[a]: 1–10 cm/sec ±1–2 mm/sec • With 350 K heater[a]: 0.5–5.0 mm/sec ±0.1–0.2 mm/sec See Section 3.2, requirement #1 for spatial resolution requirements. Film synchronized to 0.005 second with the measured data.

[a]Note: Anticipated velocities in liquid phase more than 2 mm below surface are on order of 0–0.1 mm/sec (may be too difficult to resolve quantitatively) for experiment times of less than 10 minutes.

Table 2: Science Requirements (continued)

Measurement requirements: (continued)

Item	*Minimum Requirement*	*Preferred Requirement*
Temperature	Heater, ambient, and wall temperatures; also fluid temperatures for 1-g tests. • With 800 K heater: 280–810 K ±0.5°C • With 350 K heater: 280–355 K ±0.1°C Data rate: 1 Hz	In addition, fluid temperatures especially along liquid surface. See Section 3.2, requirement #2 for spatial resolution requirements.
Pressure	Ambient and gas phase in test cell 11.7–17.7 psia ±0.2 psia Data rate: 1 Hz	Same
Gravitational acceleration	In space-based experiment for normal gravity direction 10^{-3}–$10^{-4} \pm 5 \times 10^{-5}$ g Data rate: 5 Hz	All 3 principal directions for space-based experiment plus normal gravity direction for 1 drop tower run (latter $10^{-5} \pm 10^{-6}$ g) Data rate: 10–100 Hz
Interfacial position	Measure minimum and maximum height of liquid surface to ±4% of radius (half-length) of test cell.	Measure position and shape to ±4% of radius (half-length) of test cell every 1 sec until change is less than 1 mm/sec.

Experimental conditions requirements:

Item	*Minimum Requirement*	*Preferred Requirement*
Ambient temperature	Shall be between 240 K and 320 K	300 K ±5 K
Ambient pressure	14.7 ±3 psia	Same
G-jitter	Shall not exceed 10^{-4} g	Shall not exceed 5% of the normal gravitational acceleration.
Interfacial position	Local angle of liquid surface shall not exceed 0.04 radian.	Local angle of liquid surface shall not exceed 0.02 radian.

1. Velocity Measurements

Minimum Requirement: Flow visualization shall be used to measure qualitatively the flow pattern with a full field of view in each of the three experiment settings. Flow visualization is required in one (1) vertical plane of the test cell parallel to the expected two-dimensional or axisymmetric motion. The flow visualization record should be synchronized to approximately 0.5 second with the run time of the experiment.

Preferred Requirement: In addition to the above, it is desirable to quantify the velocity measurements. Experiments using the 800 K heater should measure velocities on the order of 1–10 cm/sec within an accuracy of ±1–2 mm/sec. Experiments using the 350 K heater should measure velocities on the order of 0.5–5.0 mm/sec within an accuracy of ±0.1–0.2 mm/sec. Anticipated velocities more than 2 mm below the liquid surface are on the order of 0–0.1 mm/sec. Therefore it may be too difficult to resolve quantitatively the velocities in this regime. Film from the flow visualization should by synchronized to 0.005 second with the measured data. The fluid velocity measurements should be spatially resolved with the following accuracy:

Near inside of wall (gas phase):

±1 mm within 5 mm of wall for 1-g experiments.

±1 mm within 10 mm of wall for reduced gravity experiments.

Near liquid-vapor interface:

±2 mm within 5 mm of interface (in gas phase) for 1-g experiments.

±2 mm within 10 mm of interface (in gas phase) for reduced gravity experiments.

±2 mm within 2 mm of interface (in liquid phase) for all experiments.

Elsewhere:

± 4 mm (gas phase).

± 10 mm (liquid phase).

Quantitative flow measurements should be taken at a frequency of 1 Hz throughout each experiment. Data should be obtained for the full field of flow if possible (measurements along the liquid surface are the most desirable). At some point during each test it is required to check for axisymmetry.

Rationale: Qualitative flow visualization will reveal the number and shape of the recirculation cells. Such information is necessary to compare with the predictions of the computational code as well as with previous test results from related experiments. Quantifying the flow field velocities is highly desirable in order to further validate the model. Without quantified flow velocities, a detailed comparison of the dominating mechanisms cannot be made. The expected orders of magnitude of the flow velocity for the different tests are based on computer simulation results. The desired accuracy of the measurements is based on a deemed allowable ± 10–20% error in the measurements. This is somewhat arbitrary.

Spatial resolution requirements were derived from anticipated velocity gradients based on simulated results. Where the gradients are large, a higher spatial resolution is required. The accuracies cited in the preferred requirement are on the order of a grid size used for the respective regions in simulations run on the CRAY computer. If the true velocity gradient is known, then the error in a velocity measurement due to an error in spatial resolution (say in the y-direction) is

$$\Delta U = \frac{\Delta U}{\Delta y} \Delta y$$

This equation shows that for an allowable error in velocity measurement due only to an error in spatial resolution, the required accuracy on the location of the measurement is inversely proportional to the velocity gradient. The quantified requirements given above yield allowable errors in the velocity measurements due to uncertain spatial resolutions in all regions except those very close to a wall (where the no slip condition results in very large velocity gradients). Large velocity measurement errors will exist for these regions as more stringent requirements than ± 1 mm do not seem practical. The preferred film synchronization requirement reflects a ± 0.5 mm contribution to the error in spatial resolution measurements for 10 cm/sec velocities.

2. Temperature Measurements

Minimum Requirement: In all experiments, temperature measurements of the heater surface and the test cell walls are required. The temperature of the ambient environment shall also be measured in the 1-g and space-based experiments. The locations of the heater surface and wall temperature measurements are shown on Figures 3.1 and 3.2. In these figures, the locations of the thermocouples are specified more as a guideline than as a precise requirement. The most important temperature measurements are the ones adjacent to the liquid surface and also those on and adjacent to the heater. The other thermocouples which are shown on the figure are either equally spaced along the walls of the gas phase in one-half of one plane, or are situated in order to check for axisymmetry of the temperature field. Although not shown in the figures, future tests may also incorporate a rake with thermocouples mounted along the centerline immediately below the liquid surface (similar to the design used in Reference [13]). The accuracy of the temperature measurements shall

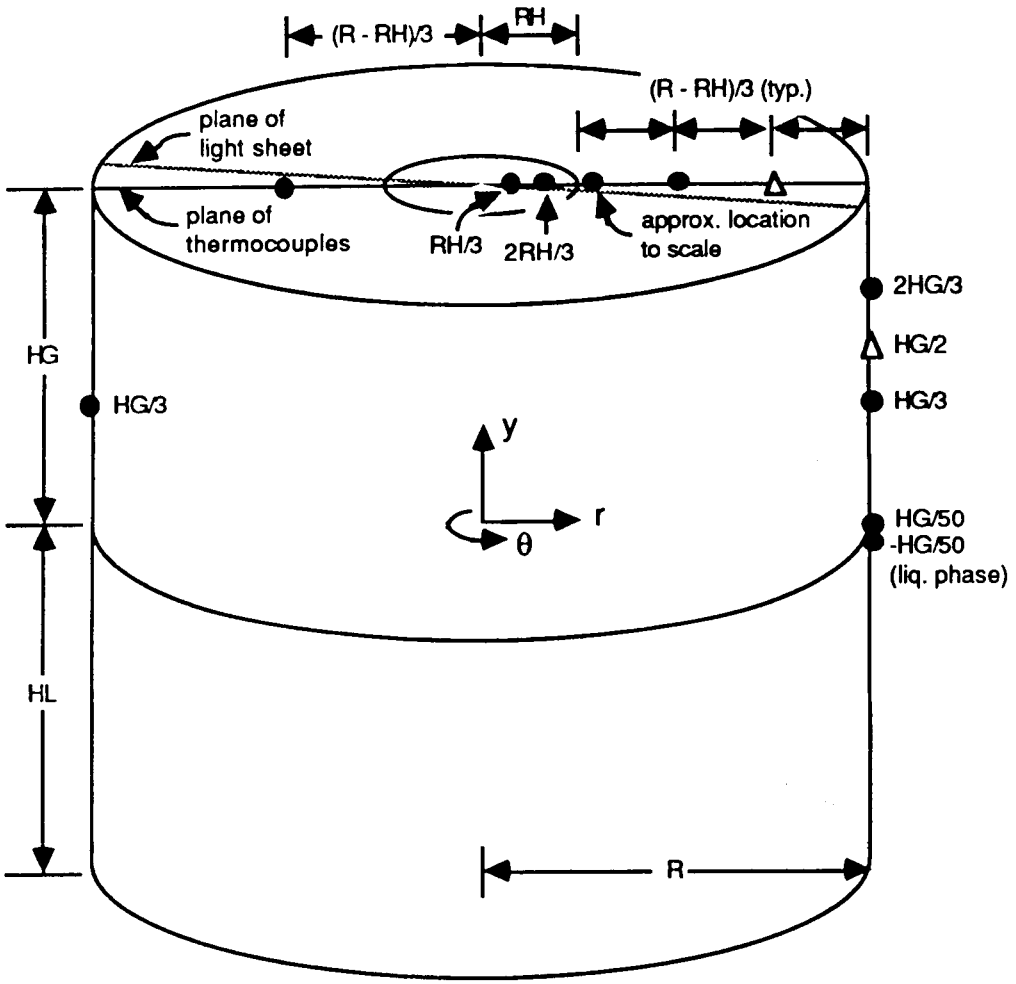

Notes: (1) Thermocouples are on the inner wall at r or y locations specified in above figure except where noted below.

(2) The two thermocouples at r = RH/3 and r = 2RH/3 are on top of the heater.

(3) The two thermocouples marked with the symbol "Δ" are on the outside of the test cell wall. These thermocouples are not required for drop tower tests.

(4) HG = height of gas phase, HL = height of liquid phase, R = inner radius of test cell, RH = radius of heater assembly.

Figure 3.1: Thermocouple locations for heater surface and wall temperature measurements (cylindrical geometry).

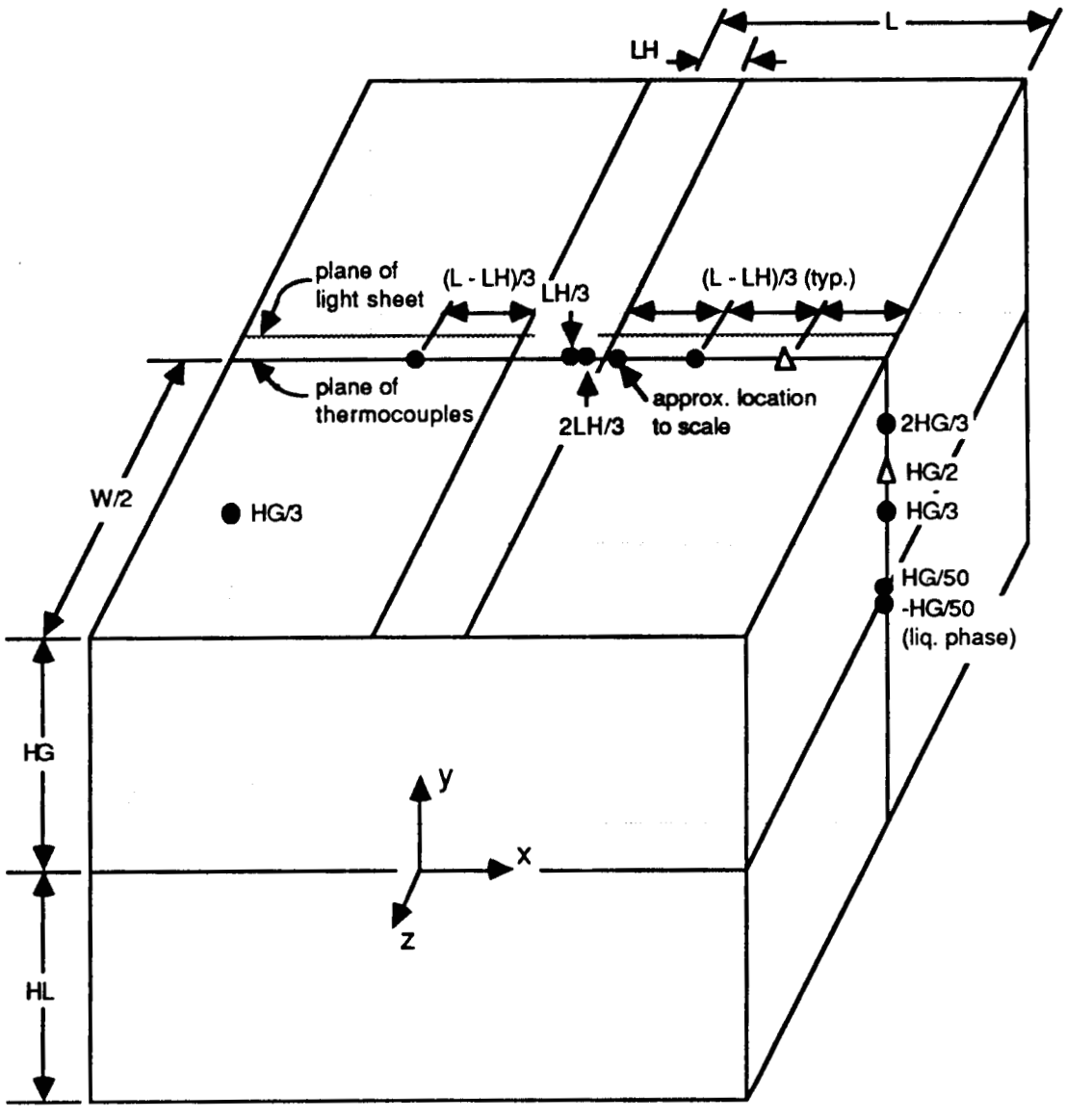

Notes: (1) Thermocouples are on the inner wall at x or y locations specified in above figure except where noted below.

(2) The two thermocouples at x = LH/3 and x = 2LH/3 are on top of the heater.

(3) The two thermocouples marked with the symbol "Δ" are on the outside of the test cell wall. These thermocouples are not required for drop tower tests.

(4) HG = height of gas phase, HL = height of liquid phase, 2L = inner length of test cell, 2LH = length of heater assembly, W = width of test cell.

Figure 3.2: Thermocouple locations for heater surface and wall temperature measurements (planar geometry).

be at least ±0.5°C for tests with the 800 K heater, at least ±0.3°C for tests with the 575 K heater, and at least ±0.1°C for tests with the 350 K heater. The wall temperature measurements shall be resolved spatially to an accuracy of ±1 mm. The frequency of the measurements shall be at least 1 Hz.

Preferred Requirement: In addition to the above, it would be desirable to obtain fluid temperature measurements, particularly near the liquid surface. The fluid temperature measurements should be resolved spatially to the following accuracy:

Below top of cell:

±1 mm within 5 mm of wall for 1-g experiments.

±1 mm within 10 mm of wall for reduced gravity experiments.

Near side walls (gas phase), except where specified above:

±2 mm within 5 mm of wall for 1-g experiments.

±2 mm within 2 mm of wall for reduced gravity experiments.

Near liquid-vapor interface:

±2 mm within 5 mm of interface (in gas phase) for 1-g experiments.

±2 mm within 10 mm of interface (in gas phase) for reduced gravity experiments.

±2 mm within 2 mm of interface (in liquid phase) for all experiments.

Elsewhere:

±4 mm (gas phase).

±10 mm (liquid phase).

Rationale: Again, quantitative measurements are required to validate the computational model. Such information would supplement the quantified flow

velocity measurements. The temperature of the heater surface must be monitored and recorded to provide input to the computer code. The required accuracy of the temperature measurements is based on the expected temperature rise along the inner wall of the test cell in the gas phase and along the liquid surface. Simulations indicate that these temperatures may rise only about 1°C over the course of one hour with the 350 K heater. Hence for this case a minimum allowable precision is ±0.1°C. With the 800 K heater the inner wall may increase a few degrees before a quasi-steady state condition is reached. Hence ±0.5°C would be approximately ±20% of this temperature rise. The required accuracy for temperature measurements with the 575 K heater was interpolated from the above requirements for the 350 K and 800 K heaters. The minimum time between temperature measurements (1 s) is commensurate with the time required for the inner surface temperature of a plexiglass wall to increase 1°C in response to an 800 K 2.5 cm diameter heater. This is also of the same order as the time required for thermal diffusion between two node points in the container wall in the computational model (based on 10 node points in a 1/4" thick glass wall). Similar to the velocity requirements, spatial resolution requirements were derived from anticipated temperature gradients based on simulated results. Very close to the heater large temperature measurement errors will exist due to the large temperature gradients. For example, simulations indicate that gradients on the order of 100–200°C/mm will exist 1–2 mm below the heater. In this region an error of ±1 mm in spatial resolution whould therefore result in temperature measurement uncertainties of 100–200°C. Such a large uncertainty in this region may have to be accepted, as more stringent requirements than ±1 mm do not seem practical.

3. Pressure Measurements

Minimum Requirement: It is required to measure the ambient pressure and the average pressure of the gas phase in the test cell. The accuracy of the measurements shall be ±0.2 psia. The frequency of the measurements shall be at least 1 Hz.

Rationale: Ambient pressure measurements are useful in assessing the possibility that gas leakage occurred during an experiment due to a pressure difference across a small space between the heater and the container or between any other small crevice of the test cell. The average pressure inside the test cell and the bulk temperature of the gas is required to determine the total vaporization rate of the liquid as a function of time. The required accuracy of ±0.2 psia represents approximately a 10–15% change in temperature of the gas inside the container or a 10–15% change in ambient pressure.

4. Gravitational Acceleration Measurements

Minimum Requirement: Gravitational acceleration levels shall be measured in the space-based experiments. As a minimum, the acceleration in the plane of the normal gravitational force is required. The accuracy of the measurements shall be $\pm 5 \times 10^{-5}$ g (approximately $\pm 5 \times 10^{-4}$ m/s^2). Data should be collected as frequently as practical (data rate shall be at least 5 Hz).

Preferred Requirement: Gravitational acceleration levels shall be measured in the three principal directions of the space-based experiments. The accuracy of the measurements shall be $\pm 5 \times 10^{-5}$ g (approximately $\pm 5 \times 10^{-4}$ m/s^2). In addition, the acceleration should be measured in the plane of the normal gravitational force during one drop test run. The accuracy of this measurement shall be $\pm 10^{-6}$ g (approximately $\pm 10^{-5}$ m/s^2). The data collection rate for the

gravitational acceleration shall be at least 5 Hz for the space-based experiments, and at least 10 Hz for the drop tower test.

Rationale: The computational code can incorporate an oscillating component of the normal gravitational force in order to simulate g-jitter which is encountered on manned space vehicles. These random fluctuations occur at high frequency, so the data collection rate must be correspondingly high. A minimum rate of 5 Hz (data every 0.2 second) was selected because this is comparable to the time step used in the simulation for a low-gravity run after achieving a quasi-steady state. A greater frequency of 10–100 Hz would be more desirable to represent more accurately the fluctuating g-jitter and to correspond with the smaller time steps required in the simulation prior to achieving a quasi-steady state. Gravitational acceleration levels orthogonal to the normal gravitational force would be desirable to compare with the magnitude of the normal gravitational acceleration. Such measurements are necessary to assess the effect of these acceleration components on the flow. The data collection rate for these orthogonal gravitational acceleration components need not be as high (about 1 Hz) as the normal gravitational acceleration rate. The accuracy of the acceleration measurements represent $\pm 10\%$ of the expected mean normal gravitational acceleration levels.

5. Measurement of Interfacial Position

Minimum Requirement: A qualitative picture shall be taken of the portion of the liquid surface which meets the front side wall (facing the camera). The minimum and maximum height of the liquid surface must be measured with an accuracy of $\pm 4\%$ of the radius (half-length) of the test cell.

Preferred Requirement: The position and shape of the liquid surface shall be measured with an accuracy of ±4% of the radius (half-length) of the test cell. If an initial change in the position of the liquid surface occurs (as expected in drop tower tests), then the position and shape of the liquid surface shall be measured every 1 second until the position of the interface changes by less than 1 mm over a period of 1 second (or until the drop is complete for the case of the drop tower tests).

Rationale: The height of the liquid pool must be determined. The required accuracy of ±4% of the radius (half-length) of the test cell is comparable to the related requirement of allowable liquid surface deformation. It is also desirable to obtain the quantitative shape of the liquid surface so that thermocouples may be placed accurately right above the liquid surface to obtain important temperature measurements along the interface. If necessary, quantitative information on the shape of the liquid surface may also be used in a future modification of the computational model which allows for a curved gas/liquid interface. Since obtaining quantitative information on the shape of the liquid surface may be exceptionally difficult to accomplish, this has been cited as a "preferred" rather than a "minimum" requirement.

3.3 Experimental Conditions

Some external conditions must be controlled to minimize their effects on the experiment. The requirements for the external conditions are given below. In general these requirements are not very restrictive because the computational model incorporates environmental conditions such as ambient temperature and pressure and normal

(vertical) gravitational force. Hence measurements of these parameters is the only strict requirement. However, as noted below, operating the experiments under "normal" external conditions is the preferred requirement.

1. Ambient Temperature

   Minimum Requirement: The ambient temperature shall not exceed 320 K nor be less than 240 K during the experiment.

   Preferred Requirement: The ambient temperature should be maintained at 300 $\pm$5 K throughout the experiment.

   Rationale: Since liquid R113 vaporizes at 320.7 K, a maximum ambient temperature of 320 K was selected. The lower bound of 240 K was selected because little thermophysical property data exists for liquid R113 below this temperature. No restrictions on the shape of the temperature profile were made since ambient temperature measurements can be incorporated into the computational model. A preferred requirement of maintaining the ambient temperature at 300 $\pm$5 K was selected because simulations show that the liquid surface and wall temperatures of the experiment change by not more than $\pm$1% over 1 hour in the case of a 305 K ambient temperature versus a 300 K ambient temperature.

2. Ambient Pressure

   Minimum Requirement: The ambient pressure shall be maintained at 14.7 $\pm$3 psia throughout the experiment.

   Rationale: To minimize leakage of R113 vapor through imperfect seals in the container, the ambient pressure should be maintained within about 20% of the initial gas pressure in the test cell. Pressure fluctuations should not

occur over a period of time less than that required for the gas pressure to equilibrate. This minimum fluctuation time is TBD. Another criterion for the ambient pressure requirement is based on keeping the flow velocity through a crack (orifice due to imperfect seal) in the test cell much less than the flow velocity in the test chamber. This analysis is TBD.

3. G-jitter

Minimum Requirement: The g-jitter level shall be kept at 10^{-4} g or less during the test in order to keep the amount of free surface deformation below 1.5 mm.

Preferred Requirement: The g-jitter level should be kept below 5% of the normal gravitational acceleration during the experiment.

Rationale: The assumed mean gravitational level of 5 x 10^{-4} g on the Shuttle is acceptable for the space-based experiments in order to achieve the required range of $\beta g L \Delta T$ and the Grashof number. The effect of g-jitter during the space-based experiments not only changes the buoyancy force in the experiment, but also affects the shape of the liquid free surface. By measuring the gravitational force during the experiment, the input of gravitational force in the computer simulation can be changed accordingly. However, the computational code still assumes a flat liquid-gas interface. Deformation of the liquid free surface will be minimized by the liquid-gas interface control system (the internal flanges—see Appendix A). However, the g-jitter level should be kept at 10^{-4} g or less at any time during the test to keep the local angle of the liquid surface below 0.04 radian. The preferred requirement of a 5% g-jitter level is desired in order to minimize the effect of g-jitter and thus simplify the analysis.

4. Interfacial Position

Minimum Requirement: The local angle of the liquid surface with respect to the plane that is perpendicular to the side walls shall be no greater than 0.04 radian.

Preferred Requirement: The above local angle of the liquid surface shall be no greater than 0.02 radian.

Rationale: Based on static considerations, the liquid surface deformation must be minimized so that the vertical component of liquid surface velocity is negligible compared to the horizontal component. The local angle of the liquid surface is

$$\theta \approx \tan\theta = \frac{V_y}{V_x} = \frac{L}{R-\delta}$$

where L is the radius (half-length) of the test cell, R is the radius of curvature of the liquid surface, and δ is the liquid surface deformation with respect to the height of the liquid in contact with the side walls. It can be shown that if $R \gg L$, then

$$\theta \ll 1 \quad \Rightarrow \quad \frac{\delta}{L} \ll 1$$

Therefore the requirements above on the maximum local angle of the liquid surface represent approximately a 4% and 2% maximum allowable liquid surface deformation with respect to the radius (or half-length) of the test cell.

3.4 Preliminary Hardware Concepts

The ground-based and space-based experiments consist of the following hardware:

1. Test cell: Plexiglass.
2. Fluids (liquid and gas): Silicon oil, R113, or water (liquid); air (gas).
3. Heater: Nichrome wire in ceramic cement.
4. Flow visualization system: Laser light sheet with tracer particles.
5. Temperature measurement system: Thermocouples (microgravity and 1-g), interferometry (1-g only).
6. Liquid-gas interface control system: Internal flanges.
7. Data acquisition and control system.

Hardware concepts for the ground-based and space-based experiments are given in Appendix A.

Chapter 4

Experimental Timeline

4.1 1-g Tests

No automation is required in the 1-g tests. A typical sequence of events is as follows:

1. Fill test cell to desired level with liquid and tracer particles.
2. Preheat heater until it reaches a steady temperature. This may be done either away from the test cell or in place.
3. Install heater and entire top of test cell.
4. Turn on laser for flow visualization system.
5. Turn on camera(s) for recording system.
6. Begin data collection.
7. Use second light sheet halfway through experiment for 2 minutes to check for axisymmetry (see Section 3.2). Replace light sheet into original position after this time.

8. End test run when surface temperature has reached a quasi-steady state (see note below) or after 1 hour.

As discussed in [1], a quasi-steady state condition is characterized by stabilized thermal and dynamic boundary layers. This occurs when the temperature and velocity on the liquid surface vary very slowly. Typically this takes between 1–10 minutes. A truly steady state condition would require several hours to reach and is not necessary for the purpose of the experiment. Therefore a run time of 1 hour has been selected. It should be noted that smoke tracers or tracer droplets remain in suspension for only approximately 10 minutes. Since injecting more vapor tracers will interfere with the flow, the 1 hour runs will only have vapor tracers for the first 10 minutes.

4.2 Drop Tower Tests

The procedure for the drop tower tests is slightly different than for the 1-g tests because the experimental package hangs above the drop tower for at least 3 minutes prior to the drop. During this hang-time the experiment is enclosed in a capsule and cannot be touched. Therefore an automated system must be used to inject tracer droplets into the gas phase immediately before the drop. A remote means is also required for turning on the heater while it is hanging in the drop capsule. The sequence of events is as follows:

1. Install heater and entire top of test cell. The heater should be turned off and at ambient temperature at this point.

2. Fill test cell to desired level with liquid and tracer particles.

3. Install experimental package into drop capsule. Raise capsule to its hanging position.

4. Turn on camera and monitor liquid in test cell.

5. After liquid becomes quiescent, turn on heater (remotely) and begin data collection.

6. Monitor heater temperature. Drop the experiment when the heater reaches the desired temperature.

7. Data collection ends after approximately 2–3 or 5–6 seconds (depending on which drop tower facility is used) when drop is complete.

4.3 Space-Based Tests

The procedure for these tests is the same as for the 1-g tests, except that the liquid fill and tracer droplet/particle injection and stirring are done by automated systems. A crewmember may be required only to turn on the heater, monitor its temperature until it reaches a quasi-steady state, turn on and monitor the liquid fill system until the desired liquid fill level is achieved, and then press one button to simultaneously: inject and stir tracers, activate light sheet, and turn on data acquisition system. Each experiment will take 1 hour after the initial 20 minute set-up time.

Chapter 5

Planned Data Analysis

The following data collected in the experiments will be used for analysis:

1. Video or movie films as the flow observation record.
2. A tape (memory size TBD for the three experiment settings) with the recording of the thermocouple outputs.
3. G-jitter and acceleration data during the tests (space-based only).
4. Comments of the test operators.

The films will be reviewed to observe general flow patterns and free surface behaviors. The particle motions will be studied by a motion analyzer to quantify the flow visualization at various times. The thermocouple outputs will be converted to temperatures. The temperatures of the heater, the ambient air, and the fluid at various locations (ground-based tests only) will be plotted as a function of time. Wall temperatures at various locations will also be plotted against time. For the 1-g tests, the surface temperature distribution will be plotted for various times. Results of the data analysis will be compared with the predictions of the computational model. Ground-based test results will be used to aid in the design of the space-based experiments.

Chapter 6

The Numerical Model

6.1 Description of Numerical Model

The finite-difference procedure applied to the governing equations in the gas and liquid phases utilizes the SIMPLE algorithm [3] with the SIMPLEC modification [14]. The important operations of this algorithm, in the order of their execution, are (taken from [3]):

1. Guess the pressure field p^*.
2. Solve the momentum equations to obtain u^* and v^*.
3. Solve the p' equation.
4. Calculate p by adding p' to p^*.
5. Calculate u and v from their starred values using the velocity-correction formulas.
6. Solve the discretization equation for other ϕ's (such as enthalpy and mass fraction of species) if they influence the flow field through fluid properties, source terms, etc.

7. Treat the corrected pressure p as a new guessed pressure p^*, return to step 2, and repeat the whole procedure until a converged solution is obtained.

The numerical model uses primitive variables (u, v, p, h), a staggered mesh [3], and variable thermophysical properties (density, viscosity, etc.) in both phases. The effects of surface tension, evaporation, radiation, and wall thermal inertia are incorporated into the computational code. The user has the option of using an explicit one-dimensional or two-dimensional wall conductivity calculation (the latter takes into account heat transfer between the outer walls and the environment via Newton Cooling). All surfaces are assumed to have an emissivity of 1.0. The calculation of the radiative heat transfer between elementary rings of the enclosure and liquid surface has been described previously by Abramzon, Edwards, and Sirignano [1]. The program also accounts for the total pressure variations in the gas phase. This option is very important for the enclosed container simulations because the total gas pressure is continuously increasing during the heating and vaporization processes. The code also allows for local refining of the finite-difference grid at regions where the field gradients are large and better resolution of the problem is needed.

The following variables are allowed to be changed parametrically:

1. Liquid fill level.
2. Container dimensions, including wall thickness.
3. Thermal driving potential (heater temperature, position, and size).
4. Fluid properties.
5. Gravity level.

The gas and liquid phase solutions are time-split in that the solution at time t represents the gas phase at time t and the liquid phase at time $t + \frac{1}{2}\Delta t$ (where Δt is the time step). At the liquid-vapor interface, values of liquid temperature and velocity are used for the gas phase solution while values of gradients of gas temperatures and velocities are used for the liquid phase solution. Because the prediction of the liquid-vapor interfacial shape is complex, the model presently considers only a flat liquid-vapor interface. The sequential calculation procedure for each time step is as follows:

- Determine wall boundary temperatures using explicit scheme:

    1. Calculate total heat fluxes (radiative + conductive) to the walls in the gas phase based on temperatures at time t.

    2. Calculate conductive heat fluxes to the walls in the liquid phase based on temperatures at time t.

    3. Use explicit scheme to calculate wall temperatures based on above heat flux data. Newton's law of cooling is used as a boundary condition for the outside of the walls to take into account natural convection to the environment.

- Determine gas phase solution at time $t + \Delta t$:

    1. Calculate gas phase properties at beginning of time step. Only values of c_p are updated during the internal iteration cycle. This helps stabilize the solution. Values of c_p are updated in order to update values of enthalpy.

2. Perform internal iteration loop for gas phase (using SIMPLEC algorithm). Boundary values of wall temperatures (from explicit solution) and liquid temperatures and velocities (from time $t + \frac{1}{2}\Delta t$) are used.

- Determine liquid phase solution at time $t + \frac{3}{2}\Delta t$:

1. Calculate liquid phase properties at beginning of time step. Only values of c_p are updated during the internal iteration cycle.

2. Perform internal iteration loop for liquid phase (SIMPLEC algorithm). Boundary values of wall temperatures (from explicit solution) and gradients of gas temperatures and velocities (from time $t + \Delta t$) are used (e.g., heat and stress balances at interface). The bottom of the liquid phase is assumed to be isothermal at the reference temperature.

As previously mentioned, the resulting solution for time $t+\Delta t$ actually represents the gas phase at time $t+\Delta t$ and the liquid phase at time $t+\frac{3}{2}\Delta t$. The calculation procedure for the single-phase simulation is similar to the above except that a relatively thick wall is used at the bottom of the gas phase with the isothermal boundary condition being applied at the bottom of this wall.

Calculations are typically performed with a 22 x 22 mesh in each phase for aspect ratios equal to 1.0. Since two boundary nodes are used in each direction, there are 20 x 20 internal cells in this mesh. Denser meshes were employed to test grid sensitivity. For one simulation, three runs were made with mesh sizes of 22 x 22, 32 x 32, and 42 x 42. The resulting stream function contour plots after $t = 100$ seconds were qualitatively identical. Quantitatively, the local maxima of the stream function differed by only 1% between the 32 x 32 and 42 x 42 meshes, while these values differed

by 8–10% between the 22 x 22 and 32 x 32 meshes. The time step was typically about 0.05 second and required about 8 seconds of CPU time on a VAX-11/780 computer for the two-phase calculations, and about 4 seconds of CPU time for the single-phase calculations. For the single-phase simulations presented in Chapter 7, a 22 x 42 grid was used with a 0.01 second time step.

6.2 Governing Equations

Aside from the continuity equation, which we solve for by iterating with the pressure correction equation, the following conservation equations are solved in nondimensional form: momentum equations (u- and v-), the energy equation (for excess enthalpy), and species equations (for mass fractions). Each equation is written in a general form.

6.2.1 The General Conservation Equation

The general form of the dimensional conservation equation is as follows:

$$\frac{\partial}{\partial t'}(\rho'\phi') + \frac{1}{r'}\frac{\partial}{\partial x'}\left[r'\left(\rho' V_x'\phi' - \Gamma_\phi'\frac{\partial \phi'}{\partial x'}\right)\right] + \frac{\partial}{\partial y'}\left(\rho' V_y'\phi' - \Gamma_\phi'\frac{\partial \phi'}{\partial y'}\right) = S_\phi' \tag{6.1}$$

where

ϕ' = the quantity of interest (e.g., u', Y_i', h_1')

Γ_ϕ' = dimensional diffusion coefficient for ϕ' (e.g., μ', $k'/\bar{c}_p'$)

$$S'_\phi = \text{dimensional source term for } \phi'$$

$$r' = \begin{cases} x' \text{ for cylindrical coordinates} \\ 1 \text{ for rectangular coordinates} \end{cases}$$

To make equation (6.1) nondimensional, use:

$$t \equiv t'/t_*,\ \phi \equiv \phi'/\phi_*,\ x \equiv x'/L_*,\ y \equiv y'/L_*,$$

$$V_x \equiv V'_x/U_* \text{ and } V_y \equiv V'_y/U_* \text{ where } U_* \equiv L_*/t_*,$$

$$\Gamma_\phi \equiv \Gamma'_\phi/\Gamma_* \text{ (where } \Gamma_* \equiv \mu_* \text{ for all } \phi),\ g \equiv g' t_*/U*,$$

$$S_\phi \equiv \frac{S'_\phi t_*}{\rho_* \phi_*},\ P \equiv P'/(\Delta P)_*,\ \tau \equiv \frac{\tau' L_*}{\mu_* U_*},\ T \equiv T'/T_*, \text{ and}$$

$$T_1 \equiv T'_1/T_* \text{ where } T'_1 = (\Delta T)' = T' - T_* \text{ and } (\Delta T)_* = T_* \tag{6.2}$$

By multiplying equation (6.1) by

$$\frac{t_*}{\rho_* \phi_*} = \frac{L_*}{\rho_* U_* \phi_*}$$

and noting that

$$\frac{\Gamma_*}{\rho_* U_* L_*} = \frac{\mu_*/\rho_*}{U_* L_*} \equiv 1/Re_*$$

we get the following nondimensional general conservation equation:

$$\frac{\partial(\rho\phi)}{\partial t} + \frac{1}{r}\frac{\partial}{\partial x}\left[r\left(\rho V_x \phi - \frac{1}{Re_*}\Gamma_\phi \frac{\partial \phi}{\partial x}\right)\right]$$
$$+ \frac{\partial}{\partial y}\left(\rho V_y \phi - \frac{1}{Re_*}\Gamma_\phi \frac{\partial \phi}{\partial y}\right) = S_\phi \tag{6.3}$$

6.2.2 Continuity Equation

The continuity equation in nondimensional form is

$$\frac{\partial \rho}{\partial t} + \vec{\nabla}\cdot(\rho \vec{V}) = 0$$

In cylindrical coordinates with $\partial/\partial\theta = 0$, this becomes

$$\frac{\partial \rho}{\partial t} + \frac{1}{r}\frac{\partial}{\partial r}(\rho r V_r) + \frac{\partial}{\partial y}(\rho V_y) = 0$$

The rectangular coordinate equation and the cylindrical coordinate equation can be combined by

$$\frac{\partial \rho}{\partial t} + \frac{1}{r}\frac{\partial}{\partial x}(r\rho u) + \frac{\partial}{\partial y}(\rho v) = 0 \tag{6.4}$$

where $r = x$ for the cylindrical geometry, $r = 1$ for the planar geometry, $u = V_r = V_x$, and $v = V_y$. This designation will be assumed for the remainder of this document. Note also that equation (6.4) is in the general form of equation (6.3) with

$$\phi = 1,\ \Gamma_\phi = 0, \text{ and } S_\phi = 0$$

6.2.3 Momentum Equations

Omitting the single quote ($'$) superscripts, the dimensional momentum equation is

$$\rho\frac{D\vec{V}}{Dt} = \rho\frac{\partial \vec{V}}{\partial t} + \rho(\vec{V}\cdot\vec{\nabla})\vec{V} = -\nabla P + [\vec{\nabla}\cdot\vec{\tau}] + \rho\vec{g} \tag{6.5}$$

where $[\vec{\nabla}\cdot\vec{\tau}]$ is not a simple divergence because of the tensorial nature of $\vec{\tau}$; $\vec{\tau}$ is the stress tensor defined for the cylindrical geometry as (convention opposite to [15]):

$$\tau_{rr} = \tau_{xx} = \mu\left[2\frac{\partial u}{\partial x} - \frac{2}{3}\vec{\nabla}\cdot\vec{V}\right] \tag{6.6}$$

$$\tau_{\theta\theta} = \mu\left[2\frac{u}{r} - \frac{2}{3}\vec{\nabla}\cdot\vec{V}\right] \tag{6.7}$$

(note $\tau_{\theta\theta} = 0$ for planar geometry)

$$\tau_{yy} = \mu\left[2\frac{\partial v}{\partial y} - \frac{2}{3}\vec{\nabla}\cdot\vec{V}\right] \tag{6.8}$$

$$\tau_{r\theta} = \tau_{\theta r} = \tau_{\theta y} = \tau_{y\theta} = 0 \tag{6.9}$$

$$\tau_{yx} = \tau_{xy} = \mu\left[\frac{\partial v}{\partial x} + \frac{\partial u}{\partial y}\right] \tag{6.10}$$

The nondimensional form of the momentum equations will now be treated separately for the r (or x) and y directions.

u-momentum equation

Equations (6.5) and (6.6)-(6.10) for the r (or x) direction give

$$\rho\left(\frac{\partial u}{\partial t}+u\frac{\partial u}{\partial x}+v\frac{\partial u}{\partial y}\right)=-\frac{\partial P}{\partial x}+\left[\frac{1}{r}\frac{\partial}{\partial x}(r\tau_{xx})-\frac{\tau_{\theta\theta}}{r}+\frac{\partial \tau_{yx}}{\partial y}\right]+\rho\overbrace{g_x}^{=0} \tag{6.11}$$

The left hand side of this equation can be re-written with the aid of the continuity equation as

$$\rho\left(\frac{\partial u}{\partial t}+u\frac{\partial u}{\partial x}+v\frac{\partial u}{\partial y}\right)+\overbrace{\left[\frac{\partial \rho}{\partial t}+\frac{1}{r}\frac{\partial}{\partial x}(r\rho u)+\frac{\partial}{\partial y}(\rho v)\right]}^{=0}u=$$

$$\begin{aligned}
&=\frac{\partial(\rho u)}{\partial t}+u\left[\frac{1}{r}\frac{\partial}{\partial x}(r\rho u)+\frac{\partial}{\partial y}(\rho v)\right]+\rho u\frac{\partial u}{\partial x}+\rho v\frac{\partial u}{\partial y}\\
&=\frac{\partial(\rho u)}{\partial t}+\left[\frac{u}{r}\frac{\partial}{\partial x}(r\rho u)+\rho u\frac{\partial u}{\partial x}\right]+\left[u\frac{\partial}{\partial y}(\rho v)+\rho v\frac{\partial u}{\partial y}\right]\\
&=\frac{\partial(\rho u)}{\partial t}+\frac{1}{r}\frac{\partial}{\partial x}(r\rho u\cdot u)+\frac{\partial}{\partial y}(\rho v u)\\
&=\frac{\partial(\rho\phi)}{\partial t}+\frac{1}{r}\frac{\partial}{\partial x}(r\rho u\phi)+\frac{\partial}{\partial y}(\rho v\phi)
\end{aligned} \tag{6.12}$$

where $\phi=u$.

Substituting equation (6.12) into equation (6.11) gives

$$\frac{\partial(\rho\phi)}{\partial t}+\frac{1}{r}\frac{\partial}{\partial x}(r\rho u\phi)+\frac{\partial}{\partial y}(\rho v\phi)=-\frac{\partial P}{\partial x}+\left[\frac{1}{r}\frac{\partial}{\partial x}(r\tau_{xx})-\frac{\tau_{\theta\theta}}{r}+\frac{\partial \tau_{yx}}{\partial y}\right]$$

To get this equation into the standard form, we subtract

$$\frac{1}{r}\frac{\partial}{\partial x}\left(r\mu\frac{\partial u}{\partial x}\right)+\frac{\partial}{\partial y}\left(\mu\frac{\partial u}{\partial y}\right)$$

from both sides of the equation to get

$$\frac{\partial(\rho\phi)}{\partial t} + \frac{1}{r}\frac{\partial}{\partial x}\left[r\left(\rho u\phi - \mu\frac{\partial\phi}{\partial x}\right)\right] + \frac{\partial}{\partial y}\left(\rho v\phi - \mu\frac{\partial\phi}{\partial y}\right) =$$

$$= -\frac{\partial P}{\partial x} + \frac{1}{r}\frac{\partial}{\partial x}\left[r\left(\tau_{xx} - \mu\frac{\partial u}{\partial x}\right)\right] + \frac{\partial}{\partial y}\left(\tau_{yx} - \mu\frac{\partial u}{\partial y}\right) - \frac{\tau_{\theta\theta}}{r}$$

Denoting the right hand side of this equation as S'_ϕ and letting

$$\phi = u,\ \Gamma_\phi = \mu$$

the above dimensional equation can be multiplied by

$$\frac{t_*}{\rho_*\phi_*} = \frac{L_*}{\rho_* u_* \phi_*}$$

to get the nondimensional u-momentum equation:

$$\frac{\partial(\rho\phi)}{\partial t} + \frac{1}{r}\frac{\partial}{\partial x}\left[r\left(\rho u\phi - \frac{\Gamma_\phi}{Re_*}\frac{\partial\phi}{\partial x}\right)\right] + \frac{\partial}{\partial y}\left(\rho v\phi - \frac{\Gamma_\phi}{Re_*}\frac{\partial\phi}{\partial y}\right) = \frac{S'_\phi t_*}{\rho_*\phi_*} \tag{6.13}$$

Therefore the nondimensional u-momentum equation is in the general form of equation (6.3) with

$$\phi = u,\ \Gamma_\phi = \mu, \text{ and}$$

$$S_\phi = \frac{t_*}{\rho_* u_*}\left\{-\frac{\partial P'}{\partial x'} + \frac{1}{r'}\frac{\partial}{\partial x'}\left[r'\left(\tau'_{xx} - \mu'\frac{\partial u'}{\partial x'}\right)\right]\right.$$
$$\left. + \frac{\partial}{\partial y'}\left(\tau'_{yx} - \mu'\frac{\partial u'}{\partial y'}\right) - \frac{\tau'_{\theta\theta}}{r'}\right\} \tag{6.14}$$

where the subscript * denotes a reference quantity and the superscript ′ denotes a dimensional quantity. The source term S_ϕ in equation (6.14) will be defined in terms of nondimensional quantities in Section 6.3.

v-momentum equation

Equations (6.5)-(6.10) for the y-direction give

$$\rho\left(\frac{\partial v}{\partial t}+u\frac{\partial v}{\partial x}+v\frac{\partial v}{\partial y}\right)=-\frac{\partial P}{\partial y}+\left[\frac{1}{r}\frac{\partial}{\partial x}(r\tau_{xy})+\frac{\partial \tau_{yy}}{\partial y}\right]+\rho g_y \qquad (6.15)$$

where all quantities above are dimensional. Again, the left hand side of this equation can be rewritten using the continuity equation as

$$\begin{aligned}\rho\frac{Dv}{Dt} &= \frac{\partial(\rho v)}{\partial t}+\left[\frac{v}{r}\frac{\partial}{\partial x}(r\rho u)+\rho u\frac{\partial v}{\partial x}\right]+\left[v\frac{\partial}{\partial y}(\rho v)+\rho v\frac{\partial v}{\partial y}\right]\\ &= \frac{\partial(\rho v)}{\partial t}+\frac{1}{r}\frac{\partial}{\partial x}(r\rho u\cdot v)+\frac{\partial}{\partial y}(\rho v\cdot v)\\ &= \frac{\partial(\rho\phi)}{\partial t}+\frac{1}{r}\frac{\partial}{\partial x}(r\rho u\phi)+\frac{\partial}{\partial y}(\rho v\phi)\end{aligned}$$

Hence it can easily be seen that the nondimensional v-momentum equation can be written in the general form of equation (6.3) with

$$\phi = v,\ \Gamma_\phi = \mu, \text{ and}$$

$$\begin{aligned}S_\phi = \frac{t_*}{\rho_* u_*}\Bigg\{&-\frac{\partial P'}{\partial y'}+\frac{1}{r'}\frac{\partial}{\partial x'}\left[r'\left(\tau'_{xy}-\mu'\frac{\partial v'}{\partial x'}\right)\right]\\ &+\frac{\partial}{\partial y'}\left(\tau'_{yy}-\mu'\frac{\partial v'}{\partial y'}\right)+\rho' g'_y\Bigg\}\end{aligned} \qquad (6.16)$$

Note that in equation (6.16), $g'_y = -|g'|$ for the given orientation (e.g., for earth gravity $g'_y = -9.81$ m/s^2).

6.2.4 Energy Equation

The thermal energy equation is solved in terms of the excess enthalpy of the mixture. The derivation of this equation appears in Appendix B while the final result

[in the form of equation (6.3)] is given below. The excess enthalpy of the i^{th} species ($h'_{i,\text{excess}}$) and of the mixture (h'_1) is defined by

$$h'_{i,\text{excess}} \equiv \overline{c}'_{p_i}(T' - T^{o'}) = \overline{c}'_{p_i} T'_1 \tag{6.17}$$

and

$$h'_1 = \sum_i Y'_i h'_{1,i} = \overline{c}'_p T'_1 = h' - h^{o'} \tag{6.18}$$

where

$$\begin{aligned}
h'_i &= h_i^{o'} + h'_{i,\text{excess}} = h_i^{o'} + h'_{1,i} \\
h_i^{o'} &= h'_i(T^{o'}) = \text{formation enthalpy} \\
T^{o'} &= T_* = 300 \text{ K (reference temperature)} \\
h' &= \sum_i Y'_i h'_i \\
h^{o'} &= \sum_i Y'_i h_i^{o'} \\
\overline{c}'_{p_i} &= \left(\frac{1}{T' - T^{o'}}\right) \int_{T^{o'}}^{T'} c'_{p_i}(T')dT' \\
\overline{c}'_p &= \sum_i Y'_i \overline{c}'_{p_i}
\end{aligned}$$

The dimensional energy equation written in the standard form of equation (6.3) using the mass-weighted average velocity components (u' and v') is

$$\begin{aligned}
&\frac{\partial}{\partial t'}(\rho' h'_1) + \frac{1}{r'}\frac{\partial}{\partial x'}\left[r'\left(\rho' u' h'_1 - \frac{k'}{\overline{c}'_p}\frac{\partial h'_1}{\partial x'}\right)\right] \\
&\quad + \frac{\partial}{\partial y'}\left(\rho' v' h'_1 - \frac{k'}{\overline{c}'_p}\frac{\partial h'_1}{\partial y'}\right) = S'_\phi
\end{aligned} \tag{6.19}$$

where

$$\begin{aligned}
S'_\phi = {} & \frac{DP'}{Dt'} + Q'_{\text{ch}} + \vec{\nabla}' \cdot \left\{\rho' \mathcal{D}'_{ij} T'_1 \left[\sum_i (\overline{c}'_{p_i} \nabla' Y'_i) - \overline{Le}' \nabla' \overline{c}'_p\right]\right\} \\
& + \mu' \Phi' + \dot{Q}'_V - \frac{1}{2}\rho' \frac{D'}{Dt'}\left(\sum_i Y'_i \vec{V}'_i \cdot \vec{V}'_i\right) \\
& - \vec{\nabla}' \cdot \left\{\rho' \sum_i [Y'_i \vec{V}'_i (\vec{v}'_A \cdot \vec{V}'_i) + \frac{1}{2} Y'_i \vec{V}'_i (\vec{V}'_i \cdot \vec{V}'_i)]\right\} + \vec{\nabla}' \cdot \sum_i P'_i \vec{V}'_i
\end{aligned} \tag{6.20}$$

and

$$Q'_{\mathrm{ch}} \equiv -\sum_i (h_i^\circ r_i''')' = \text{heat released by chemical reaction (calculated at temperature } T^{o'}) \tag{6.21}$$

$$\mathcal{D}'_{ij} = \text{binary diffusion coefficient}$$

$$\overline{Le}' = \frac{k'/\overline{c}'_p}{\rho' \mathcal{D}'_{ij}} = \text{Lewis number of mixture} \tag{6.22}$$

$$\Phi' = \text{viscous dissipation function (see [16], eqn A.16)}$$

$$\dot{Q}'_V = \frac{d\dot{Q}'}{dV'} = \text{volumetric heat source term (energy production per unit volume per unit time)}$$

$$\vec{V}'_i = -\frac{\mathcal{D}'_{ij} \nabla' Y'_i}{Y'_i} \tag{6.23}$$

$$\vec{v}'_A = \sum_i Y'_i \vec{v}'_i \tag{6.24}$$

$$\vec{v}'_i = \vec{v}'_A + \vec{V}'_i \tag{6.25}$$

Note that $\vec{v}'_i$ is the local average velocity of species i (relative to stationary coordinate axes), $\vec{v}'_A$ is the mass-weighted average velocity of the fluid mixture, and $\vec{V}'_i$ is the diffusion velocity of species i. The nondimensional form of equation (6.19) is

$$\frac{\partial(\rho\phi)}{\partial t} + \frac{1}{r}\frac{\partial}{\partial x}\left[r\left(\rho u\phi - \frac{\Gamma_\phi}{Re_*}\frac{\partial\phi}{\partial x}\right)\right]$$

$$+ \frac{\partial}{\partial y}\left(\rho v\phi - \frac{\Gamma_\phi}{Re_*}\frac{\partial\phi}{\partial y}\right) = \frac{t_*}{\rho_* c_{p_*} T_*} S'_\phi$$

with

$$\phi = h_1 = \frac{h'_1}{c_{p_*} T_*} \qquad \text{and} \qquad \Gamma_\phi = \frac{k'/\overline{c}'_p}{\mu_*} \tag{6.26}$$

The source term

$$S_\phi = \frac{t_*}{\rho_* c_{p_*} T_*} S'_\phi$$

in equation (6.26) [see also equation (6.20)] will be defined in terms of nondimensional quantities in Section 6.3.

6.2.5 Species Equation

One species equation must be written for each species in the gas phase: fuel vapor, oxygen, and products. These equations are used in the code if vaporization effects are included (user option). For diffusion in a nonstationary medium, the total mass flux, $\vec{n_i}$, of species i is given by (all quantities dimensional unless otherwise specified):

$$\vec{n_i} = \rho_{\text{mix}} Y_i \vec{v'} - \rho_{\text{mix}} \mathcal{D}_{ij} \nabla Y_i = \rho Y_i (\vec{v'} + \vec{V_i}) \tag{6.27}$$

If we designate r_i''' as the rate of production of the i^{th} component [kg/(m^3·s)], a two-dimensional mass balance gives

(mass accumulated = mass produced + flux in − flux out)

$$\left[(\rho Y_i)_{t+\Delta t} - (\rho Y_i)_t\right] \Delta x \Delta y =$$
$$r_i''' \Delta x \Delta y \Delta t + (n_x - n_{x+\Delta x}) \Delta y \Delta t + (n_y - n_{y+\Delta y}) \Delta x \Delta t$$

Dividing by $\Delta x \Delta y \Delta t$ and taking the limit as $\Delta x, \Delta y, \Delta t \to 0$ gives

$$\frac{\partial}{\partial t}(\rho Y_i) = -\vec{\nabla} \cdot \vec{n_i} + r_i''' \tag{6.28}$$

Substituting equation (6.27) into (6.28) and using the general form applicable to both cylindrical and rectangular coordinates yields

$$\frac{\partial}{\partial t}(\rho Y_i) + \vec{\nabla} \cdot (\rho \vec{v'} Y_i - \rho \mathcal{D}_{ij} \nabla Y_i) = r_i'''$$

$$\Rightarrow \quad \frac{\partial}{\partial t'}(\rho' Y_i') + \frac{1}{r'} \frac{\partial}{\partial x'} \left[r' \left(\rho' u' Y_i' - \rho' \mathcal{D}_{ij}' \frac{\partial Y_i'}{\partial x'} \right) \right]$$
$$+ \frac{\partial}{\partial y'} \left(\rho' v' Y_i' - \rho' \mathcal{D}_{ij}' \frac{\partial Y_i'}{\partial y'} \right) = \left(r_i''' \right)' \tag{6.29}$$

All quantities in equation (6.29) are dimensional. To make the equation dimensionless, multiply it by

$$\frac{t_*}{\rho_* Y_*} = \frac{L_*}{\rho_* U_* Y_*}$$

to get

$$\frac{\partial}{\partial t}(\rho Y_i) + \frac{1}{r}\frac{\partial}{\partial x}\left[r\left(\rho u Y_i - \frac{\mu_*}{\rho_* U_* L_*}\cdot\frac{\rho' \mathcal{D}'_{ij}}{\mu_*}\frac{\partial Y_i}{\partial x}\right)\right]$$
$$+\frac{\partial}{\partial y}\left(\rho v Y_i - \frac{\mu_*}{\rho_* U_* L_*}\cdot\frac{\rho' \mathcal{D}'_{ij}}{\mu_*}\frac{\partial Y_i}{\partial y}\right) = \frac{t_*}{\rho_* Y_*}\left(r_i'''\right)'$$

Using the Schmidt number, $Sc_* = \mu_*/\rho_* \mathcal{D}_*$, and the nondimensionalization

$$\begin{aligned} Y_i &= Y'/Y_* \qquad (= \phi \text{ and } Y_* \equiv 1) \\ \rho \mathcal{D}_{ij}/Sc_* &= \rho' \mathcal{D}'_{ij}/\mu_* \qquad (= \Gamma_\phi) \end{aligned} \tag{6.30}$$

we obtain the result

$$\frac{\partial}{\partial t}(\rho\phi) + \frac{1}{r}\frac{\partial}{\partial x}\left[r\left(\rho u\phi - \frac{\Gamma_\phi}{Re_*}\frac{\partial \phi}{\partial x}\right)\right]$$
$$+\frac{\partial}{\partial y}\left(\rho v\phi - \frac{\Gamma_\phi}{Re_*}\frac{\partial \phi}{\partial y}\right) = \frac{t_*}{\rho_* Y_*}\left(r_i'''\right)'$$

This is in the general form of equation (6.3) with

$$\begin{aligned} \phi &= Y_i \\ \Gamma_\phi &= \rho \mathcal{D}_{ij}/Sc_* \\ S_\phi &= \frac{t_*}{\rho_* Y_*}\left(r_i'''\right)' = \frac{t_*}{\rho_*}\left(r_i'''\right)' \end{aligned} \tag{6.31}$$

The computational model currently includes vaporization (and thus multicomponents in the gas phase) but not chemical reaction. Therefore $S_\phi = 0$ in equation (6.31). In the future, chemical reactions may be incorporated in the model with a simple one-step reaction and an Arrhenius expression for the specific rate constant. The source term for this one-step chemical reaction is derived in Appendix C.

6.3 Source Term Approximations

The nondimensional source terms in the governing equations were defined in Section 6.2 in terms of dimensional variables and reference quantities. The nondimensionalization of these source terms is treated in this section. Simplified source terms are used in the computational model. The approximations which led to these simplified terms are also given in this section.

6.3.1 Momentum Equations

With the exception of the buoyancy term in the v-momentum equation, the source term of the u- and v-momentum equations are treated similarly.

u-momentum equation

The source term in the u-momentum equation was given by equation (6.14):

$$S_\phi = \frac{t_*}{\rho_* u_*}\left\{-\frac{\partial P'}{\partial x'} + \frac{1}{r'}\frac{\partial}{\partial x'}\left[r'\left(\tau'_{xx} - \mu'\frac{\partial u'}{\partial x'}\right)\right] + \frac{\partial}{\partial y'}\left(\tau'_{yx} - \mu'\frac{\partial u'}{\partial y'}\right) - \frac{\tau'_{\theta\theta}}{r'}\right\}$$

Using the definitions of the nondimensional variables in equation (6.2), equation (6.14) becomes

$$S_\phi = -\frac{(\Delta P)_*}{\rho_* U_*^2}\frac{\partial P}{\partial x} + \frac{\mu_*}{\rho_* U_* L_*}\left\{\frac{1}{r}\frac{\partial}{\partial x}\left[r\left(\tau_{xx} - \mu\frac{\partial u}{\partial x}\right)\right] + \frac{\partial}{\partial y}\left(\tau_{yx} - \mu\frac{\partial u}{\partial y}\right) - \frac{\tau_{\theta\theta}}{r}\right\}$$

Defining

$$Eu_* \equiv \frac{(\Delta P)_*}{\rho_* U_*^2} \tag{6.32}$$

and noting that

$$\frac{\mu_*}{\rho_* U_* L_*} \equiv 1/Re_* \tag{6.33}$$

the nondimensional source term for the u-momentum equation becomes

$$\begin{aligned} S_\phi &= -Eu_* \left(\frac{\partial P}{\partial x}\right) + \frac{1}{Re_*}\left\{\frac{1}{r}\frac{\partial}{\partial x}\left[r\left(\tau_{xx} - \mu\frac{\partial u}{\partial x}\right)\right]\right. \\ &\quad \left. + \frac{\partial}{\partial y}\left(\tau_{yx} - \mu\frac{\partial u}{\partial y}\right) - \frac{\tau_{\theta\theta}}{r}\right\} \end{aligned} \tag{6.34}$$

v-momentum equation

Before the source term in the v-momentum equation is evaluated, we must first examine how we define P' in the computational model (pressure splitting). The total pressure is divided into three parts: global pressure (P_o'), dynamic pressure (P_1'), and the hydrostatic pressure ($\rho_* g_y' y' = -\rho_* g' y'$). Hence

$$P' = P_o'(t) + P_1'(x, y) - \rho_* g' y' \tag{6.35}$$

While global pressure is used to calculate density in the gas phase, only the dynamic pressure appears in the momentum and pressure correction equations. In the u-momentum equation, the global pressure and the hydrostatic term do not appear because only the gradient in the x-direction appears. The global pressure also does not appear in the v-momentum equation. However, the hydrostatic term in equation (6.35) contributes to the pressure gradient in the y-direction. Therefore, the source term in the v-momentum equation becomes [from equation (6.16)]

$$S_\phi = \frac{t_*}{\rho_* u_*}\left\{-\frac{\partial P_1'}{\partial y'} + \frac{1}{r'}\frac{\partial}{\partial x'}\left[r'\left(\tau_{xy}' - \mu'\frac{\partial v'}{\partial x'}\right)\right]\right.$$
$$\left. + \frac{\partial}{\partial y'}\left(\tau_{yy}' - \mu'\frac{\partial v'}{\partial y'}\right) + g'(\rho_* - \rho')\right\} \tag{6.36}$$

In the above equation, g_y' from equation (6.16) has been replaced by $-g'$ where $g' \geq 0$. Using equations (6.2), (6.32), and (6.33), the nondimensional source term for the v-momentum equation becomes (note P is understood now to be the dynamic pressure)

$$S_\phi = -Eu_*\left(\frac{\partial P}{\partial y}\right) + \frac{1}{Re_*}\left\{\frac{1}{r}\frac{\partial}{\partial x}\left[r\left(\tau_{xy} - \mu\frac{\partial v}{\partial x}\right)\right]\right.$$
$$\left. + \frac{\partial}{\partial y}\left(\tau_{yy} - \mu\frac{\partial v}{\partial y}\right)\right\} + g(1-\rho) \tag{6.37}$$

If the user chooses to run a simulation using the Boussinesq approximation, then the last term in equation (6.37) is replaced by $g(T - 1.0)$ for the gas phase and $g\beta' T_*(T - 1.0)$ for the liquid phase (where T is evaluated at the center of the v-momentum control volume).

6.3.2 Energy Equation

The dimensional source term of the energy equation (omitting the primes on the right hand side of the equation) was previously given by equation (6.20) as

$$S_\phi' = \frac{DP}{Dt} + Q_{\text{ch}} + \vec{\nabla}\cdot\left\{\rho\mathcal{D}_{ij}T_1\left[\sum_i(\overline{c}_{p_i}\nabla Y_i) - \overline{Le}\nabla\overline{c}_p\right]\right\}$$
$$+\mu\Phi + \dot{Q}_V - \frac{1}{2}\rho\frac{D}{Dt}\left(\sum_i Y_i\vec{V}_i\cdot\vec{V}_i\right)$$
$$-\vec{\nabla}\cdot\left\{\rho\sum_i[Y_i\vec{V}_i(\vec{v}\cdot\vec{V}_i) + \frac{1}{2}Y_i\vec{V}_i(\vec{V}_i\cdot\vec{V}_i)]\right\} + \vec{\nabla}\cdot\sum_i P_i\vec{V}_i$$

This source term expression may be simplified by the following approximations:

1. Low Mach number flow with no explosions.
2. All species' average heat capacitances are equal and do not vary spatially for a given time t.
3. Negligible viscous dissipation.
4. No volumetric heat sources or sinks.
5. Terms with a diffusion velocity of order two or more are negligible.
6. The molecular weights of all species are equal.

The first approximation above implies that

$$\frac{DP}{Dt} = \frac{\partial P}{\partial t} + (\vec{v}\cdot\vec{\nabla})P \approx \frac{\partial P}{\partial t} \tag{6.38}$$

The approximation that at a given t, $\bar{c}_{p_i} \approx$ constant yields

$$\sum_i \bar{c}_{p_i}\nabla Y_i \approx \sum_i \nabla(\bar{c}_{p_i}Y_i) = \nabla\sum_i(\bar{c}_{p_i}Y_i) = \nabla\bar{c}_p \tag{6.39}$$

However, near the heater in the gas phase, large temperature gradients can cause $\bar{c}_{p_i}$ to vary by about 5% between the adjacent cells. Thus if the approximation of equation (6.39) were not made, we can still introduce a different assumption by first writing

$$\sum_i \bar{c}_{p_i}\nabla Y_i - \overline{Le}\nabla\bar{c}_p = (1-\overline{Le})\sum_i(\bar{c}_{p_i}\nabla Y_i) - \overline{Le}\sum_i\left(Y_i\frac{\partial\bar{c}_{p_i}}{\partial T}\nabla T\right) \tag{6.40}$$

The derivation of equation (6.40) is as follows:

$$\overline{c}_p = \sum_i Y_i \overline{c}_{p_i} \quad \Rightarrow \quad \nabla \overline{c}_p = \sum_i (\overline{c}_{p_i} \nabla Y_i + Y_i \nabla \overline{c}_{p_i})$$

and

$$\nabla \overline{c}_{p_i} = \frac{\partial \overline{c}_{p_i}}{\partial T} \nabla T$$

so that

$$\begin{aligned} &\sum_i \overline{c}_{p_i} \nabla Y_i - \overline{Le} \nabla \overline{c}_p = \\ &= \sum_i \overline{c}_{p_i} \nabla Y_i - \overline{Le} \left[\sum_i \overline{c}_{p_i} \nabla Y_i + \sum_i \left(Y_i \frac{\partial \overline{c}_{p_i}}{\partial T} \nabla T \right) \right] \\ &= (1 - \overline{Le}) \sum_i (\overline{c}_{p_i} \nabla Y_i) - \overline{Le} \sum_i \left(Y_i \frac{\partial \overline{c}_{p_i}}{\partial T} \nabla T \right) \end{aligned}$$

From equation (6.40) it is clear that if we allow $\overline{c}_{p_i}$ to vary for different i, we can still make the approximation that if $\overline{Le} \approx 1$, then

$$\sum_i \overline{c}_{p_i} \nabla Y_i - \overline{Le} \nabla \overline{c}_p \approx - \sum_i \left(Y_i \frac{\partial \overline{c}_{p_i}}{\partial T} \nabla T \right)$$

so that

$$\vec{\nabla} \cdot \left\{ \rho \mathcal{D}_{ij} T_1 \left[\sum_i (\overline{c}_{p_i} \nabla Y_i) - \overline{Le} \nabla \overline{c}_p \right] \right\} \approx - \vec{\nabla} \cdot \left[\rho \mathcal{D}_{ij} T_1 \sum_i \left(Y_i \frac{\partial \overline{c}_{p_i}}{\partial T} \nabla T \right) \right] \tag{6.41}$$

The third and fourth assumptions imply that

$$\mu \Phi \approx 0 \tag{6.42}$$

and

$$\dot{Q}_V \approx 0 \tag{6.43}$$

The fifth approximation that terms in which the diffusion velocity appears as order two or higher are neglected implies that

$$-\frac{1}{2}\rho\frac{D}{Dt}\left(\sum_i Y_i\vec{V}_i\cdot\vec{V}_i\right)-\vec{\nabla}\cdot\left\{\rho\sum_i[Y_i\vec{V}_i(\vec{v}\cdot\vec{V}_i)+\frac{1}{2}Y_i\vec{V}_i(\vec{V}_i\cdot\vec{V}_i)]\right\}\approx 0 \qquad (6.44)$$

The final approximation that the molecular weights of all species are equal results in

$$\begin{aligned}\vec{\nabla}\cdot\sum_i P_i\vec{V}_i &= \vec{\nabla}\cdot\rho\mathcal{R}T\sum_i\left(\frac{Y_i\vec{V}_i}{\hat{M}_i}\right)\\ &\approx \nabla\cdot\frac{\rho\mathcal{R}T}{\hat{M}_1}\sum_i Y_i\vec{V}_i = 0\end{aligned} \qquad (6.45)$$

since

$$\sum_i Y_i\vec{V}_i = 0$$

Using a prime (′) to denote a dimensional quantity, equations (6.20), (6.38), and (6.41)-(6.45) give the following nondimensional approximate source term for the energy equation for $\overline{Le} = 1$:

$$\begin{aligned}S_\phi = \frac{t_*}{\rho_* c_{p_*} T_*}S'_\phi \approx \frac{t_*}{\rho_* c_{p_*} T_*}\Bigg\{&\frac{\partial P'}{\partial t'}+Q'_{\mathrm{ch}}\\ &-\vec{\nabla}'\cdot\left[\rho'\mathcal{D}'_{ij}T'_1\sum_i\left(Y'_i\frac{\partial\overline{c}'_{p_i}}{\partial T}\nabla T'\right)\right]\Bigg\}\end{aligned} \qquad (6.46)$$

Using

$$Eu_* \equiv \frac{(\Delta P)_*}{\rho_* U_*^2}$$

and

$$Ec_* \equiv \frac{U_*^2}{c_{p_*}T_*} \qquad (6.47)$$

we can write

$$\frac{t_*}{\rho_* c_{p_*} T_*}\frac{\partial P'}{\partial t'} = Eu_* Ec_*\frac{\partial P}{\partial t}$$

Also, since

$$Y_* = 1, \quad \rho\mathcal{D}_{ij} = \frac{\rho'\mathcal{D}'_{ij}}{\mu_*}, \quad \text{and } t_* = \frac{L_*}{U_*}$$

we can write

$$\begin{aligned}
&\frac{t_*}{\rho_* c_{p_*} T_*}\vec{\nabla}'\cdot\left[\rho'\mathcal{D}'_{ij}T'_1\sum_i\left(Y'_i\frac{\partial\overline{c}'_{p_i}}{\partial T}\nabla T'\right)\right] = \\
&= \frac{\mu_*}{\rho_* U_* L_*}\vec{\nabla}\cdot\left[\rho\mathcal{D}_{ij}T_1\sum_i\left(Y_i\frac{\partial\overline{c}_{p_i}}{\partial T}\nabla T\right)\right] \\
&= \frac{1}{Re_*}\vec{\nabla}\cdot\left[\rho\mathcal{D}_{ij}T_1\sum_i\left(Y_i\frac{\partial\overline{c}_{p_i}}{\partial T}\nabla T\right)\right]
\end{aligned}$$

Therefore the final nondimensional source term [equation (6.46)] may be written as

$$\begin{aligned}
S_\phi \approx\ & Eu_* Ec_* \frac{\partial P}{\partial t} + \frac{t_*}{\rho_* c_{p_*} T_*} Q'_{\text{ch}} \\
& -\frac{1}{Re_*}\vec{\nabla}\cdot\left[\rho\mathcal{D}_{ij}T_1\sum_i\left(Y_i\frac{\partial\overline{c}_{p_i}}{\partial T}\nabla T\right)\right]
\end{aligned} \tag{6.48}$$

In the current computational model, we assume that $\overline{c}_{p_i} \approx$ constant, $\overline{Le} = 1$, and no chemical reactions so that

$$S_\phi \approx Eu_* Ec_* \frac{\partial P}{\partial t} \tag{6.49}$$

However, in the future when chemical reactions are included in the code, equation (6.48) will be used as the source term of the energy equation where

$$Q_{\text{ch}} \equiv -\sum_i \left(h_i^\circ r_i'''\right)'$$

Chapter 7

Preliminary Results

The numerical model has been tested by comparing results with a bench mark solution for one-phase, steady-state, buoyancy-driven flow in a square cavity [17]. The thermal boundary conditions for this problem are differentially heated vertical side walls and insulated top and bottom walls. Results obtained using the SIMPLEC algorithm agree very well with the literature. For example, for the case of Ra = 10^6 (Ra is the Rayleigh number), De Vahl Davis reports $|-\psi|_{\max} = 16.772$ at $x = 0.154$ and $y = 0.545$. For this same case I find $|-\psi|_{\max} = 17.3$ at $x = 0.154$ and $y = 0.540$, which differs from the aforementioned bench mark solution by approximately 3%. However, since this relatively simple test problem does not involve the effects of radiation, wall thermal inertia, or variable properties, the comparison cannot be considered a complete verification of the computational code.

In order to obtain a more thorough verification of the code, it is necessary to compare numerical and experimental results. This involves an added complexity in that the computer code must accurately model the actual experiment, or vice-versa. If simplifications introduced in the model cannot be reproduced experimentally to within a prescribed accuracy, then the computational code must be modified to duplicate the experimental results. As will be shown in this chapter, preliminary results

of a single-phase simulation agree fairly well with the corresponding experimental results; however some evidence exists which suggests that the current computational model should be modified to allow for emissivities less than 1.0. The results also indicate that the actual radial temperature profile of the axisymmetric heater should be used instead of modelling the heater as having a constant radial temperature.

The following four single-phase, normal-gravity computer simulations have been performed to date for a cylindrical, plexiglass test cell (10 cm Dia. x 10 cm Height):

1. 682 K, 1.2 cm heater with 0.4 cm thick top and side walls, and 1.2 cm thick bottom wall.
2. 682 K, 1.2 cm heater with 0.4 cm thick top and side walls, and 1.2 cm thick bottom wall; radiation effect not included.
3. 794 K, 1.0 cm heater with 0.635 cm thick top and side walls, and 1.905 cm thick bottom wall.
4. 1.0 cm heater with 0.635 cm thick top and side walls, and 1.905 cm thick bottom wall. Parabolic heater temperature profile (from actual measurements) used with 772 K centerline temperature (actual radial temperature profile given on Figure 7.1).

Unless otherwise specified above (e.g., simulation #2), all runs included the effects of radiation (assuming all heater and wall surface emissivities equal to 1.0), variable properties, and wall thermal inertia. A two-dimensional explicit scheme was used for the thermal conduction in the walls. The right side of the heater is assumed to be insulated from the remainder of the top wall. The outside of the bottom wall is assumed to be held at constant temperature (300 K). The outside of the top and side

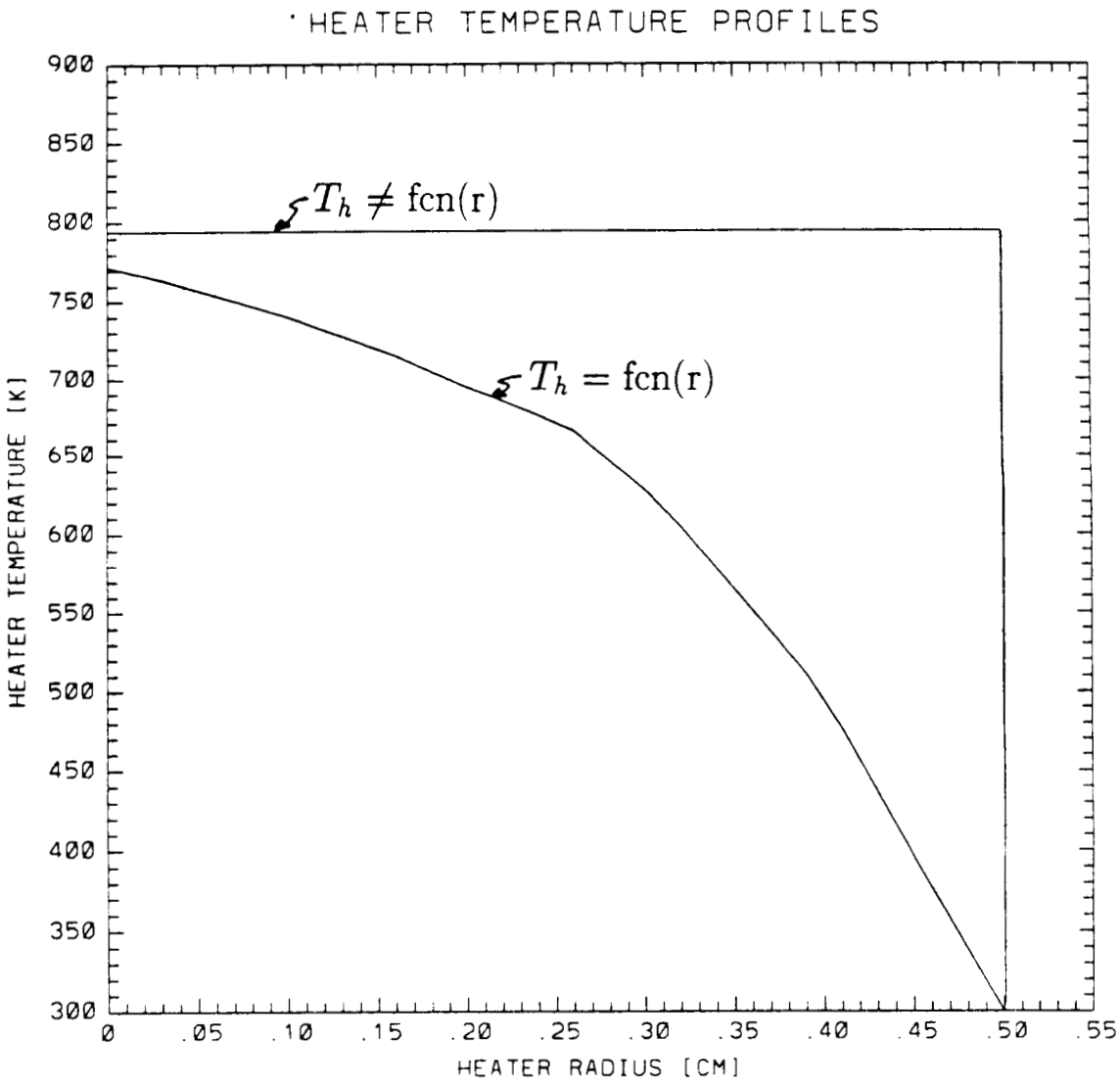

Figure 7.1: Heater temperature profiles for simulations #3 and #4.

walls exchange heat to the ambient environment via Newton Cooling (this heat loss is negligible compared to the heat flux on the inner walls for the relatively short-time simulations conducted). The results of these simulations and the experiments which they model are presented below. Note that the left side of the computational domain corresponds to the axis of symmetry of the container.

As shown on Figure 7.2, one toroidal cell is initially formed in the container for simulation #1. After approximately 4 seconds a second cell begins to form near the side wall at near mid-height of the container. This cell eventually splits the flow pattern into three separate toroidal-shaped vortices. Figure 7.2 shows a velocity vector representation of the flow fields, with all magnitudes of the vectors equal in order to emphasize the qualitative pattern of the flow. In actuality the velocities just below the heater are on the order of 3 cm/s while the velocities in the middle and lower vortices are on the order of 0.2 cm/s and 0.05 cm/s, respectively. Therefore, in order to get a better quantitative and qualitative picture of the flow field, it is helpful to plot contours of the nondimensional stream function, defined by

$$\psi = -\int_0^r \rho r v dr, \qquad \psi = r\int_0^y \rho u dy \tag{7.1}$$

Plots of this type indicate that the maximum value of the stream function in the middle vortex increases slightly until $t = 15$ seconds, decreases between $t = 15$ seconds and $t = 50$ seconds, and then increases steadily for times greater than 50 seconds. This is shown on Figures 7.3 and 7.4. It appears that for $t < 50$ seconds, the middle vortex is partially entrained by the upper and lower vortices. However for $t > 50$ seconds, the middle vortex strengthens and the amount of entrainment decreases. Notice that at $t = 10$ seconds the ratio of the local maxima of the stream function for the three vortices (upper:middle:lower) is 126:29:5 (approximately 25:6:1), while at

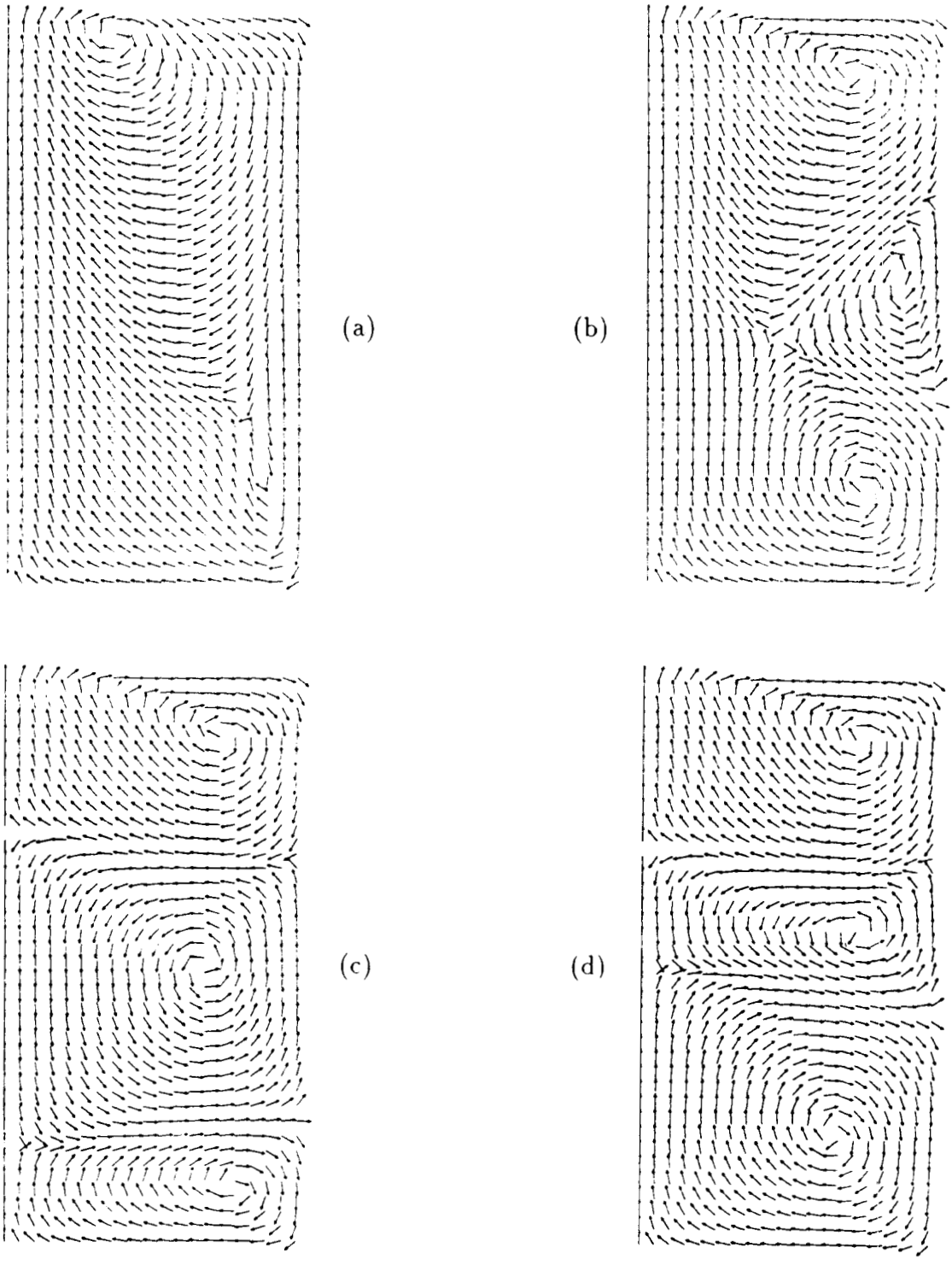

Figure 7.2: Flow patterns from simulation #1 for (a) $t = 0.5$, (b) $t = 4$, (c) $t = 15$, and (d) $t = 50$ seconds. All velocity vectors shown are made equal length to emphasize the qualitative pattern of the flow.

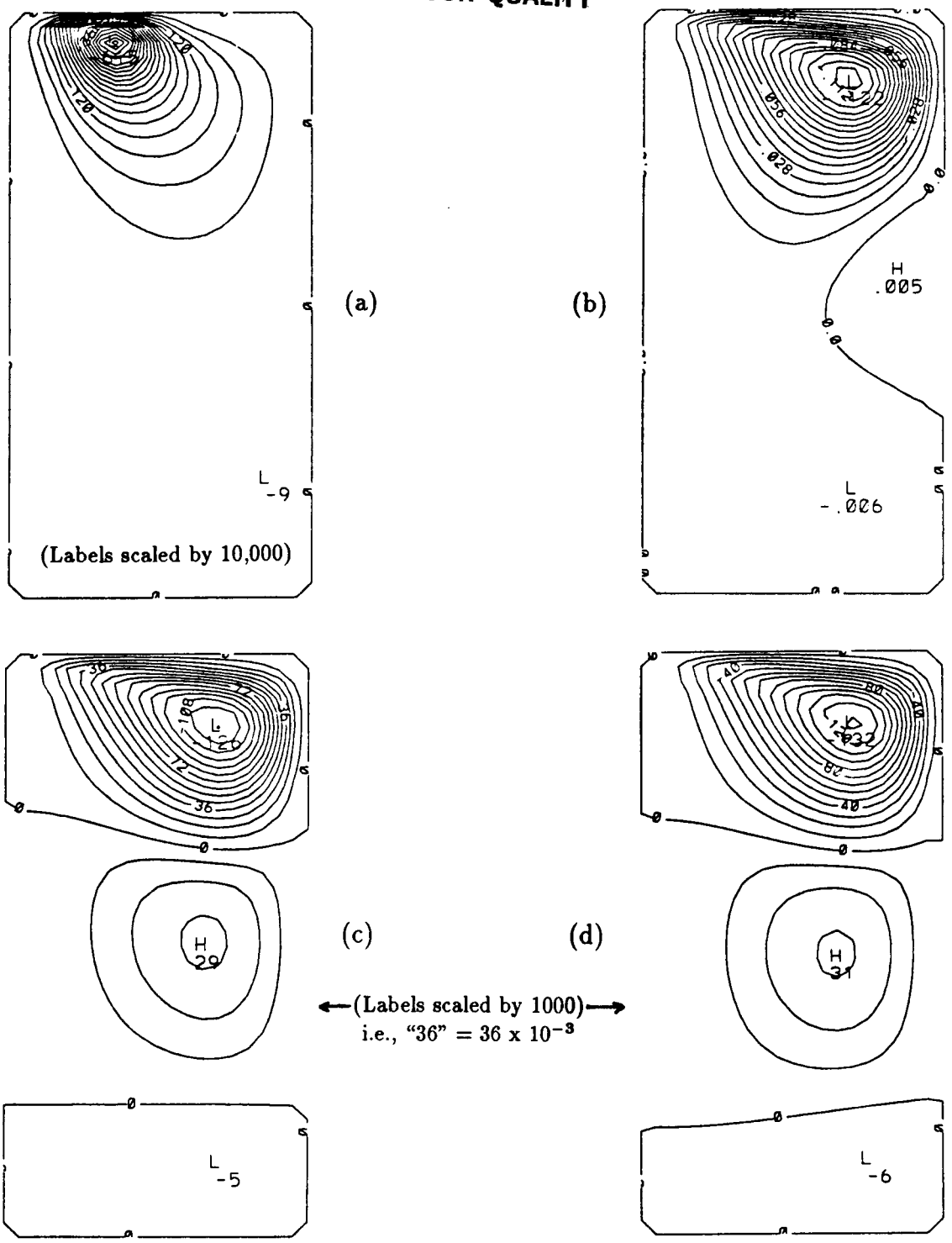

Figure 7.3: Nondimensional stream function (ψ) contours from simulation #1 for (a) $t = 0.5$, (b) $t = 4$, (c) $t = 10$, and (d) $t = 15$ seconds. Note local maximum of ψ for middle vortex increases from $t = 10$ to $t = 15$ seconds; $(\rho UL)_* = 5.915 \times 10^{-4}$ kg/(m·s).

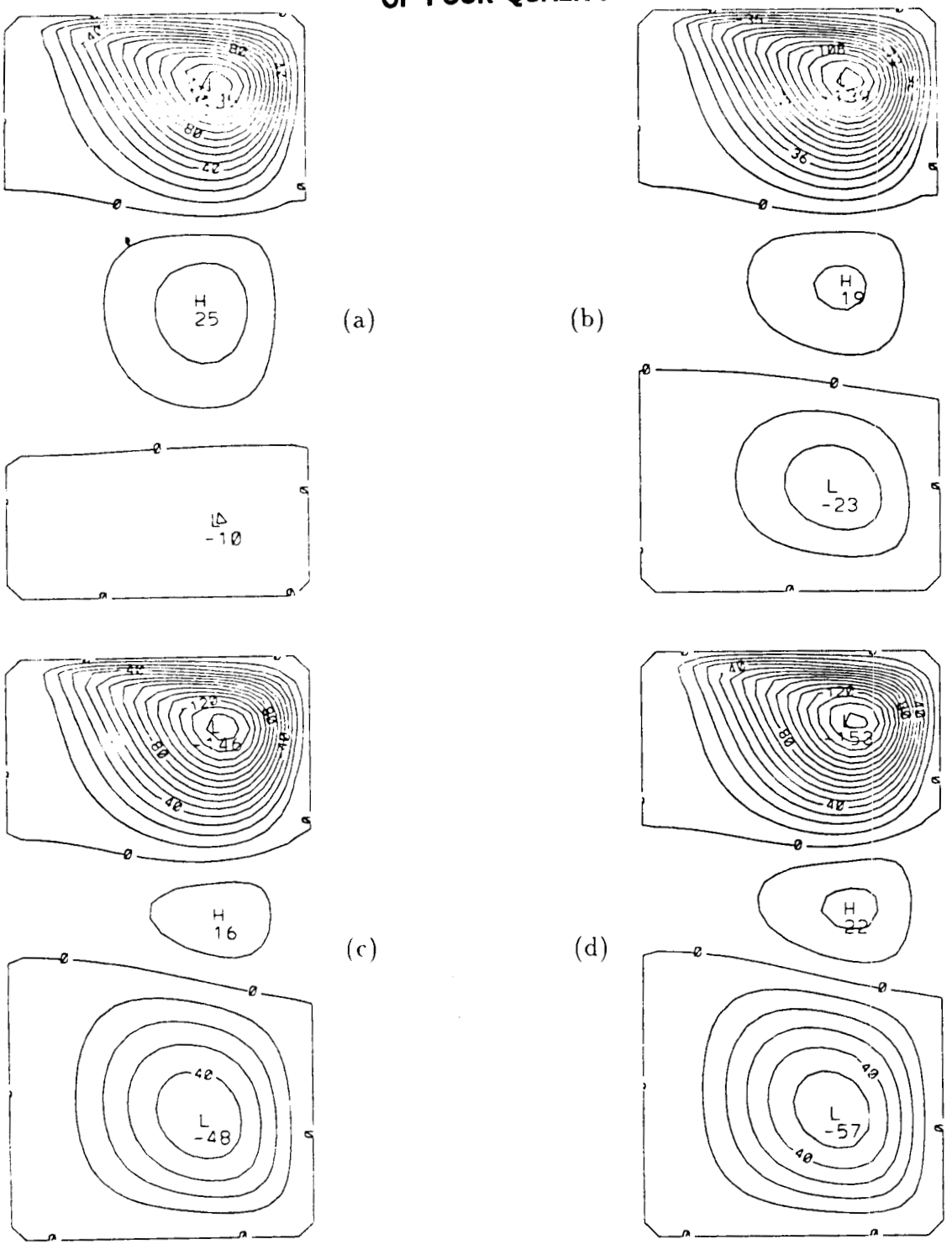

Figure 7.4: Nondimensional stream function (ψ) contours from simulation #1 for (a) $t = 20$, (b) $t = 30$, (c) $t = 50$, and (d) $t = 80$ seconds. For $t < 50$ seconds, the middle vortex is partially entrained by the upper and lower vortices. However middle vortex stregthens for $t > 50$ seconds. Note: ψ values scaled by 1000.

$t = 50$ seconds this ratio is 146:16:48 (approximately 9:1:3), and at $t = 200$ seconds this ratio is 176:39:53.

As shown on Figures 7.5 and 7.6, only one large toroidal cell is distinguishable during the first approximately 50 seconds in experiments using the 682 K heater (note that this is the centerline temperature of the heater; the exact radial temperature profile of the heater has not been measured). At later times, a second vortex appears in the lower half of the container. This vortex is much weaker than the upper cell, and in some experiments the upper and lower vortices were formed inside one large, "figure-8"-shaped cell. The general trend of the experiments performed to date with the 1.0 cm and 1.2 cm heaters and the 10 cm (diameter and height) container has been that at relatively low heater temperatures (below approximately 650 K) only one large toroidal cell forms in the container. Between 650 K and 750 K the single cell starts to form a "figure-8" pattern, and for heater temperatures between approximately 750 K and 820 K two toroidal cells separated by a saddle point appear inside a large "figure-8"-shaped cell. For the most part experimental results have shown good reproducibility. However, some experiments indicate that soot formation on the inner walls of the container (due to the smoke particles used for flow visualization) may appreciably affect the radiation heat transfer. We would expect that as the Grashof number increases (e.g., by increasing the heater temperature) or as the radiation heat transfer increases for a given Grashof number, the number of recirculation cells should increase. Over the temperature range investigated the number of recirculation cells found experimentally seemed to vary from one cell to two cells. In most tests increasing the heater temperature decreased the height of the upper vortex; however in some tests the height of this cell increased (extended much lower toward the bottom of the container) compared to runs made at a lower heater temperature. One parameter

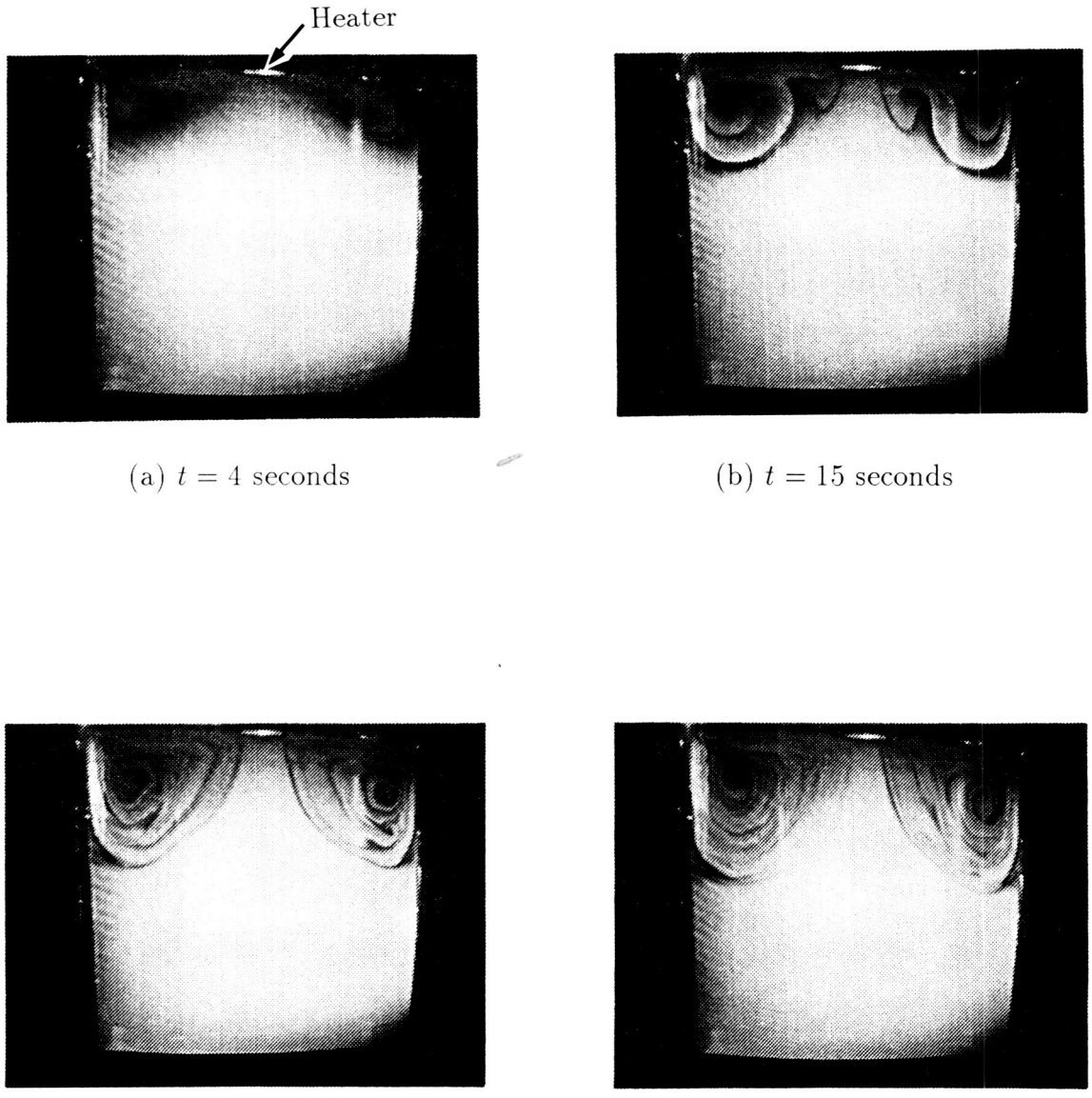

(a) $t = 4$ seconds

(b) $t = 15$ seconds

(c) $t = 30$ seconds

(d) $t = 50$ seconds

Figure 7.5: Flow patterns obtained in experiments using 682 K heater for (a) $t = 4$, (b) $t = 15$, (c) $t = 30$, and (d) $t = 50$ seconds. Only one toroidal-shaped vortex is distinguishable. Smoke tracers and low-power laser light sheet were used for flow visualization.

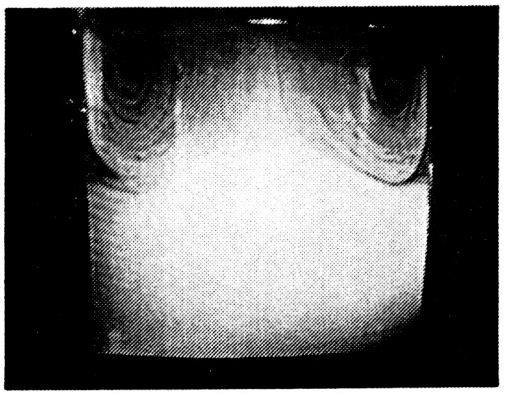

(a) $t = 60$ seconds

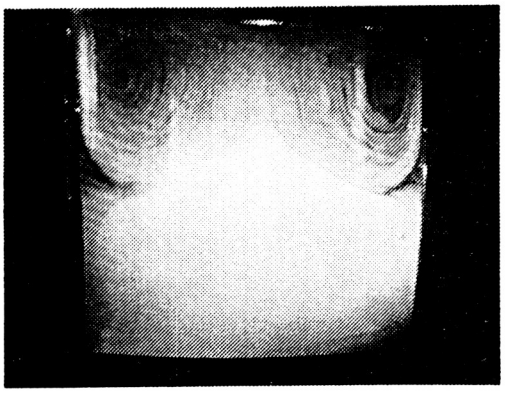

(b) $t = 80$ seconds

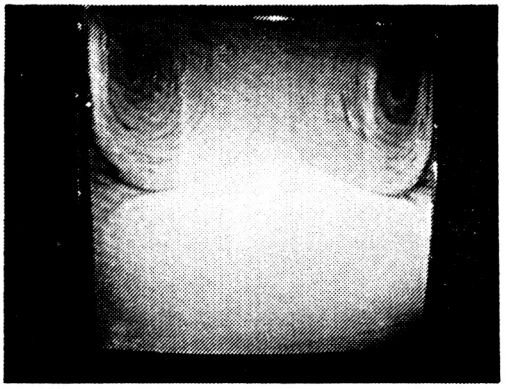

(c) $t = 100$ seconds

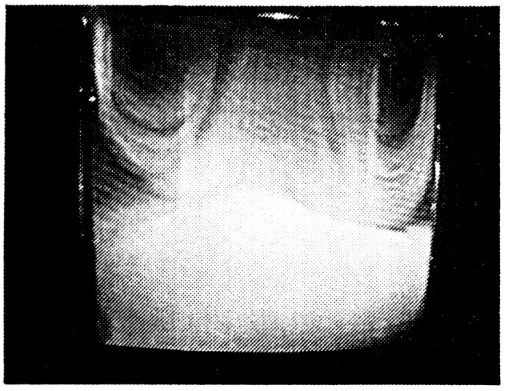

(d) $t = 200$ seconds

Figure 7.6: Flow patterns obtained in experiments using 682 K heater for (a) $t = 60$, (b) $t = 80$, (c) $t = 100$, and (d) $t = 200$ seconds. Outline of relatively weak lower vortex is faintly distinguishable.

that may significantly affect the flow pattern may be the emissivity of the heater and wall surfaces. These values may change over the course of the experiments from an "ultrasonically cleaned" value to a soot-covered value due to the use of smoke particles for flow visualization.

In order to get a lower bound on the effect of radiation on the flow pattern, the above simulation was run without including the effect of radiation (simulation #2). The result, as shown on Figure 7.7, is that one large toroidal cell forms in the container, the strength of which changes very little from $t = 5$ seconds to $t = 100$ seconds. A comparison of the nondimensional stream function contours with and without radiation for $t = 100$ seconds appears on Figure 7.8. The maximum value of the stream function for the single vortex without radiation is only 8% less than the local maximum value of the upper vortex for the case including radiation. However, the flow pattern is qualitatively very different since only only large cell is formed instead of three. Thus the qualitative flow pattern is a strong function of the radiative heat transfer.

In the first simulation described above, three vortices formed with the middle vortex being the weakest and smallest of the three. However, in the experiments conducted with the 682 K heater at most only two vortices formed inside a large "figure-8"-shaped cell. Although the radial temperature profile of this heater was not measured (due to equipment failure), another experiment was run using a slightly hotter heater with a known radial temperature distribution. Two computer simulations were run to investigate the differences in flow pattern between using a constant heater temperature profile and using the actual radial temperature distribution. Figure 7.1 shows the heater temperature profiles used for these two simulations. The 794 K heater temperature corresponds to the thermocouple reading of the centerline

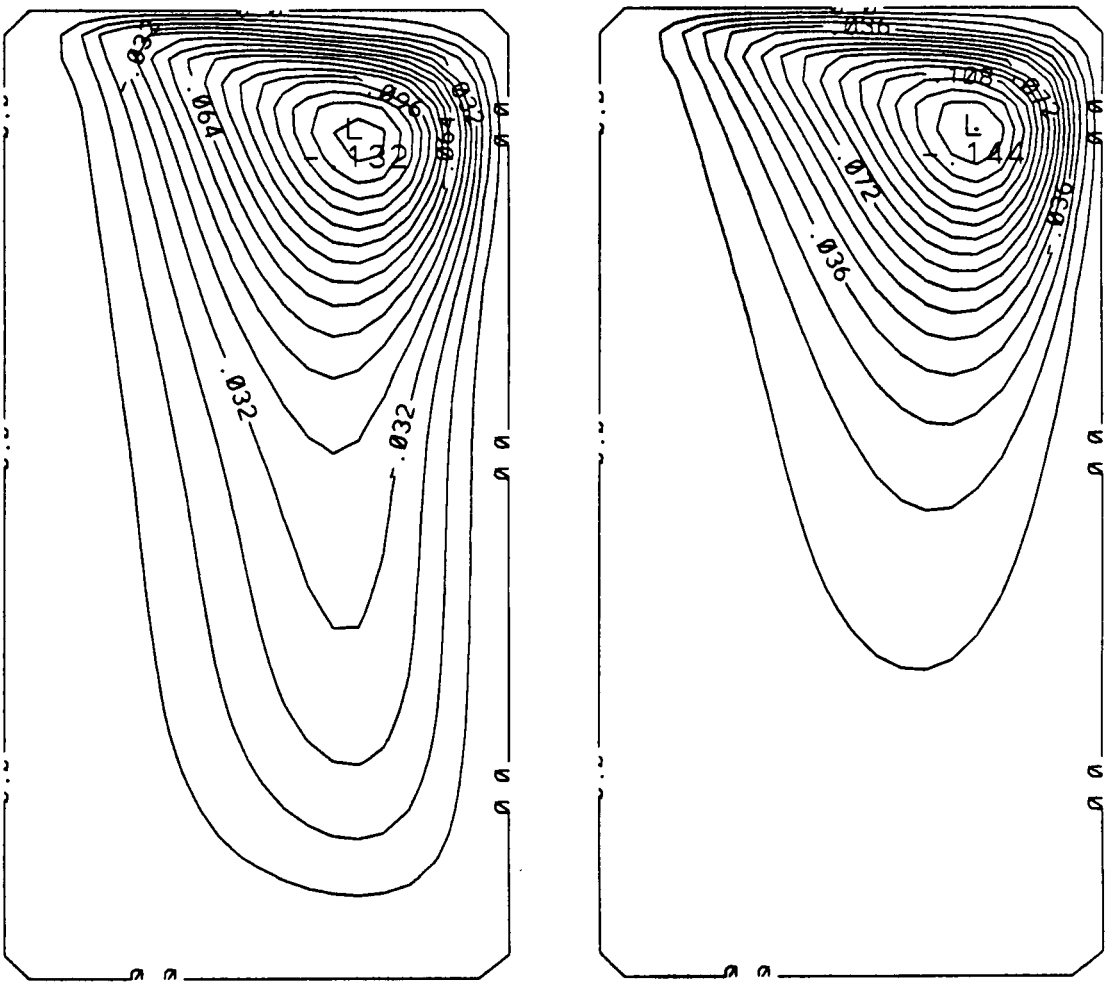

(a) $t = 5$ seconds

(b) $t = 100$ seconds

Figure 7.7: Nondimensional stream function (ψ) contours from simulation #2 (radiation not included) for (a) $t = 5$ seconds and (b) $t = 100$ seconds. One large toroidal cell forms in the container, the strength of which changes very little throughout the simulation.

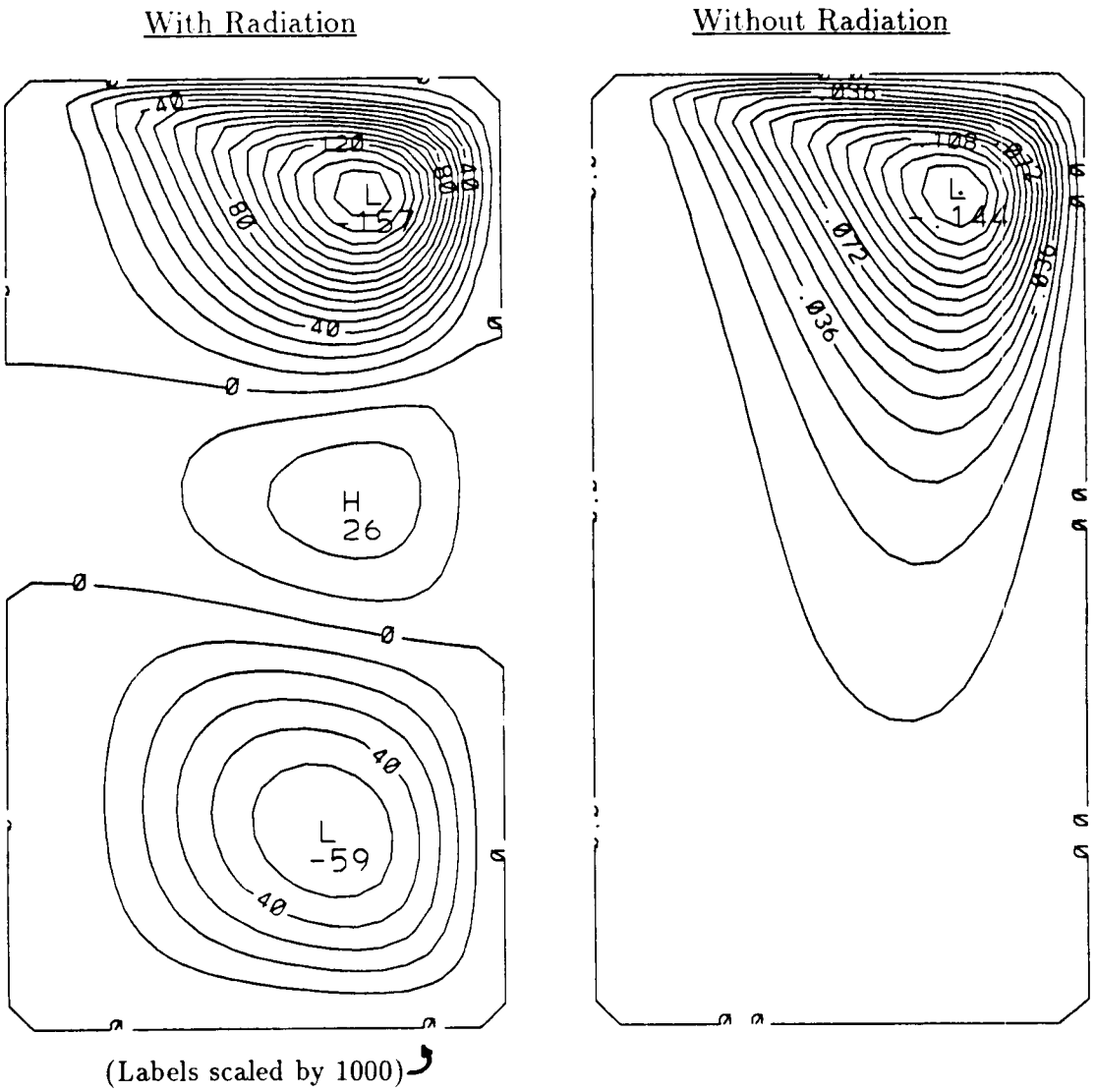

$t = 100$ seconds

Figure 7.8: Comparison of the nondimensional stream function (ψ) contours with and without radiation (simulations #1 and #2) for $t = 100$ seconds.

temperature of the heater while it was in place during the experiment. An optical radiometer was then used to measure the radial temperature profile of the heater after the heater and water-cooled jacket were removed from the top wall of the test cell. Using this measurement technique, the centerline temperature of the heater was found to be 772 K.

Using the constant-temperature heater profile, the flow pattern developed in a qualitatively identical manner as the previously reported simulation with the 682 K 1.0 cm heater. However, when the radially-varying heater temperature profile was used, a "figure-8"-shaped flow pattern resulted with a saddle point separating two clockwise rotating vortices. Figure 7.9 shows a comparison of the two flow fields after $t = 60$ seconds in terms of the nondimensional stream function (note that negative values of the stream function correspond to clockwise rotation). It was found that, qualitatively, the flow patterns did not change significantly after $t = 20$ seconds. Although no photographs were taken of the experiment with this heater temperature, hand-drawn sketches of the flow pattern and reports by the experimenter confirm that a "figure-8"-shaped flow pattern was indeed formed, and that this configuration was stable over the (several minute) duration of the test. Therefore based on the experimental results and the results of the two related computer simulations, one may conclude that significant differences in the predicted flow pattern result depending on the assumption of the heater temperature profile for a given centerline temperature. In order to obtain an accurate comparison of the experimental results, the actual radial heater temperature distribution should be obtained.

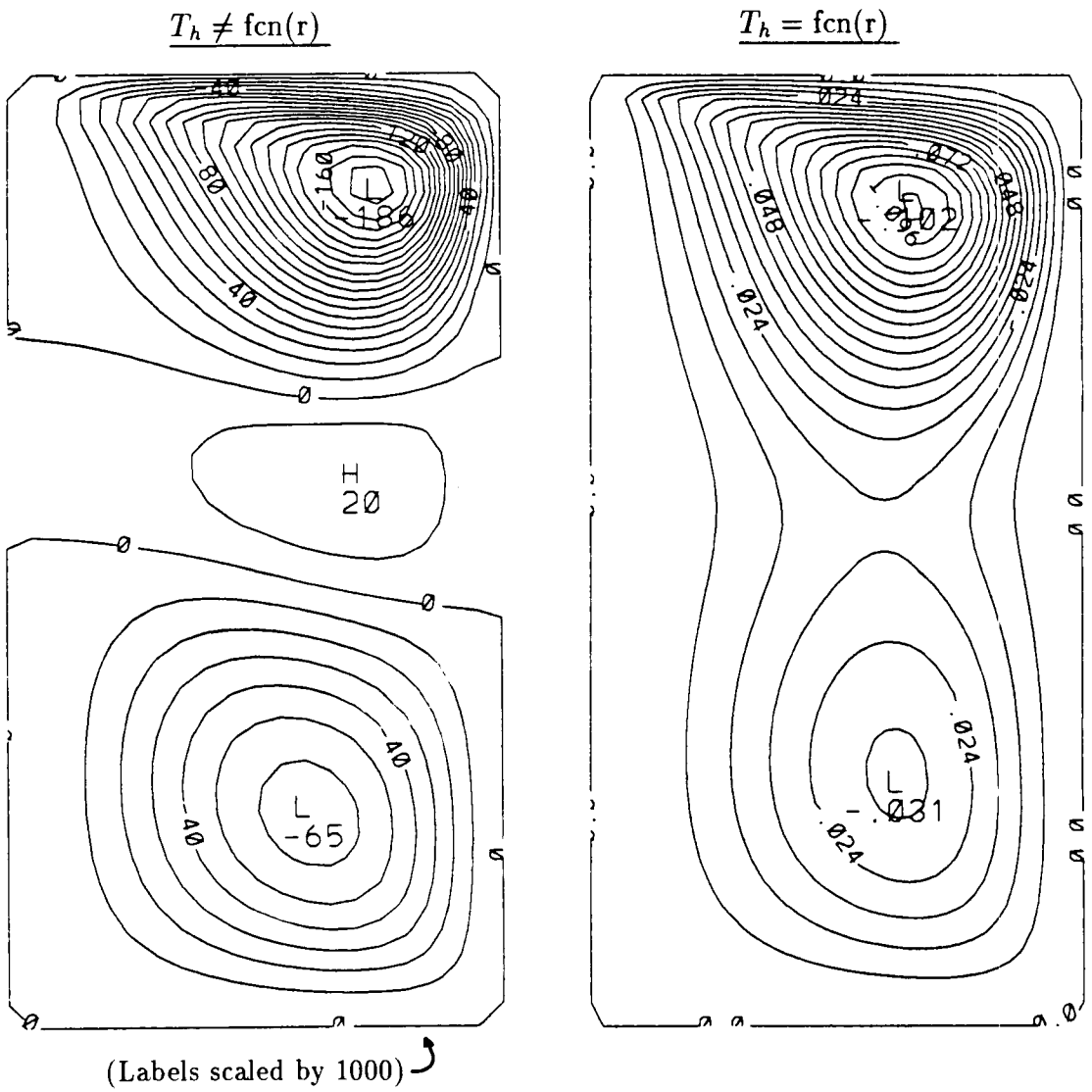

$t = 60$ seconds

Figure 7.9: Comparison of the nondimensional stream function (ψ) contours at $t = 60$ seconds for constant versus radially-varying heater temperature profiles (simulations #3 and #4).

Chapter 8

Conclusions

The principal objective of the experimental effort is to validate a computational model which simulates transient heat transfer and fluid flow in an enclosure containing a single-phase or two-layer gas-and-liquid system heated unevenly from above. Toward this goal, both minimum and desired requirement levels were defined to guide the design and conduct of the experiments. The rationale presented for the minimum requirements was typically based on the need for verifying the qualitative results (e.g., flow patterns) of the computer code, whereas the desired requirements were established in order to verify the quantitative results (e.g., magnitudes of velocity and temperature) of the code. Specifications were provided for experiments in three separate settings: (a) a normal gravity laboratory, (b) the NASA-LeRC drop towers, and (c) a space-based laboratory. Most of the experiments will be conducted under normal gravity conditions. However, in order to study the quasi-steady state behavior of the preignition problem and to validate the computer program over the required range of the Grashof number and the inertia of the flow, eight tests have been defined for a space-based facility. The 2.2 and 5.18 second NASA-LeRC drop towers will be used to obtain transient low-gravity data and to support the space flight experimental effort. For example, the required design for maintaining a flat liquid surface in microgravity may be developed in the drop tower tests. As discussed

in Chapter 3 and Appendix A, most of the parametric studies will be conducted in the ground-based tests to minimize the cost of the spaced-based experimental effort.

Preliminary results of single-phase normal gravity experiments and simulations show fairly good agreement. However some evidence exists which suggests that the current computational model should be modified to allow for heater and wall surface emissivities less than 1.0. Results also indicate that the radial temperature profile of the heater, not just the centerline temperature, must be measured in order to accurately simulate the experiment.

Appendix A

Description of Preliminary Hardware Concepts

The ground-based and space-based experiments consist of the following hardware: test cell, fluids (liquid and gas), heater, flow visualization system, temperature measurement system, liquid-gas interface control system, and a data acquisition and control system. Hardware concepts for these tests are described in this appendix.

Test Cell. Previous experimental efforts at NASA-LeRC have utilized plexiglass test cells of both planar and cylindrical geometries. In these tests a rectangular tank surrounding the test cell was partially filled with an index matching fluid in order to minimize distortion due to refraction in the liquid phase. The 1-g tests used 10 cm inner diameter cylindrical cells of height 10 cm with the wall being 1/8–1/4" thick. The rectangular test cell geometry has the advantage that it simplifies flow visualization and data reduction. However, the cylindrical geometry has the important advantage that an axisymmetric flow is easily achieved within a small packaging volume. With the planar geometry, if a rectangular heater strip spans the width of the top of the test cell, then the width of the container must be relatively large to reduce edge effects.

The container must be made of an optically transparent material to allow for measurement of the velocity field. Testing in 1-g has shown that Freon 113 (the liquid selected for ground-based tests) crazes plexiglass. Hence if Freon 113 (also known as R113) is to be used for space-based experimentation, a glass or sapphire container should be used. Glass has the disadvantage of being fragile while sapphire has the disadvantage of being expensive. Since the preignition tests will not involve flames, plexiglass, glass, and sapphire all meet the temperature stability requirements.

Packaging constraints severely limit the size of the test cell for microgravity experimentation. The cylindrical capsule of the 5.18 second drop tower limits the experiment volume to 1 m diameter and 1.5 m height. The inside dimensions of a Shuttle "special can" are approximately 31" (0.79 m) diameter and 57" (1.45 m) height. The minimum dimensions of the test cell are governed primarily by flow visualization requirements. Tests have also indicated that in microgravity experiments the smaller the test cell, the easier it is to achieve a quiescent, "flat" interface. Specifically, the required reduced gravity time to reach an equilibrium shape goes as $d^{1.5}$ where d is the diameter of the test cell. The selected container dimensions will be determined after further study of the component packaging and after further assessment of the velocity and temperature measurement systems.

No special provisions are required for maintaining insulated or constant wall temperature boundary conditions, as the computational code accounts for general two-dimensional conduction and thermal inertia in the wall. Computer simulations have indicated that the temperature of the liquid at the bottom of the container does not change more than $0.01^{\circ}C$ during the first hour of an experiment. This result was obtained for the case of a 10 cm height of liquid R113 with an 800 K heater, run for one hour in a simulated 1-g environment. The outer side walls, however, heat up

to almost 340 K when a 1/4" thick plexiglass test cell is used in a 300 K ambient environment for the above simulation. Heat loss due to natural convection to the environment is therefore appreciable in quasi-steady state 1-g tests. Requirements for ambient temperature have already been given in this document.

Fluids. To promote stable, measurable fluid motion and to simplify analysis, the selected fluid should have the following characteristics: large $d\sigma/dT$, small viscosity, high decomposition temperature, purity, insensitivity to contamination, and well known liquid and vapor properties. It would also be desirable that the liquid have a near 90^o contact angle with the test cell material, although this is not a requirement since special provisions will be made to "pin" the interface (see "Liquid-Gas Interface Control System" section). Of course, the selected fluid must also satisfy the usual array of health and safety requirements. For space-based experimentation, nonflammability is critical. In other space experiment work, silicon oil is proposed for use [13]. This fluid is unsuitable however for the present effort as it is a complex mixture of polymers for which little or no vapor property information is available.

An alternative is the halogenated hydrocarbons (tradename: Freon), hereafter referred to as refrigerants. Properties for these fluids are well documented with one attractive candidate, R113, being exceptionally well documented [18] and well modelled [19]. This fluid also has a very high rating for being nonflammable and nontoxic [18]. As mentioned previously, ground tests with R113 indicated that this fluid crazes the surface of a plexiglass container over a few drop tower tests. This is not a problem for ground-based experimentation, since test cells may be readily replaced between tests. However, volume limitations on the Shuttle or Space Station make spare test cells an impractical option for space-based experimentation. For these tests either

R113 will be used with a glass or sapphire container, or else alternative fluids will be selected for use with a plexiglass test cell.

Air will be used as the gas phase in all the experiments. Although some difficulties arise for flow visualization with a two-phase system, using air for the gas phase is most practical on a scientific basis.

Filling the test cell with liquid to a specified level is simple in 1-g experiments. However, additional hardware is required for the reduced gravity experiments. For drop tower tests the ability to fill the test cell to a specified liquid level via remote and reproducible means is required. At the present time a gravity-feed system has been designed but not fabricated or tested. For space-based experiments, a different system is required. One concept for such a system may operate as follows: a bladder tank is initially filled with the test liquid. A flow meter and controller monitor, measure, and control the flow and flow rate. A fine mesh screen is installed near the bottom of the test cell. The flow rate of the liquid is sufficiently slow (on order of TBD cc/sec) so that the surface tension of the liquid anchors the liquid to the screen and walls of the test cell, thus preventing the formation of liquid droplets which could wander off into the vapor portion of the container. Such a system has been designed and tested for a surface-tension-driven space-based experiment [20]. The liquid-gas interface control system prevents the liquid from migrating up the walls past the desired fill level.

Heater. The experiments use a constant-temperature heater operated at either 350 K, 575 K, or 800 K. This temperature range was selected to provide a variation of one order of magnintude in $\beta g L \Delta T$ when the liquid is initially at 300 K. Fluctuations in the heater temperature should not exceed $\pm 1\%$ over a period of less than 1 second

(the data sampling period). A constant-temperature heat source is used by the computational model instead of a constant-heat-flux source because the former is more representative of actual flames. Normal gravity tests at NASA-LeRC have used a heater of shielded nichrome wire brazed to a stainless steel plate. Ceramic cement insulation reduces heat loss to the environment, and a temperature-controlled water jacket is used to both prevent the test cell material from reaching a melting temperature and to concentrate the heating from above. Cylindrical heaters of diameters 1 cm, 2.5 cm, and 5 cm have been constructed for use in cylindrical test cells. However for the rectangular test cell which may also be used in ground-based experiments, a rectangular heater strip is required. Such a rectangular heater would be surrounded by a water-cooled jacket for the purposes mentioned above. The dimensions of the heater and/or the emissivity of the heater will be varied in the experiments in order to provide for a variation of the radiation heat transfer in the experiments.

Flow Visualization System. Requirements for the flow visualization system differ slightly between the three experiment settings: 1-g, drop tower, and space-based. Certainly the goal of the system is the same for each case: to track the flow of the gas and liquid phases in order to obtain velocity measurements over time throughout the test cell. As a minimum requirement visualization of the general flow patterns in each phase is needed. However, different constraints are involved for the three experiment settings. For the space-based experiment, packaging and automation are the key concerns. The available volume of a Shuttle "special can" is highly restrictive, and operator (crew) time is restricted. The flow visualization system for a Shuttle experiment must survive launch and be reliable, as crewmembers should not have to make any adjustments on-orbit. Drop tower experiments are also appreciably volume-limited. The drop tower imposes two additional requirements to the design

of the flow visualization system: the system must survive approximately a 30-g shock at the bottom of the drop, and the system must function effectively after at least a 3 minute 1-g "hands-off" hanging time prior to the drop. The 1-g experiments are the least restrictive of the three. They have basically no volume constraint, require no automation, and undergo no shock or change of gravitational acceleration.

The flow visualization systems selected for the three types of experiments each consist of four basic components: tracer particles, a method for injecting and stirring the tracer particles and droplets, a light sheet for illuminating one plane of the flow, and a camera or cameras for recording the flow visualization. A grid should be used on the test cell to help quantify the visualization measurements. The design of the flow visualization system components is discussed below.

1. Tracer Particles

   Feasibility tests were performed to determine if tracer particles or droplets could be employed for flow visualization. Of particular difficulty was the tracer measurement of the gas phase. The common technique of smoke tracers was investigated and discarded when it was observed that the smoke contaminated the liquid R113 surface. This contamination effectively eliminated the surface-tension-driven convection because the surface-tension variation due to temperature variation was counter-balanced by that due to the concentration variation. Therefore smoke tracers will only be used in single-phase tests and two-phase tests designed to obtain results without surface-tension-driven convection. In place of smoke tracers, small R113 droplets were injected into the gas phase near the stagnation point of the heater surface. These droplets, being the same material as the bulk liquid, did not contaminate the liquid surface. They were

also sufficiently small, on the order of 1–5 micron, so that they allowed observation of flow patterns. Figures A.1 and A.2 show photographs taken of video tape frames from a 1-g experiment. The toroidal-shaped circulating cell in the top half of the gas phase is driven by buoyancy. The "notch" in this cell was seen repeatedly in several tests, although it was unpredicted with the current simulation. However, later experimentation with the orientation of the light sheet indicated that the power of the laser light caused this "notch" in the flow field.

In anticipation of velocity field quantification, an error analysis was performed to determine how well the tracer droplets could track the vapor streamlines. The largest sources of error were found to be gravitational settling (for 1-g tests), on the order of 2 mm/sec for the largest droplets (5 micron), and thermocapillary-driven motion very near the heater surface.

The tracer particles selected for flow visualization in the liquid phase are 1 micron aluminum oxide (Al_2O_3) particles with about 0.5 mg/100 ml concentration level. This technique has been used successfully in the 1-g experiments which were conducted [21]. In order to minimize distortion due to refraction, a rectangular chamber surrounding the test cell was filled with an index matching fluid (liquid phase only). Due to diffraction, information on velocities within 1 mm of the surface is lost. In future ground-based tests, surface velocities will be obtained by sprinkling aluminum oxide particles on the surface with observation from below. Measurement of liquid surface velocities for the space-based experiment is desirable but not required.

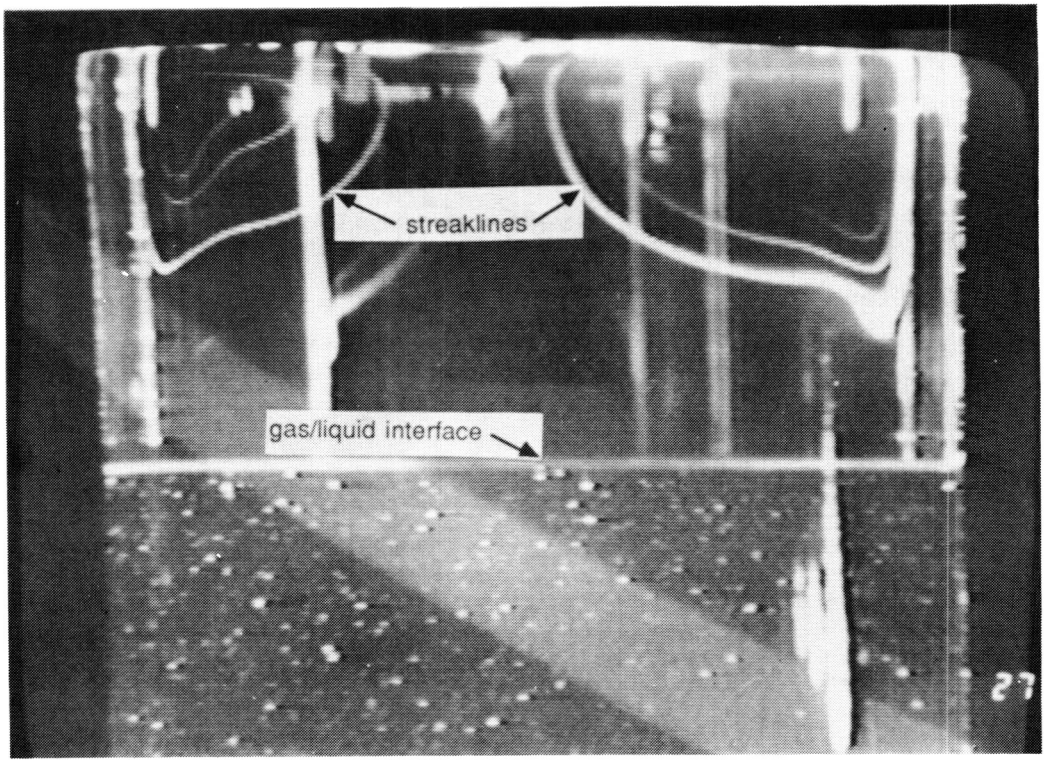

Figure A.1: Streaklines formed by R113 droplets injected into gas phase of 1-g two-phase experiment (vertical streaks are reflections of light off the test cell). Photo displays both liquid and gas phases at $t = 7$ seconds after heater is started. The liquid phase has aluminum oxide particles in suspension.

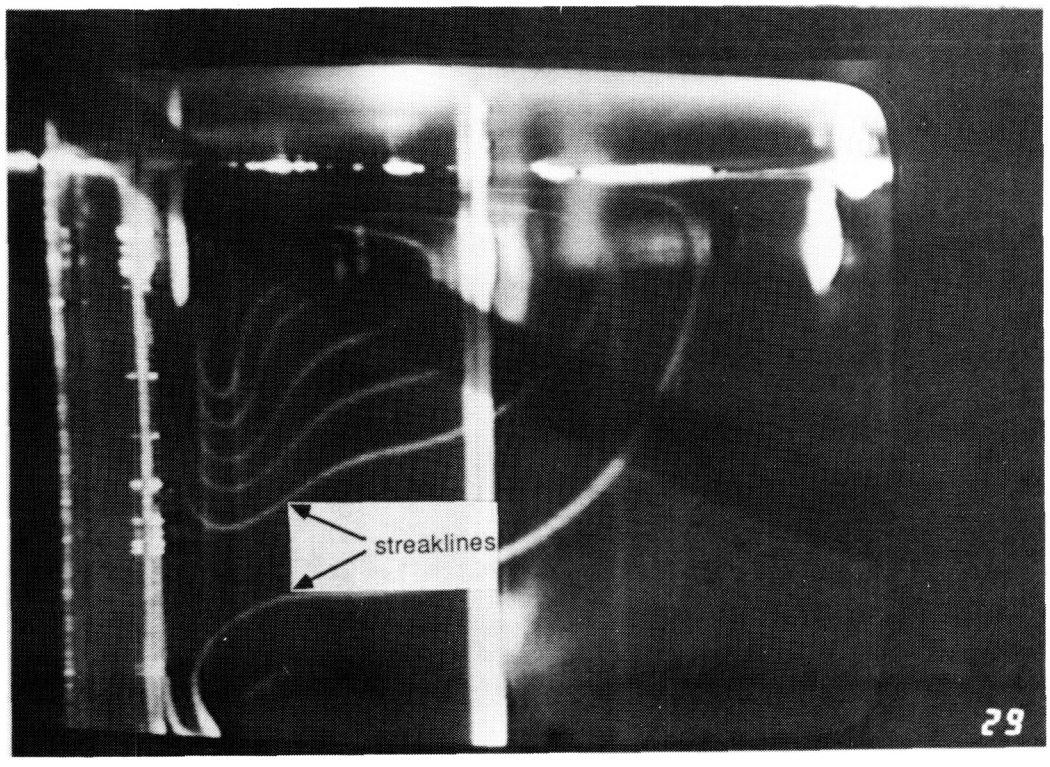

Figure A.2: Closeup photo of one-half the gas phase at $t = 25$ seconds in 1-g two-phase experiment. Streaklines are formed by R113 droplets (the large vertical streaks are reflections of light off the test cell). The left side of the photo is the axis of symmetry of the test cell.

2. Injection of Tracer Particles

In the 1-g tests performed to date, aluminum oxide particles are injected and mixed into the liquid by hand. The vapor tracer droplets are injected by hand via a hypodermic needle in the center of the heater. For drop tower and space-based tests, a remote injection and stirring capability is required for the tracer particles.

3. Light Sheet

The laser light sheet is produced by an argon or helium-neon laser, a cylindrical lens, and a converging lens, as shown on Figure A.3. The thin sheet of light (about 1 mm thick) illuminates a single plane of the flow in order to trace the particle velocities in the plane. In the 1-g tests two light sheets oriented in different planes will be used to check for axisymmetry of the flow. The effectiveness of the flow visualization system depends on both the intensity of the light source (i.e., the laser power) and the ability of the recording system (i.e., the camera) to detect low light levels. The laser selected for drop tower experimentation must survive the 30-g impact of the drop. A commercially available, DC-powered helium-neon laser which meets this requirement has been identified for drop tower use. The 5 mW laser, including power supply, is 18" long with a 1.5" diameter. Because the experimental volume of the Shuttle "special can" is comparable to the drop tower package, this laser is a good candidate for the Shuttle experiment. Another good candidate is a diode-pumped yag rod laser. This laser represents the current state-of-the-art in small, relatively high intensity (about 20 mW) lasers which do not require much power. Final selection of the laser for space-based experimentation is TBD.

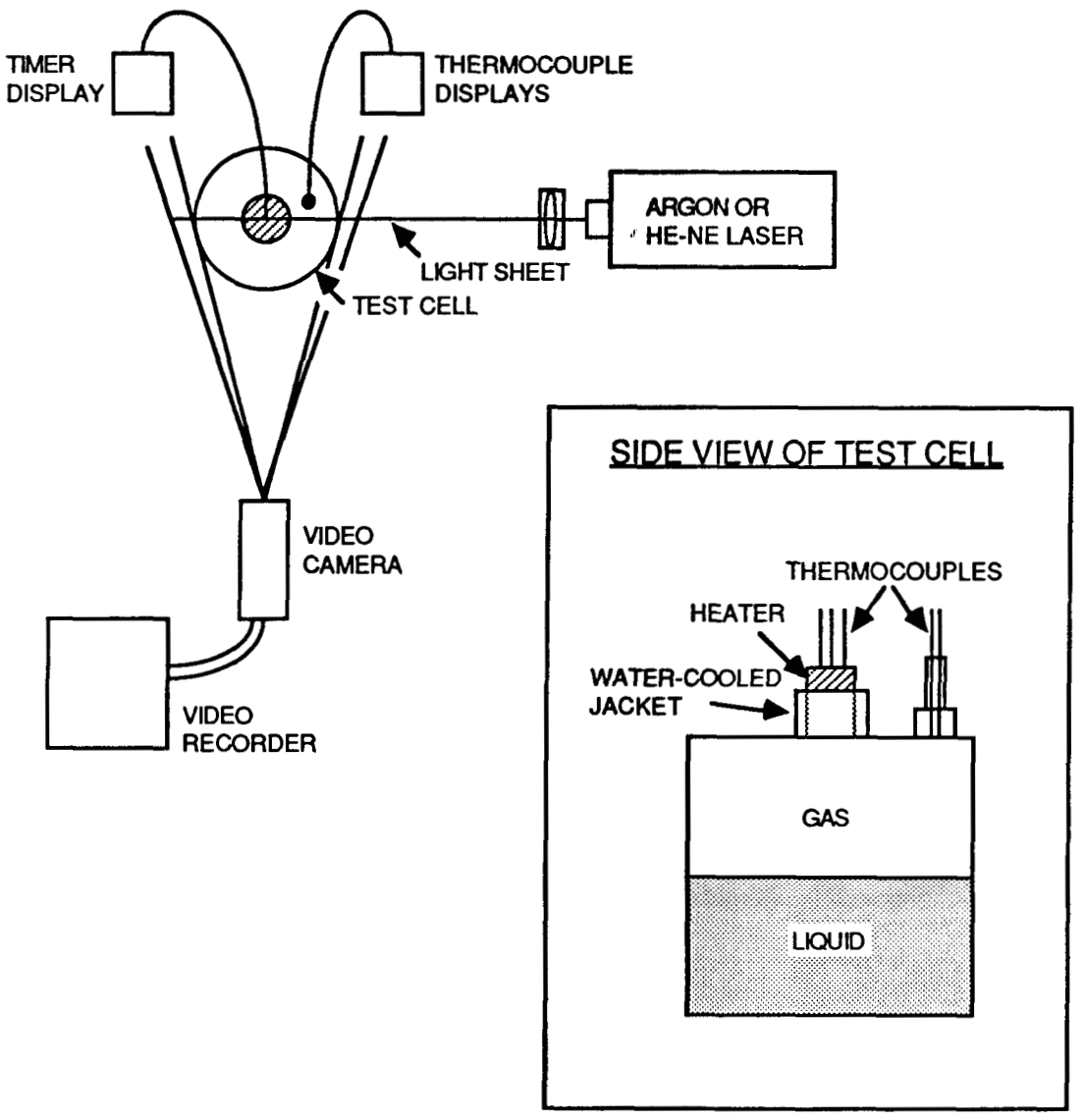

Figure A.3: Schematic view of the test cell arrangement. Light sheet serves to illuminate single plane of axisymmetric test cell. Not shown is rectangular chamber around test cell which serves to reduce distortion due to refraction.

4. Recording System

Within the volume constraints of the experiment, a tradeoff exists between laser intensity and the ability of the recording system to detect low levels of light. The selection of a low-power (5 mW) laser for drop tower (and perhaps Shuttle) experiments results in the requirement of a motion picture camera with high resolution at very low light intensities for these tests. To determine flow speeds on the order of 10 cm/sec within ± 2 mm/sec accuracy, the camera speed should be at least 100 frames/sec with exposure times less than approximately 50 μsec. This maximum exposure time represents the time required for a tracer droplet or particle to move 5 μm at a velocity of 10 cm/sec. As previously mentioned, liquid surface velocities may not be measurable in drop tower or Shuttle experiments. If this is the case, the maximum velocity in the liquid at least 1 mm below the surface may be only of order 1 cm/sec. Hence camera exposure times of less than 500 μsec may be required.

Temperature Measurement System. Thermocouples will be used to obtain temperature measurements of the ambient air, the heater surface, the container walls, and selected locations in the liquid and gas phases. Although thermocouples are "intrusive," no effect of their presence on the flow pattern was observed in 1-g feasibility tests. Because thermocouples provide information at only a few discrete locations, interferometry was explored as a technique for providing whole field quantification in the 1-g experiments. Interferometry is not planned for drop tower or space-based tests due to concerns about optical alignment and instrumentation survivability. Of the optical methods available for temperature measurement, holographic interferometry is preferred for the 1-g experiments. This technique provides whole field quantification non-intrusively. Additionally, a rainbow schlieren deflectometer was used in

feasibility tests to provide qualitative information on the temperature gradient field in each phase. In these tests a heated wire was placed in air just above a liquid silicon oil surface. A holographic interferometer with electronic heterodyne data reduction was also used in these tests to quantify the temperature fields near the wire with a spatial resolution of 100 μm. The measurement accuracies in the gas and liquid phases were 0.6% and 1.8%, respectively. The somewhat larger variance in the liquid phase resulted from the uncertainty in the determination of refractive index based upon temperature, whereas accurate tabulated values were available for the gas phase measurements.

For wall temperature measurements, chromel-constantan, type E, 30 gauge wire thermocouples will be used with wires running up the side walls. For liquid and gas phase measurements, the wire leads should go in a horizontal plane across the container and through the opposite walls of the test cell. Threaded plugs made from the container material (e.g., plexiglass) may be used to install and remove thermocouples used for the liquid and gas phases. Fine thermocouple wires (approximately 75 μm diameter) with butt-end junctions may be used for the ground-based tests. However, this set-up may be inadequate for drop tower and space-based tests.

The measurement of surface temperature distribution with, say, a thin thermocouple probe would be highly desirable and achievable in 1-g. However, positioning of the probe close to the surface is very difficult to do in reduced gravity because the exact location of the free surface cannot be specified a priori. Even with the proposed liquid-gas interface control system, the free surface may deform 1–2 mm. Moreover, the free surface deforms a certain extent due to fluid motion and g-jitter. The probe

could be positioned manually after the flow is started, but doing this at several radial locations for the surface temperature distribution measurement may be too time consuming. For the drop tower experiment, such a manual positioning is impossible.

Due to the aforementioned problems associated with fluid temperature measurement, the reduced gravity experiments may only incorporate provisions for wall temperature measurements.

Liquid-Gas Interface Control System. Reduced gravity experiments introduce the problem of liquid-gas interface surface curvature. In order to prevent such curvature and to make the comparison of earth and reduced gravity experiments straightforward, special precautions are required to "pin" the interface and maintain a flat shape. Drop tower experiments have been conducted in the NASA-LeRC 5.18 second facility which use internal flanges in the test cell (see Figure A.4). These experiments were successful in significantly reducing surface curvature, as shown on Figures A.5 and A.6. Some surface motion was observed throughout the first four seconds of the drop. It is believed that this motion will be eliminated by more exact filling techniques. The internal flanges will be used in both the drop tower and space-based experiments to maintain a flat liquid-gas interface with a 0.04 radian maximum local angle of the liquid surface. The positioning of these flanges along the container walls should be adjustable to allow for a variation in the liquid fill level.

Software for Data Collection. Temperature and flow visualization measurement data from the experiments must be collected and analyzed. A commercially-available data acquisition and control system has been identified for the drop tower experiments. This system is capable of sampling at the rate of 100 readings/second/channel on each of 8 channels. With its digital I/O, it is capable of control functions. The

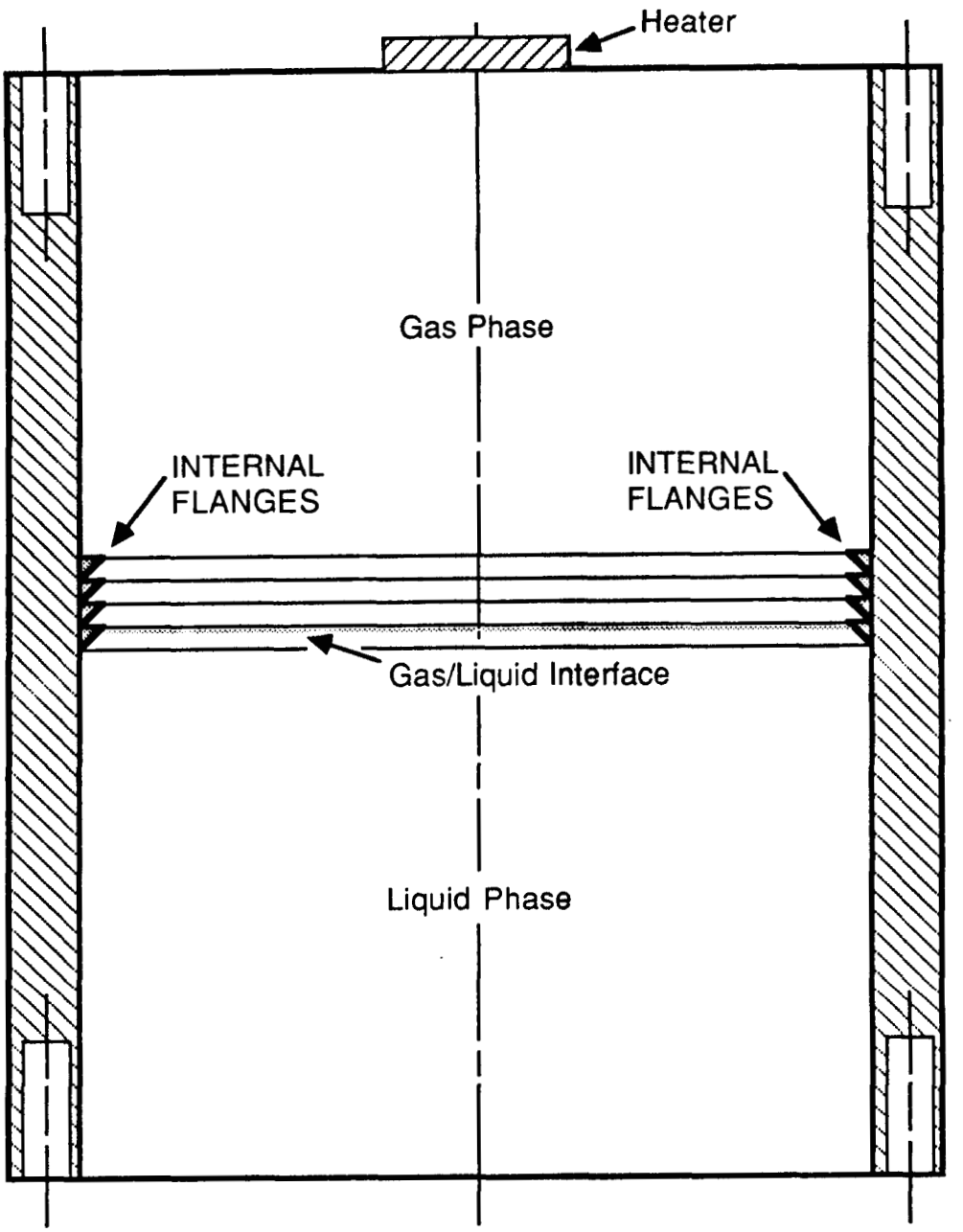

Figure A.4: Internal flanges used to "pin" the gas-liquid interface. Peak-to-peak length and distance from the wall are 1/16 inch (1.6 mm).

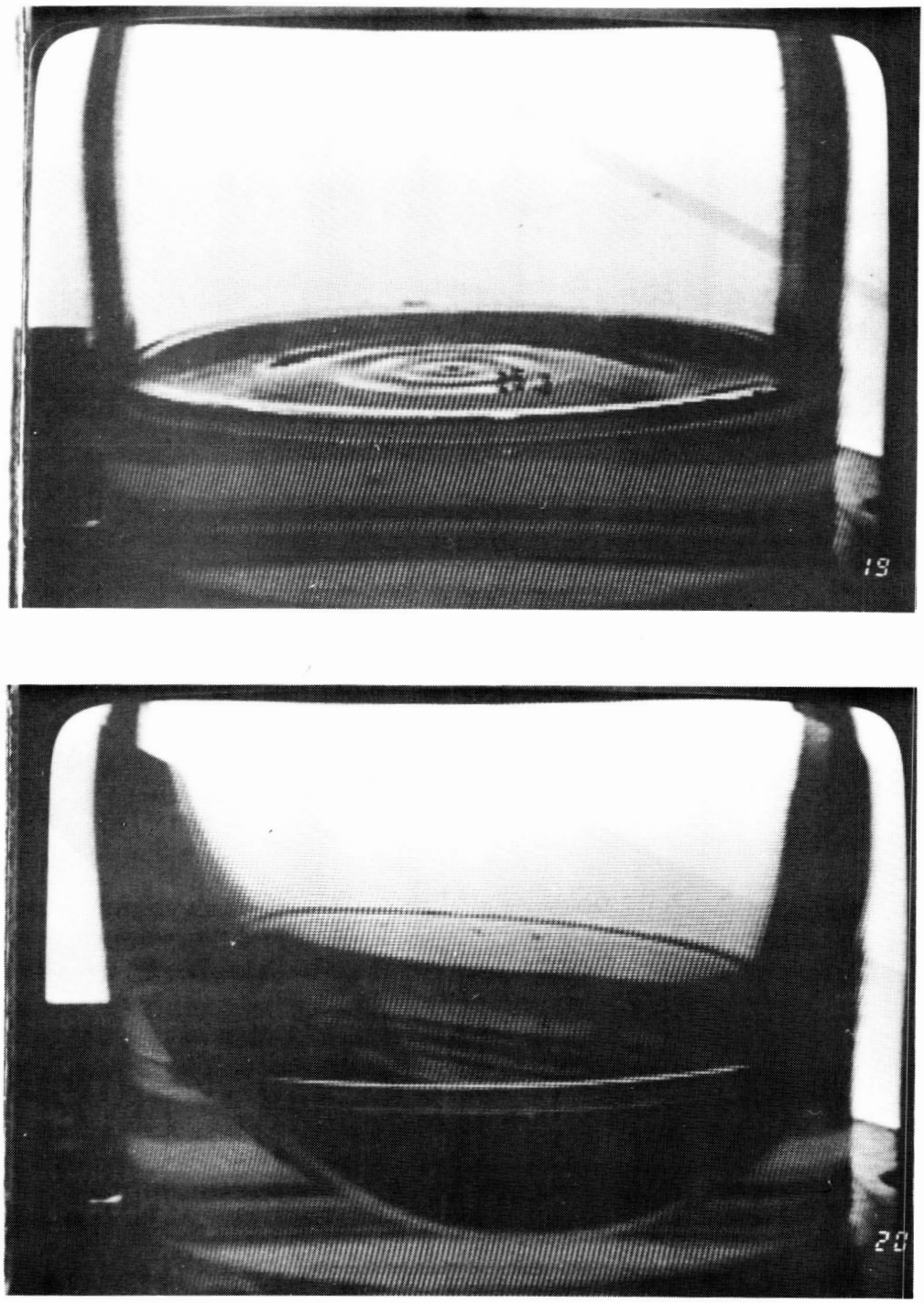

Figure A.5: (a) and (b) display the liquid position in a 10 cm tank at various times in a 5.18 second drop. (a): about 0.1 seconds after drop start. (b): about 4 seconds later; note the liquid has crept along sidewall, forming a nearly hemispherical shape.

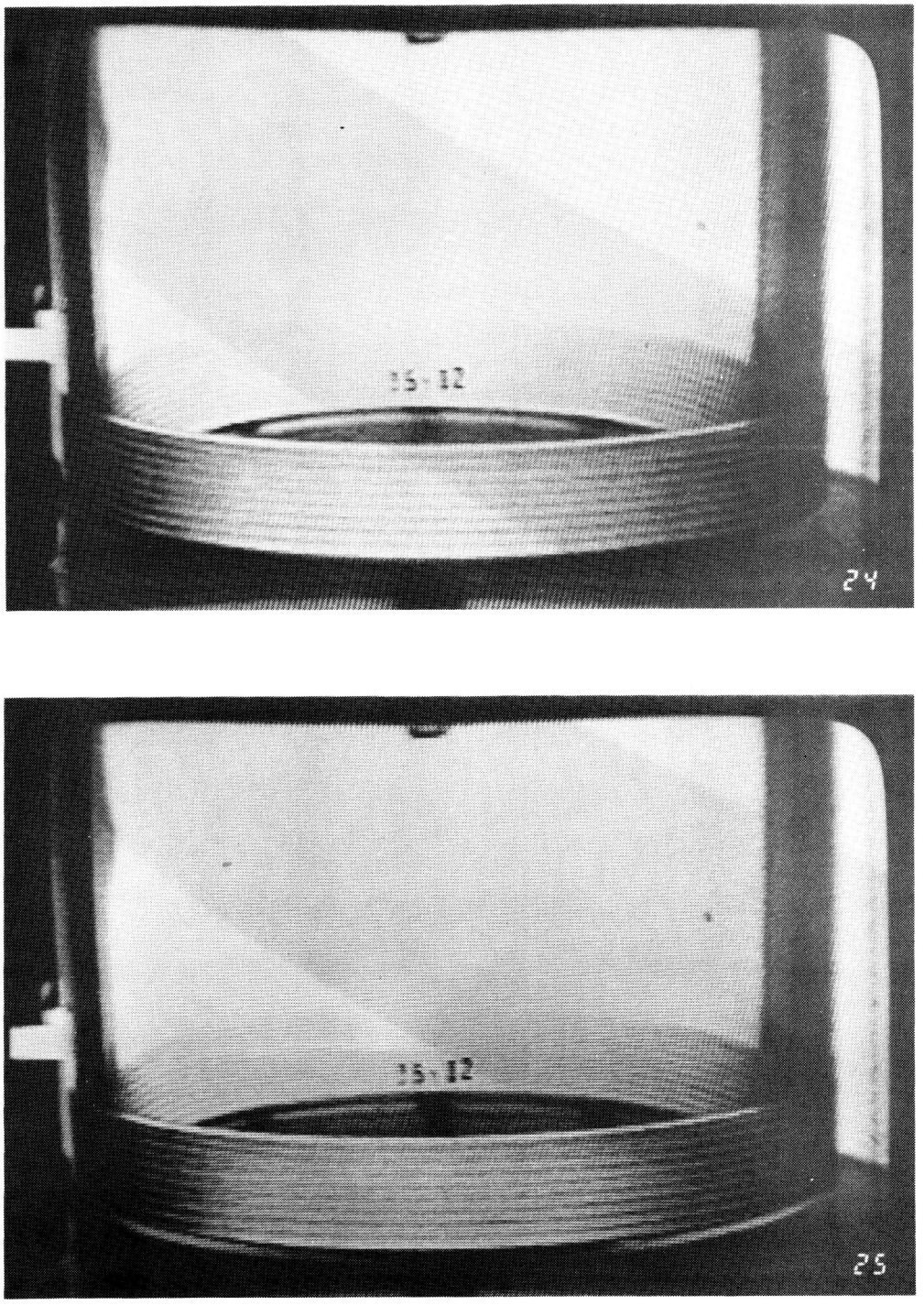

Figure A.6: (a) and (b) are analogous to (a) and (b) in Figure A.5 except that internal flanges have been installed in the tank. These prevent the liquid migration and serve to "pin" the liquid-gas interface nearly flat.

selection of the data acquisition and control system for the Shuttle experiments has not yet been finalized.

In order to quantify the flow visualization, software has been developed for use with an NEC motion analyzer which digitizes 16 mm motion picture frames. Data collected on the Shuttle will be evaluated on the ground.

Safety Precautions

Since the experiments will not involve flames or flammable or toxic substances, no special handling requirements or safety precautions are required (non-decomposed R113 is classified as nonflammable and nontoxic by [18]). Standard OSHA (for ground-based) and Shuttle or Space Station (for space-based) guidelines should be followed for the operation of the experiments. A temperature control and automatic shutoff system should be used in the heater design for overtemperature protection. Although the heater will be insulated in the experiment, computer simulations have indicated that the outside wall temperature around the gas phase may reach approximately 340 K in a one-hour experiment. Therefore care should be taken when handling the test cell during and/or after an experiment.

Appendix B

Derivation of Energy Equation

In order to write the thermal energy equation in terms of excess enthalpy, we define for the i^{th} species (all quantities dimensional unless otherwise specified)

$$h_{i,\text{excess}} \equiv \overline{c}_{p_i}(T - T^o) = \overline{c}_{p_i} T_1 \tag{B.1}$$

where

$$\begin{aligned}
h_1 &= \sum_i Y_i h_{1,i} = \overline{c}_p T_1 = h - h^o \\
h_i &= h_i^o + h_{i,\text{excess}} = h_i^o + h_{1,i} \\
h_i^o &= h_i(T^o) = \text{formation enthalpy} \\
T^o &= T_* = 300 \text{ K (reference temperature)} \\
h &= \sum_i Y_i h_i \\
h^o &= \sum_i Y_i h_i^o \\
\overline{c}_{p_i} &= \left(\frac{1}{T - T^o}\right) \int_{T^o}^{T} c_{p_i}(T) dT \\
\overline{c}_p &= \sum_i Y_i \overline{c}_{p_i}
\end{aligned} \tag{B.2}$$

The thermal energy equation will be derived in rectangular coordinates for the two-dimensional planar geometry. The results will then be generalized to apply also to the cylindrical geometry.

To obtain the thermal energy equation, we derive the total energy and mechanical energy equations, and subtract the latter from the former to get the thermal energy equation. The following notation will be used:

$$
\begin{aligned}
\hat{u}_i &= \text{internal energy per unit mass of species } i \\
\frac{1}{2}v_i^2 &= \frac{1}{2}(\vec{v}_i \cdot \vec{v}_i) = \text{kinetic energy per unit mass of species } i \\
\tau_{xx} &= \mu\left[2\frac{\partial u}{\partial x} - \frac{2}{3}\vec{\nabla}\cdot\vec{v}\right] \\
\tau_{yy} &= \mu\left[2\frac{\partial v}{\partial y} - \frac{2}{3}\vec{\nabla}\cdot\vec{v}\right] \\
\tau_{yx} &= \tau_{xy} = \mu\left[\frac{\partial v}{\partial x} + \frac{\partial u}{\partial y}\right] \\
\begin{bmatrix} \vec{F}_x \\ \vec{F}_y \end{bmatrix} &= \begin{bmatrix} P - \tau_{xx} & -\tau_{xy} \\ -\tau_{yx} & P - \tau_{yy} \end{bmatrix} \begin{bmatrix} \vec{i} \\ \vec{j} \end{bmatrix} \\
\dot{Q}_V = \frac{d\dot{Q}}{dV} &= \text{volumetric heat source term} \\
&\quad \text{(energy production per unit volume per unit time)} \\
\Phi &= \text{viscous dissipation function (see [16], eqn A.16)}
\end{aligned}
$$

Notice that the sign convention for the shear stresses is opposite to [15]. For a two-dimensional control volume $dx \cdot dy$, the conservation of total energy is

$$
\left\{\begin{array}{c}\text{rate of}\\ \text{accumulation}\\ \text{of internal}\\ \text{and kinetic}\\ \text{energy}\end{array}\right\} = \left\{\begin{array}{c}\text{net rate of}\\ \text{internal and}\\ \text{kinetic energy}\\ \text{in by convection}\\ \text{and diffusion}\end{array}\right\} + \left\{\begin{array}{c}\\ \text{net rate of}\\ \text{heat addition}\\ \text{by conduction}\\ \\ \end{array}\right\} +
$$

$$+ \left\{ \begin{array}{c} \text{net rate of} \\ \text{work done on} \\ \text{element by} \\ \text{surroundings} \end{array} \right\} + \left\{ \begin{array}{c} \text{net rate of} \\ \text{heat addition} \\ \text{by sources} \end{array} \right\} \tag{B.3}$$

An Eulerian point of view will be used for the derivation (fluid flows through a control volume which is fixed in space).

The rate of accumulation of internal and kinetic energy is

$$\frac{\partial}{\partial t}\left[\sum_i (\hat{u}_i + \frac{1}{2}v_i^2)Y_i\rho\right] dx\, dy \tag{B.4}$$

where $\rho = \rho_{\text{mix}}$ = density of the mixture and (following [22])

$$v_i^2 = \vec{v}_i \cdot \vec{v}_i \tag{B.5}$$

$$\vec{v}_i = \vec{v'} + \vec{V}_i \tag{B.6}$$

$$\vec{v'} = \sum_i Y_i \vec{v}_i = \vec{v}_A \tag{B.7}$$

$$\vec{V}_i = -\frac{\mathcal{D}_{ij}\nabla Y_i}{Y_i} \tag{B.8}$$

In equation (B.6), $\vec{v}_i$ is the local average velocity of species i (relative to stationary coordinate axes), $\vec{v'}$ is the mass-weighted average velocity of the fluid mixture [given by equation (B.7)], and $\vec{V}_i$ is the diffusion velocity of species i [given by equation (B.8) which follows from Fick's law of diffusion].

Substituting equations (B.5)–(B.8) into equation (B.4) gives

$$\frac{\partial}{\partial t}\left[\sum_i (\hat{u}_i + \frac{1}{2}v_i^2)Y_i\rho\right] dx\, dy = \frac{\partial}{\partial t}\left(\rho \sum_i Y_i \hat{u}_i\right) dx\, dy +$$
$$\frac{\partial}{\partial t}\left[\frac{1}{2}\rho(\vec{v'}\cdot\vec{v'})\sum_i Y_i + \rho\sum_i (\vec{v'}\cdot\vec{V}_i)Y_i + \frac{1}{2}\rho\sum_i (\vec{V}_i\cdot\vec{V}_i)Y_i\right] dx\, dy$$

Since

$$\hat{u} = \sum_i Y_i \hat{u}_i = \text{internal energy of mixture} \tag{B.9}$$

$$\sum_i Y_i = 1 \tag{B.10}$$

$$\sum_i (\vec{v}' \cdot \vec{V}_i) Y_i = \vec{v}' \cdot \sum_i Y_i \vec{V}_i = 0 \tag{B.11}$$

[$\sum_i Y_i \vec{V}_i = 0$ follows from equations (B.6), (B.7), and (B.10)], the rate of accumulation of internal and kinetic energy is

$$\frac{\partial}{\partial t}\left[\sum_i (\hat{u}_i + \frac{1}{2} v_i^2) Y_i \rho\right] dx\, dy = \frac{\partial}{\partial t}(\rho \hat{u} + \frac{1}{2}\rho \vec{v}' \cdot \vec{v}') dx\, dy + \frac{1}{2}\frac{\partial}{\partial t}\left(\rho \sum_i Y_i \vec{V}_i \cdot \vec{V}_i\right) dx\, dy \tag{B.12}$$

For diffusion in a nonstationary medium, the total mass flux of species i (denoted by $\vec{n}_i$) is given by

$$\vec{n}_i = \rho Y_i \vec{v}' - \rho \mathcal{D}_{ij} \nabla Y_i = \rho Y_i (\vec{v}' + \vec{V}_i) \tag{B.13}$$

The first term on the right hand side of equation (B.13) is the convection of the mass-weighted average fluid flow, and the second term is the diffusive contribution which represents the mass flux of the i^{th} species relative to the mass average velocity $\vec{v}'$. The amount of internal and kinetic energy which flows into the Eulerian control volume through the x-face by convection and diffusion is

$$\left[\sum_i \rho Y_i (v_x' + V_{i,x})(\hat{u}_i + \frac{1}{2} v_i^2)\right]_x dy$$

while the amount of energy which flows out through the $x + dx$ face by convection and diffusion is

$$\left[\sum_i \rho Y_i (v_x' + V_{i,x})(\hat{u}_i + \frac{1}{2} v_i^2)\right]_{x+dx} dy$$

Hence for the x-direction, the net rate of energy in by convection and diffusion is

$$-\frac{\partial}{\partial x}\left[\sum_i \rho Y_i (v_x' + V_{i,x})(\hat{u}_i + \frac{1}{2} v_i^2)\right] dx\, dy$$

Similarly, the net rate of energy in by convection and diffusion in the y-direction is

$$-\frac{\partial}{\partial y}\left[\sum_i \rho Y_i(v_y' + V_{i,y})(\hat{u}_i + \frac{1}{2}v_i^2)\right] dx\, dy$$

Therefore the total net rate of energy in by convection and diffusion is

$$-\vec{\nabla}\cdot\left[\sum_i \rho Y_i(\vec{v'} + \vec{V}_i)(\hat{u}_i + \frac{1}{2}v_i^2)\right] dx\, dy$$

In the above equation $v_i^2 = \vec{v}_i\cdot\vec{v}_i$ where $\vec{v}_i$ is given by equation (B.6). Therefore, substituting equation (B.6) into the above equation yields

$$\begin{aligned}
&-\vec{\nabla}\cdot\left[\sum_i \rho Y_i(\vec{v'} + \vec{V}_i)(\hat{u}_i + \frac{1}{2}v_i^2)\right] dx\, dy = \\
&\quad = -\vec{\nabla}\cdot\left[\rho\sum_i Y_i(\vec{v'} + \vec{V}_i)(\hat{u}_i + \frac{1}{2}\vec{v'}\cdot\vec{v'} + \vec{v'}\cdot\vec{V}_i + \frac{1}{2}\vec{V}_i\cdot\vec{V}_i)\right] dx\, dy \\
&\quad = -\vec{\nabla}\cdot\left[\rho\vec{v'}\sum_i Y_i\hat{u}_i + \rho\sum_i Y_i\hat{u}_i\vec{V}_i\right] dx\, dy \\
&\qquad -\vec{\nabla}\cdot\left[\frac{1}{2}\rho(\vec{v'}\cdot\vec{v'})\vec{v'}\sum_i Y_i + \rho\vec{v'}\sum_i(\vec{v'}\cdot\vec{V}_i)Y_i\right. \\
&\qquad \left. + \frac{1}{2}\rho\vec{v'}\sum_i(\vec{V}_i\cdot\vec{V}_i)Y_i\right] dx\, dy \\
&\qquad -\vec{\nabla}\cdot\left[\frac{1}{2}\rho(\vec{v'}\cdot\vec{v'})\sum_i Y_i\vec{V}_i + \rho\sum_i Y_i\vec{V}_i(\vec{v'}\cdot\vec{V}_i)\right. \\
&\qquad \left. + \frac{1}{2}\rho\sum_i Y_i\vec{V}_i(\vec{V}_i\cdot\vec{V}_i)\right] dx\, dy
\end{aligned}$$

Using equations (B.5), (B.6), and (B.9)-(B.11), the total net rate of energy in by convection and diffusion is

$$\begin{aligned}
&-\vec{\nabla}\cdot\left(\rho\vec{v'}\hat{u} + \rho\sum_i Y_i\hat{u}_i\vec{V}_i\right) dx\, dy \\
&-\vec{\nabla}\cdot\left[\frac{1}{2}\rho\vec{v'}(\vec{v'}\cdot\vec{v'}) + \frac{1}{2}\rho\vec{v'}\sum_i(\vec{V}_i\cdot\vec{V}_i)Y_i\right] dx\, dy \qquad \text{(B.14)} \\
&-\vec{\nabla}\cdot\left[\rho\sum_i Y_i\vec{V}_i(\vec{v'}\cdot\vec{V}_i) + \frac{1}{2}\rho\sum_i Y_i\vec{V}_i(\vec{V}_i\cdot\vec{V}_i)\right] dx\, dy
\end{aligned}$$

Denoting

$$k = \text{the mixture thermal conductivity,}$$

the rate of heat addition in by conduction is

$$\left(-k\frac{\partial T}{\partial x}\right)_x dy + \left(-k\frac{\partial T}{\partial y}\right)_y dx$$

while the rate of heat addition out by conduction is

$$\left(-k\frac{\partial T}{\partial x}\right)_{x+dx} dy + \left(-k\frac{\partial T}{\partial y}\right)_{y+dy} dx$$

Therefore the net rate of heat addition by conduction is

$$(\vec{\nabla}\cdot k\nabla T)dx\,dy \tag{B.15}$$

Notice that radiative heating of the gas has not been included in the analysis.

Work is done on the element by body forces (gravity) and surface forces (pressure and shear forces)[1]. The rate at which work is done by the body forces is the force times the velocity:

$$\rho\vec{g}\cdot\vec{v}'dx\,dy$$

Similarly, the rate at which work is done on the element at a face is the vector dot product of velocity and force. For example, on the x-face of the element the force in the x-direction is $(P-\tau_{xx})_x\vec{i}$. Therefore the net work done on the element at the x-face in the x-direction is

$$dy(P-\tau_{xx})_x\vec{i}\cdot\vec{v}' = v_x'(P-\tau_{xx})_x dy$$

Similarly, work done on the element at the x-face in the y-direction is

$$(-\tau_{xy}dy)_x\vec{j}\cdot\vec{v}' = -v_y'\,\tau_{xy}|_x\,dy$$

[1]In the derivation of the work done on the element, the contribution of work done by diffusion has been neglected to simplify the analysis.

Therefore, for the x-face the work done on the element is

$$(\vec{v'} \cdot \vec{F}_x)_x dy$$

The convention for positive shear stresses is such that a positive stress has opposite direction in opposing planes. This is usually the case. However in some instances, such as if the center of the control volume is along the centerline of a Poiseuille flow, the direction of positive shear is the same for opposite planes of the control volume. To be precise in general, therefore, the net force from pressure and shear on the x and $x + dx$ faces is of order dy. Using the previously defined positive shear directions, the work done on the control volume at the $x + dx$ face is

$$-(\vec{v'} \cdot \vec{F}_x)_{x+dx} dy$$

The net work done on the element at the x and $x + dx$ faces is therefore

$$-\frac{\partial}{\partial x}(\vec{v'} \cdot \vec{F}_x) dx\, dy$$

For the y and $y + dy$ faces, the total work done on the element is

$$-\frac{\partial}{\partial y}(\vec{v'} \cdot \vec{F}_y) dx\, dy$$

By adding the contributions at all four faces, we get the total work done on the element by surface forces:

$$-\left[\frac{\partial}{\partial x}(\vec{v'} \cdot \vec{F}_x) + \frac{\partial}{\partial y}(\vec{v'} \cdot \vec{F}_y)\right] dx\, dy$$

Therefore the net rate of work done on the element by the surroundings (body forces and surfaces forces) is

$$\left\{\rho \vec{g} \cdot \vec{v'} - \left[\frac{\partial}{\partial x}(\vec{v'} \cdot \vec{F}_x) + \frac{\partial}{\partial y}(\vec{v'} \cdot \vec{F}_y)\right]\right\} dx\, dy \qquad \text{(B.16)}$$

The net rate of heat addition by sources is given by the volume of the element multiplied by the volumetric heat source term, $\dot{Q}_V$:

$$\dot{Q}_V dx\, dy \tag{B.17}$$

By substituting equations (B.12)-(B.17) into equation (B.3) and dividing both sides by $dx\, dy$, we are left with the total energy equation (before applying continuity):

$$\begin{aligned}
&\frac{\partial}{\partial t}(\rho\hat{u} + \frac{1}{2}\rho\vec{v}\cdot\vec{v}) + \frac{1}{2}\frac{\partial}{\partial t}\left(\rho\sum_i Y_i\vec{V}_i\cdot\vec{V}_i\right) = \\
&\quad = -\vec{\nabla}\cdot\left(\rho\hat{u}\vec{v} + \rho\sum_i Y_i\hat{u}_i\vec{V}_i\right) - \vec{\nabla}\cdot\left[\frac{1}{2}\rho\vec{v}(\vec{v}\cdot\vec{v})\right. \\
&\qquad \left. + \frac{1}{2}\rho\vec{v}\sum_i Y_i(\vec{V}_i\cdot\vec{V}_i)\right] \\
&\qquad -\vec{\nabla}\cdot\left[\rho\sum_i Y_i\vec{V}_i(\vec{v}\cdot\vec{V}_i) + \frac{1}{2}\rho\sum_i Y_i\vec{V}_i(\vec{V}_i\cdot\vec{V}_i)\right] \\
&\qquad +\vec{\nabla}\cdot k\nabla T + \rho\vec{g}\cdot\vec{v} - \left[\frac{\partial}{\partial x}(\vec{v}\cdot\vec{F}_x) + \frac{\partial}{\partial y}(\vec{v}\cdot\vec{F}_y)\right] + \dot{Q}_V
\end{aligned}$$

In order to simplify the equation, we will use the overall continuity equation,

$$\frac{\partial\rho}{\partial t} + \vec{v}\cdot\nabla\rho + \rho\vec{\nabla}\cdot\vec{v} = \frac{\partial\rho}{\partial t} + \vec{\nabla}\cdot(\rho\vec{v}) = 0 \tag{B.18}$$

The first term on the left hand side and the first term on the right hand side of the total energy equation can be combined with the help of equation (B.18) to give

$$\begin{aligned}
&\frac{\partial}{\partial t}(\rho\hat{u}) + \vec{\nabla}\cdot(\rho\hat{u}\vec{v}) = \\
&\quad = \hat{u}\left[\frac{\partial\rho}{\partial t} + \vec{\nabla}\cdot(\rho\vec{v})\right] + \rho\frac{\partial\hat{u}}{\partial t} + \rho\vec{v}\cdot\nabla\hat{u} \\
&\quad = \rho\left[\frac{\partial\hat{u}}{\partial t} + \vec{v}\cdot\nabla\hat{u}\right] \\
&\quad = \rho\frac{D\hat{u}}{Dt}
\end{aligned}$$

Similarly, we can write

$$\frac{\partial}{\partial t}(\frac{1}{2}\rho\vec{v'}\cdot\vec{v'}) + \vec{\nabla}\cdot[\frac{1}{2}\rho\vec{v'}(\vec{v'}\cdot\vec{v'})] =$$
$$= \frac{1}{2}(\vec{v'}\cdot\vec{v'})\left[\frac{\partial\rho}{\partial t} + \vec{\nabla}\cdot(\rho\vec{v'})\right] + \frac{1}{2}\rho\left[\frac{\partial(\vec{v'}\cdot\vec{v'})}{\partial t} + \vec{v'}\cdot\nabla(\vec{v'}\cdot\vec{v'})\right]$$
$$= \rho\frac{D}{Dt}(\frac{1}{2}\vec{v'}\cdot\vec{v'})$$

and

$$\frac{1}{2}\frac{\partial}{\partial t}\left(\rho\sum_i Y_i\vec{V}_i\cdot\vec{V}_i\right) + \vec{\nabla}\cdot\left(\frac{1}{2}\rho\vec{v'}\sum_i Y_i\vec{V}_i\cdot\vec{V}_i\right) =$$
$$= \frac{1}{2}\sum_i Y_i\vec{V}_i\cdot\vec{V}_i\left[\frac{\partial\rho}{\partial t} + \vec{\nabla}\cdot(\rho\vec{v'})\right]$$
$$+\frac{1}{2}\rho\left[\frac{\partial}{\partial t}\sum_i Y_i\vec{V}_i\cdot\vec{V}_i + \vec{v'}\cdot\nabla\sum_i Y_i\vec{V}_i\cdot\vec{V}_i\right]$$
$$= \frac{1}{2}\rho\frac{D}{Dt}\left(\sum_i Y_i\vec{V}_i\cdot\vec{V}_i\right)$$

The above equations were each simplified using the overall continuity equation [equation (B.18)]. Substituting these three equations, the total energy equation becomes

$$\rho\frac{D}{Dt}(\hat{u} + \frac{1}{2}\vec{v'}\cdot\vec{v'}) + \frac{1}{2}\rho\frac{D}{Dt}\left(\sum_i Y_i\vec{V}_i\cdot\vec{V}_i\right) =$$
$$= -\vec{\nabla}\cdot\left\{\rho\sum_i[Y_i\hat{u}_i\vec{V}_i + Y_i\vec{V}_i(\vec{v'}\cdot\vec{V}_i) + \frac{1}{2}Y_i\vec{V}_i(\vec{V}_i\cdot\vec{V}_i)]\right\}$$
$$+\vec{\nabla}\cdot k\nabla T + \rho\vec{g}\cdot\vec{v'} - \left[\frac{\partial}{\partial x}(\vec{v'}\cdot\vec{F}_x) + \frac{\partial}{\partial y}(\vec{v'}\cdot\vec{F}_y)\right] + \dot{Q}_V \qquad \text{(B.19)}$$

The mechanical energy equation is the dot product of velocity (neglecting mechanical work by diffusion, we use the mass-weighted average velocity of the fluid mixture) with the momentum equation [equation (6.5)]. The momentum equation (where we now replace $\vec{V}$ with $\vec{v'}$) is

$$\rho\frac{D\vec{v'}}{Dt} = -\nabla P + [\vec{\nabla}\cdot\vec{\tau}] + \rho\vec{g} \qquad \text{(B.20)}$$

Substituting the stress tensor into the momentum equation, equation (B.20) becomes

$$\rho\frac{D\vec{v}}{Dt} = -\nabla P + \left(\frac{\partial\tau_{xx}}{\partial x} + \frac{\partial\tau_{yx}}{\partial y}\right)\vec{i} + \left(\frac{\partial\tau_{xy}}{\partial x} + \frac{\partial\tau_{yy}}{\partial y}\right)\vec{j} + \rho\vec{g}$$

In terms of $\vec{F}_x$ and $\vec{F}_y$, the above equation is

$$\rho\frac{D\vec{v}}{Dt} = -\frac{\partial\vec{F}_x}{\partial x} - \frac{\partial\vec{F}_y}{\partial y} + \rho\vec{g}$$

Therefore the mechanical energy equation is

$$\rho\vec{v}\cdot\frac{D\vec{v}}{Dt} = -\vec{v}\cdot\left[\frac{\partial}{\partial x}(\vec{F}_x) + \frac{\partial}{\partial y}(\vec{F}_y)\right] + \rho\vec{v}\cdot\vec{g} \qquad \text{(B.21)}$$

To get the desired thermal energy equation, we subtract the mechanical energy equation [(B.21)] from the total energy equation [(B.19)]. To do this, it is easiest to re-write the contribution of net work done on the element in the total energy equation first. Applying the chain rule to this part of equation (B.21), we get

$$\begin{aligned}
&-\frac{\partial}{\partial x}(\vec{v}\cdot\vec{F}_x) - \frac{\partial}{\partial y}(\vec{v}\cdot\vec{F}_y) + \rho\vec{g}\cdot\vec{v} = \\
&\quad = -\vec{v}\cdot\left[\frac{\partial}{\partial x}(\vec{F}_x) + \frac{\partial}{\partial y}(\vec{F}_y)\right] + \rho\vec{v}\cdot\vec{g} - \vec{F}_x\cdot\frac{\partial\vec{v}}{\partial x} - \vec{F}_y\cdot\frac{\partial\vec{v}}{\partial y}
\end{aligned}$$

Using the above identity, subtracting equation (B.21) from equation (B.19) leaves the thermal energy equation

$$\begin{aligned}
&\rho\frac{D}{Dt}(\hat{u} + \frac{1}{2}\vec{v}\cdot\vec{v}) - \rho\vec{v}\cdot\frac{D\vec{v}}{Dt} + \frac{1}{2}\rho\frac{D}{Dt}\left(\sum_i Y_i\vec{V}_i\cdot\vec{V}_i\right) = \\
&\quad = -\vec{\nabla}\cdot\left\{\rho\sum_i[Y_i\hat{u}_i\vec{V}_i + Y_i\vec{V}_i(\vec{v}\cdot\vec{V}_i) + \frac{1}{2}Y_i\vec{V}_i(\vec{V}_i\cdot\vec{V}_i)]\right\} \\
&\quad +\vec{\nabla}\cdot k\nabla T - \vec{F}_x\cdot\frac{\partial\vec{v}}{\partial x} - \vec{F}_y\cdot\frac{\partial\vec{v}}{\partial y} + \dot{Q}_V
\end{aligned}$$

We can also substitute for the viscous dissipation, $\mu\Phi$, which is (for two dimensions)

$$\mu\Phi - P\vec{\nabla}\cdot\vec{v} \equiv -\vec{F}_x\cdot\frac{\partial\vec{v}}{\partial x} - \vec{F}_y\cdot\frac{\partial\vec{v}}{\partial y} \qquad \text{(B.22)}$$

and also note

$$\rho\vec{v}\cdot\frac{D\vec{v}}{Dt} = \rho\frac{D}{Dt}(\frac{1}{2}\vec{v}\cdot\vec{v})$$

so that the thermal energy equation in terms of the mixture internal energy becomes

$$\rho\frac{D\hat{u}}{Dt} + \frac{1}{2}\rho\frac{D}{Dt}\left(\sum_i Y_i\vec{V}_i\cdot\vec{V}_i\right) =$$
$$= -\vec{\nabla}\cdot\left\{\rho\sum_i[Y_i\hat{u}_i\vec{V}_i + Y_i\vec{V}_i(\vec{v}\cdot\vec{V}_i) + \frac{1}{2}Y_i\vec{V}_i(\vec{V}_i\cdot\vec{V}_i)]\right\}$$
$$+\vec{\nabla}\cdot k\nabla T - P\vec{\nabla}\cdot\vec{v} + \mu\Phi + \dot{Q}_V \qquad \text{(B.23)}$$

We can re-write the thermal energy equation in terms of the specific enthalpy by using the relationships

$$Y_i h_i = Y_i\hat{u}_i + \frac{P_i}{\rho} \qquad \text{(B.24)}$$

and

$$h = \sum_i Y_i h_i = \hat{u} + \frac{P}{\rho} \qquad \text{(B.25)}$$

Substituting equations (B.24) and (B.25) into equation (B.23) gives

$$\rho\frac{Dh}{Dt} - \rho\frac{D(P/\rho)}{Dt} + \frac{1}{2}\rho\frac{D}{Dt}\left(\sum_i Y_i\vec{V}_i\cdot\vec{V}_i\right) =$$
$$= -\vec{\nabla}\cdot\left[\rho\sum_i\vec{V}_i\left(Y_i h_i - \frac{P_i}{\rho}\right)\right] - \vec{\nabla}\cdot\left\{\rho\sum_i[Y_i\vec{V}_i(\vec{v}\cdot\vec{V}_i) + \frac{1}{2}Y_i\vec{V}_i(\vec{V}_i\cdot\vec{V}_i)]\right\}$$
$$+\vec{\nabla}\cdot k\nabla T - P\vec{\nabla}\cdot\vec{v} + \mu\Phi + \dot{Q}_V$$

Noting that

$$-\rho\frac{D(P/\rho)}{Dt} = -\frac{DP}{Dt} + \frac{P}{\rho}\frac{D\rho}{Dt} = -\frac{DP}{Dt} + \frac{P}{\rho}\left(\frac{\partial\rho}{\partial t} + \vec{v}\cdot\nabla\rho\right)$$

and from the overall continuity equation [equation (B.18)]

$$\frac{\partial\rho}{\partial t} + \vec{v}\cdot\nabla\rho = -\rho\vec{\nabla}\cdot\vec{v}$$

we get

$$-\rho\frac{D(P/\rho)}{Dt} = -\frac{DP}{Dt} - P\vec{\nabla}\cdot\vec{v}$$

so that the thermal energy equation simplifies to

$$\rho\frac{Dh}{Dt}+\frac{1}{2}\rho\frac{D}{Dt}\left(\sum_i Y_i\vec{V}_i\cdot\vec{V}_i\right)=\vec{\nabla}\cdot\sum_i P_i\vec{V}_i$$
$$-\vec{\nabla}\cdot\left(\rho\sum_i\vec{V}_iY_ih_i\right)-\vec{\nabla}\cdot\left\{\rho\sum_i[Y_i\vec{V}_i(\vec{v}\cdot\vec{V}_i)+\frac{1}{2}Y_i\vec{V}_i(\vec{V}_i\cdot\vec{V}_i)]\right\}$$
$$+\frac{DP}{Dt}+\vec{\nabla}\cdot k\nabla T+\mu\Phi+\dot{Q}_V \qquad \text{(B.26)}$$

Notice that in the absence of diffusion ($\vec{V}_i=0$ for all i) the thermal energy equation reduces to

$$\rho\frac{D\hat{u}}{Dt}+P\vec{\nabla}\cdot\vec{v}=\vec{\nabla}\cdot k\nabla T+\mu\Phi+\dot{Q}_V$$

or

$$\rho\frac{Dh}{Dt}=\frac{Dp}{Dt}+\vec{\nabla}\cdot k\nabla T+\mu\Phi+\dot{Q}_V$$

as we would expect. These two equations apply to a single-component system.

In order to write equation (B.26) in terms of the excess enthalpy, we substitute equations (B.1) and (B.2) to get

$$\rho\frac{D}{Dt}(h^\circ+h_1)+\frac{1}{2}\rho\frac{D}{Dt}\left(\sum_i Y_i\vec{V}_i\cdot\vec{V}_i\right)=\vec{\nabla}\cdot\sum_i P_i\vec{V}_i$$
$$-\vec{\nabla}\cdot\left[\rho\sum_i\vec{V}_iY_i(h_i^\circ+h_{1,i})\right]-\vec{\nabla}\cdot\left\{\rho\sum_i[Y_i\vec{V}_i(\vec{v}\cdot\vec{V}_i)+\frac{1}{2}Y_i\vec{V}_i(\vec{V}_i\cdot\vec{V}_i)]\right\}$$
$$+\frac{DP}{Dt}+\vec{\nabla}\cdot k\nabla T+\mu\Phi+\dot{Q}_V$$

This can be expressed in a slightly different form using the continuity equation by writing

$$\rho\frac{Dh^\circ}{Dt}=\frac{\partial}{\partial t}(\rho h^\circ)+\vec{\nabla}\cdot(\rho\vec{v}h^\circ)-h^\circ\left[\frac{\partial\rho}{\partial t}+\vec{\nabla}\cdot(\rho\vec{v})\right]$$

Since the last term in the above equation is identically zero by the overall continuity equation, we get

$$\rho\frac{Dh^\circ}{Dt}=\frac{\partial}{\partial t}(\rho h^\circ)+\vec{\nabla}\cdot(\rho\vec{v}h^\circ)$$

Similarly,

$$\rho\frac{Dh_1}{Dt} = \frac{\partial}{\partial t}(\rho h_1) + \vec{\nabla}\cdot(\rho\vec{v'}h_1)$$

Substituting the above two equations into our thermal energy equation gives (after re-arranging terms)

$$\begin{aligned}\frac{\partial}{\partial t}(\rho h_1) + \vec{\nabla}\cdot(-k\nabla T + \rho\vec{v'}h_1) = \vec{\nabla}\cdot\sum_i P_i\vec{V}_i \\ -\left[\frac{\partial}{\partial t}(\rho h^\circ) + \vec{\nabla}\cdot\left(\rho\vec{v'}h^\circ + \rho\sum_i \vec{V}_i Y_i h_i^\circ\right)\right] \\ -\vec{\nabla}\cdot\left(\rho\sum_i \vec{V}_i Y_i h_{1,i}\right) + \frac{DP}{Dt} - \frac{1}{2}\rho\frac{D}{Dt}\left(\sum_i Y_i\vec{V}_i\cdot\vec{V}_i\right) \\ -\vec{\nabla}\cdot\left\{\rho\sum_i[Y_i\vec{V}_i(\vec{v'}\cdot\vec{V}_i) + \frac{1}{2}Y_i\vec{V}_i(\vec{V}_i\cdot\vec{V}_i)]\right\} + \mu\Phi + \dot{Q}_V\end{aligned}$$

Consider the first three terms in brackets on the right hand side of the above equation. Since

$$h_i^\circ = \text{constant for each } i$$

and

$$h^\circ = \textstyle\sum_i Y_i h_i^\circ$$

we can write

$$\begin{aligned}\frac{\partial}{\partial t}(\rho h^\circ) + \vec{\nabla}\cdot\left(\rho\vec{v'}h^\circ + \rho\sum_i \vec{V}_i Y_i h_i^\circ\right) = \\ = \sum_i\left\{h_i^\circ\left[\frac{\partial}{\partial t}(\rho Y_i) + \vec{\nabla}\cdot(\rho Y_i\vec{v'} + \rho Y_i\vec{V}_i)\right]\right\} \\ = \sum_i\left\{h_i^\circ\left[\frac{\partial}{\partial t}(\rho Y_i) + \vec{\nabla}\cdot\vec{n_i}\right]\right\}\end{aligned}$$

where $\vec{n_i}$ is the total mass flux given previously in equation (B.13). From the conservation of species [equation (6.28)],

$$r_i''' = \frac{\partial}{\partial t}(\rho Y_i) + \vec{\nabla}\cdot\vec{n_i}$$

where

$$r_i''' = \text{rate of production of the } i^{\text{th}} \text{ component } [\text{kg}/(\text{m}^3\cdot\text{s})]$$

we end up with

$$-\left[\frac{\partial}{\partial t}(\rho h^\circ) + \vec{\nabla}\cdot\left(\rho\vec{v}h^\circ + \rho\sum_i \vec{V}_i Y_i h_i^\circ\right)\right] = -\sum_i h_i^\circ r_i'''$$

If we define the dimensional quantity

$$Q_{\text{ch}} \equiv -\sum_i h_i^\circ r_i''' = \text{heat released by chemical reaction (calculated at temperature } T^\circ) \tag{B.27}$$

then the thermal energy equation becomes (after some rearrangement)

$$\begin{aligned}\frac{\partial}{\partial t}(\rho h_1) + \vec{\nabla}\cdot(-k\nabla T + \rho\vec{v}h_1) &= \frac{DP}{Dt} + Q_{\text{ch}} \\ -\vec{\nabla}\cdot\left(\rho\sum_i \vec{V}_i Y_i h_{1,i}\right) + \mu\Phi + \dot{Q}_V - \frac{1}{2}\rho\frac{D}{Dt}\left(\sum_i Y_i\vec{V}_i\cdot\vec{V}_i\right) \\ -\vec{\nabla}\cdot\left\{\rho\sum_i[Y_i\vec{V}_i(\vec{v}\cdot\vec{V}_i) + \frac{1}{2}Y_i\vec{V}_i(\vec{V}_i\cdot\vec{V}_i)]\right\} + \vec{\nabla}\cdot\sum_i P_i\vec{V}_i\end{aligned} \tag{B.28}$$

In order to use $\Gamma'_\phi = k'/\bar{c}'_p$ and $\phi' = \bar{c}'_p T'_1 = h'_1 = h'_{\text{excess}}$, we can write

$$\begin{aligned}\vec{\nabla}\cdot(-k\nabla T) &= \vec{\nabla}\cdot(-k\nabla T_1) = -\vec{\nabla}\cdot\left[\frac{k}{\bar{c}_p}\nabla(\bar{c}_p T_1) - \frac{kT_1}{\bar{c}_p}\nabla\bar{c}_p\right] \\ &= \vec{\nabla}\cdot\left[-\frac{k}{\bar{c}_p}\nabla h_1\right] + \vec{\nabla}\cdot\left[\frac{kT_1}{\bar{c}_p}\nabla\bar{c}_p\right]\end{aligned}$$

and use

$$\overline{Le} = \frac{\bar{\alpha}}{\mathcal{D}_{ij}} = \frac{k/\bar{c}_p}{\rho\mathcal{D}_{ij}} \tag{B.29}$$

so that by substituting equations (B.1), (B.8) and the above two equations into equation (B.28), we get

$$\frac{\partial}{\partial t}(\rho h_1) + \vec{\nabla}\cdot\left(-\frac{k}{\overline{c}_p}\nabla h_1 + \rho\vec{v}h_1\right) = \frac{DP}{Dt} + Q_{\text{ch}}$$
$$+\vec{\nabla}\cdot\left\{\rho\mathcal{D}_{ij}T_1\left[\sum_i(\overline{c}_{p_i}\nabla Y_i) - \overline{Le}\nabla\overline{c}_p\right]\right\}$$
$$+\mu\Phi + \dot{Q}_V - \frac{1}{2}\rho\frac{D}{Dt}\left(\sum_i Y_i\vec{V}_i\cdot\vec{V}_i\right)$$
$$-\vec{\nabla}\cdot\left\{\rho\sum_i[Y_i\vec{V}_i(\vec{v}\cdot\vec{V}_i) + \frac{1}{2}Y_i\vec{V}_i(\vec{V}_i\cdot\vec{V}_i)]\right\} + \vec{\nabla}\cdot\sum_i P_i\vec{V}_i \qquad \text{(B.30)}$$

All variables in equation (B.30) are dimensional. Note that we have assumed the binary diffusion coefficients, $\mathcal{D}_{ij}$, are equal for all species. If we denote

$$S'_\phi = \frac{DP'}{Dt'} + Q'_{\text{ch}} + \vec{\nabla}'\cdot\left\{\rho'\mathcal{D}'_{ij}T'_1\left[\sum_i(\overline{c}'_{p_i}\nabla' Y'_i) - \overline{Le}'\nabla'\overline{c}'_p\right]\right\}$$
$$+\mu'\Phi' + \dot{Q}'_V - \frac{1}{2}\rho'\frac{D'}{Dt'}\left(\sum_i Y'_i\vec{V}'_i\cdot\vec{V}'_i\right)$$
$$-\vec{\nabla}'\cdot\left\{\rho'\sum_i[Y'_i\vec{V}'_i(\vec{v}'_A\cdot\vec{V}'_i) + \frac{1}{2}Y'_i\vec{V}'_i(\vec{V}'_i\cdot\vec{V}'_i)]\right\} + \vec{\nabla}'\cdot\sum_i P'_i\vec{V}'_i \qquad \text{(B.31)}$$

then equation (B.30) becomes

$$\frac{\partial}{\partial t'}(\rho' h'_1) + \vec{\nabla}'\cdot\left(-\frac{k'}{\overline{c}_p}\nabla' h'_1 + \rho'\vec{v}'_A h'_1\right) = S'_\phi$$

The mass-weighted average velocity of the fluid mixture [$\vec{v}'$ (non-dimensional) or $\vec{v}'_A$ (dimensional)] is the same velocity as is used in the other conservation equations. Thus the above equation written in standard form [see equation (6.1)] using the mass-weighted average velocity components is

$$\frac{\partial}{\partial t'}(\rho' h'_1) + \frac{1}{r'}\frac{\partial}{\partial x'}\left[r'\left(\rho' u' h'_1 - \frac{k'}{\overline{c}_p}\frac{\partial h'_1}{\partial x'}\right)\right] +$$
$$+\frac{\partial}{\partial y'}\left(\rho' v' h'_1 - \frac{k'}{\overline{c}_p}\frac{\partial h'_1}{\partial y'}\right) = S'_\phi \qquad \text{(B.32)}$$

To make equation (B.32) dimensionless, multiply it by

$$\frac{t_*}{\rho_* c_{p_*} T_*} = \frac{L_*}{\rho_* U_* c_{p_*} T_*}$$

and use the nondimensional variables

$$h_1 = \frac{h_1'}{h_*} = \frac{h_1'}{c_{p_*} T_*}$$

and

$$\Gamma_\phi = \frac{k'/\overline{c}_p'}{\mu_*}$$

The result is

$$\frac{\partial}{\partial t}(\rho h_1) + \frac{1}{r}\frac{\partial}{\partial x}\left[r\left(\rho u h_1 - \frac{\mu_*/\rho_*}{U_* L_*}\frac{k'/\overline{c}_p'}{\mu_*}\frac{\partial h_1}{\partial x}\right)\right] + \frac{\partial}{\partial y}\left(\rho v h_1 - \frac{\mu_*/\rho_*}{U_* L_*}\frac{k'/\overline{c}_p'}{\mu_*}\frac{\partial h_1}{\partial y}\right) = \frac{t_*}{\rho_* c_{p_*} T_*} S_\phi' \tag{B.33}$$

Recognizing that

$$\frac{\mu_*/\rho_*}{U_* L_*} \equiv \frac{1}{Re_*}$$

the above equation is in the general form of equation (6.3),

$$\frac{\partial(\rho\phi)}{\partial t} + \frac{1}{r}\frac{\partial}{\partial x}\left[r\left(\rho u\phi - \frac{\Gamma_\phi}{Re_*}\frac{\partial\phi}{\partial x}\right)\right] + \frac{\partial}{\partial y}\left(\rho v\phi - \frac{\Gamma_\phi}{Re_*}\frac{\partial\phi}{\partial y}\right) = \frac{t_*}{\rho_* c_{p_*} T_*} S_\phi'$$

with

$$\phi = h_1 = \frac{h_1'}{c_{p_*} T_*} \qquad \text{and} \qquad \Gamma_\phi = \frac{k'/\overline{c}_p'}{\mu_*} \tag{B.34}$$

Appendix C

Derivation of Source Term For Species Equation With One-Step Chemical Reaction

In the current version of the computational model, chemical reactions are not included, and therefore the source term given in equation (6.31) is identically zero. That is,

$$S_\phi = \frac{t_*}{\rho_* Y_*}\left(r_i'''\right)' = \frac{t_*}{\rho_*}\left(r_i'''\right)' = 0$$

However, in future versions of the code incorporating chemical reactions, the source term for each species may be developed as follows. Consider a simple one-step chemical reaction

$$n_F F + n_O O \xrightarrow{k'} n_P P \tag{C.1}$$

where

F, O, P $\equiv$ fuel, oxidant, products species

n_F, n_O, n_P $\equiv$ moles of fuel, oxidant, and products in reaction

k' $\equiv$ specific rate constant

$n = n_F + n_O$ $\equiv$ order of reaction

Then the rate of production of fuel [units: kg/(m^{3}s)] is

$$\left(r_F'''\right)' = \frac{d[F]}{dt}\hat{M}_F' = -n_F k'[F]^{n_F}[O]^{n_O}\hat{M}_F' \tag{C.2}$$

where $\hat{M}_F'$ is the dimensional molecular weight of the fuel and the single brackets (e.g., $[F]$) denotes concentration, C_i'. The concentration C_i' is given by

$$C_i' = \frac{\rho_{\text{mix}}' Y_i'}{\hat{M}_i'} = \left(\frac{\rho_* Y_*}{\hat{M}_*}\right)\left(\frac{\rho Y_i}{\hat{M}_i}\right) \tag{C.3}$$

where $Y_* = 1$.

The specific rate constant is given by the Arrhenius expression

$$k' = A' \exp(-E_a'/\mathcal{R}'T') \tag{C.4}$$

where A' is the pre-exponential factor (representing the number of collisons per second), E_a' is the activation energy, $\mathcal{R}'$ is the universal gas constant, and T' is the absolute temperature.

Substituting equations (C.3) and (C.4) into equation (C.2) gives

$$\left(r_F'''\right)' = -n_F \rho_*^n \hat{M}_*^{1-n}\hat{M}_F A' \exp(-E_a'/\mathcal{R}'T')\left(\frac{\rho Y_F}{\hat{M}_F}\right)^{n_F}\left(\frac{\rho Y_O}{\hat{M}_O}\right)^{n_O} \tag{C.5}$$

Similarly, for the oxidant we get

$$\left(r_O'''\right)' = -n_O \rho_*^n \hat{M}_*^{1-n}\hat{M}_O A' \exp(-E_a'/\mathcal{R}'T')\left(\frac{\rho Y_F}{\hat{M}_F}\right)^{n_F}\left(\frac{\rho Y_O}{\hat{M}_O}\right)^{n_O} \tag{C.6}$$

The reaction rate for the products is

$$\left(r_P'''\right)' = n_P \rho_*^n \hat{M}_*^{1-n}\hat{M}_P A' \exp(-E_a'/\mathcal{R}'T')\left(\frac{\rho Y_F}{\hat{M}_F}\right)^{n_F}\left(\frac{\rho Y_O}{\hat{M}_O}\right)^{n_O} \tag{C.7}$$

As can be seen from equations (C.5)-(C.7), the reaction rates for fuel, oxidant, and products differ only by a pre-exponential factor.

In the nondimensional source term from the energy equation, we had [equations (6.48) and (B.27)]:

$$\frac{Q'_{\text{ch}} t_*}{\rho_* c_{p_*} T_*} = -\frac{t_*}{\rho_* c_{p_*} T_*} \sum_i \left(h_i^o r_i''' \right)' = -\sum_i \left(\frac{h^{o'}}{c_{p_*} T_*} \right) \left(\frac{\left(r_F''' \right)' t_*}{\rho_*} \right)$$

From this one recognizes that we should write

$$h_i^o = \frac{h^{o'}}{c_{p_*} T_*} \quad \text{and} \quad r_i''' = \frac{\left(r_F''' \right)' t_*}{\rho_*} \tag{C.8}$$

Now if we define

$$\text{PREXP} \equiv A' \rho_*^{n-1} \hat{M}_*^{1-n} t_* \quad \text{and} \quad \text{EART} \equiv -E'_a / \mathcal{R}' T_* \tag{C.9}$$

then the species source term equations become

$$S_{\phi,F} = \frac{t_*}{\rho_*} \left(r_F''' \right)' = -n_F \hat{M}_F \cdot \text{PREXP} \cdot \exp\left(\frac{\text{EART}}{T} \right) \left(\frac{\rho Y_F}{\hat{M}_F} \right)^{n_F} \left(\frac{\rho Y_O}{\hat{M}_O} \right)^{n_O}$$

$$S_{\phi,O} = -n_O \hat{M}_O \cdot \text{PREXP} \cdot \exp\left(\frac{\text{EART}}{T} \right) \left(\frac{\rho Y_F}{\hat{M}_F} \right)^{n_F} \left(\frac{\rho Y_O}{\hat{M}_O} \right)^{n_O}$$

$$S_{\phi,P} = n_P \hat{M}_P \cdot \text{PREXP} \cdot \exp\left(\frac{\text{EART}}{T} \right) \left(\frac{\rho Y_F}{\hat{M}_F} \right)^{n_F} \left(\frac{\rho Y_O}{\hat{M}_O} \right)^{n_O}$$

These can be put into a common form

$$S_{\phi,i} = B_i \cdot \text{PREXP} \cdot \exp\left(\frac{\text{EART}}{T} \right) \left(\frac{\rho Y_F}{\hat{M}_F} \right)^{n_F} \left(\frac{\rho Y_O}{\hat{M}_O} \right)^{n_O} \tag{C.10}$$

where

$$B_F = -n_F \hat{M}_F, \quad B_O = -n_O \hat{M}_O, \quad \text{and} \quad B_P = n_P \hat{M}_P \tag{C.11}$$

These coefficients B_i may be thought of as the mass of species i produced in the reaction described by equation (C.1). As described previously, these source term equations may be used in the Q_{ch} contribution to the energy equation source term when chemical reactions are included in the model.

References

[1] Abramzon, B., Edwards, D. K., and Sirignano, W. A., "Transient, Stratified, Enclosed Gas and Liquid Behavior with Concentrated Heating from Above," *J. Thermophysics*, Vol. 1, No. 4, October 1987, pp. 355–364.

[2] Aggarwal, S. K., Iyengar, J., and Sirignano, W. A., "Enclosed Gas and Liquid with Nonuniform Heating from Above," *Int. J. Heat Mass Transfer*, Vol. 29, 1986, pp. 1593–1604.

[3] Patankar, S. V. Numerical Heat Transfer and Fluid Flow, Hemisphere and McGraw-Hill, New York (1980).

[4] Glassman, I. and Dryer, F. L., "Flame Spread Across Liquid Fuels," *Fire Safety Journal*, Vol. 3, 1980/1981, pp. 123–138.

[5] Kanury, A. M., "Liquid Pool Burning," Chapter VI in Combustion Experiments in a Zero-Gravity Laboratory, Vol. 73 of Progress in Astronautics and Aeronautics, New York, 1981.

[6] Murad, R. J., Lamendola, J., Isoda, H., and Summerfield, M., "A Study of Some Factors Influencing the Ignition of a Liquid Fuel Pool," *Combustion and Flame*, Vol. 15, 1970, pp. 289–298.

[7] Glassman, I., Sirignano, W. A., and Summerfield, N., "Physics of Flames," Final Report, U.S. Army Ballistic Research Laboratories Contract DAA 05-68-C-0450, Princeton University, Princeton, New Jersey, 1970.

[8] Sirignano, W. A. and Glassman, I., "Flame Spreading Above Liquid Fuels: Surface-Tension-Driven Flows," *Comb. Sci. Tech.*, Vol. 1, 1970, pp. 307–312.

[9] Torrance, K. E., "Subsurface Flows Preceding Flame Spread Over a Liquid Fuel," *Comb. Sci. Tech.*, Vol. 3, 1971, pp. 113–143.

[10] Torrance, K. E. and Mahajan, R. L., "Surface Tension Flows Induced by a Moving Thermal Source," *Comb. Sci. Tech.*, Vol. 10, 1975, pp. 125–136.

[11] Ostrach, S., "Low-Gravity Fluid Flows," *Ann. Rev. Fluid Mech.*, Vol. 14, 1982, pp. 313–345.

[12] Furuta, M., Humphrey, J. A. C., and Fernandez-Pello, A. C., "Prediction of Flame Spread Hydrodynamics Over Liquid Fuel," *Physico-Chemical Hydrodynamics*, Vol. 6, No. 4, 1985, pp. 347–372.

[13] Ostrach, S., Kamotani, Y., and Jacobsen, T., "Science Requirements Document for Surface Tension Driven Convection Experiment in Reduced Gravity," May 1985.

[14] Van Doormaal, J. P. and Raithby, G. D., "Enhancements of the SIMPLE Method for Predicting Incompressible Fluid Flows," *Numerical Heat Transfer*, Vol. 7, 1984, pp. 147–163.

[15] Bird, R. B., Stewart, W. E., and Lightfoot, E. N., Transport Phenomena, John Wiley & Sons, New York, 1960.

[16] Edwards, D. K., Denny, V. E., and Mills, A. F., Transfer Processes, Hemisphere Publishing Corp., New York, 1979.

[17] De Vahl Davis, G. and Jones, I. P., "Natural Convection in a Square Cavity: A Comparison Exercise," *Numerical Methods in Thermal Problems*, edited by R. W. Lewis et al., Pineridge Press, Swansea, Wales, 1981, pp. 553–572.

[18] The American Society of Heating, Refrigerating, and Air-Conditioning Engineers, Inc., ASHRAE Handbook 1985 Fundamentals.

[19] Morrison, G. and McLinden, M., NBS Technical Note.

[20] Ostrach, S. and Kamotani, Y., "Surface Tension Driven Experiment Preliminary Requirements Review," February 1988.

[21] Greenberg, P. and Lai, C., manuscript in preparation.

[22] Williams, F. A., Combustion Theory, 2nd ed., Benjamin/Cummings Publishing Company, Inc., Menlo Park, California, 1985.

NASA
National Aeronautics and Space Administration

Report Documentation Page

1. Report No.	2. Government Accession No.	3. Recipient's Catalog No.
NASA CR-182256		

4. Title and Subtitle	5. Report Date
Experiment Plans to Study Preignition Processes of a Pool Fire in Low Gravity	March 1989
	6. Performing Organization Code

7. Author(s)	8. Performing Organization Report No.
David N. Schiller	None
	10. Work Unit No.
	674-22-05

9. Performing Organization Name and Address	11. Contract or Grant No.
University of California—Irvine Irvine, California 92717	NAG3-627
	13. Type of Report and Period Covered
	Contractor Report Final

12. Sponsoring Agency Name and Address	14. Sponsoring Agency Code
National Aeronautics and Space Administration Lewis Research Center Cleveland, Ohio 44135-3191	

15. Supplementary Notes

Project Manager, Howard D. Ross, Space Experiments Division, NASA Lewis Research Center. This report was a thesis submitted in partial fulfillment of the requirements for the degree Master of Science in Mechanical Engineering to the University of California—Irvine in 1988.

16. Abstract

Science requirements are specified to guide experimental studies of transient heat transfer and fluid flow in an enclosure containing a two-layer gas-and-liquid system heated unevenly from above. Specifications are provided for experiments in three separate settings: (a) a normal gravity laboratory, (b) the NASA-LeRC Drop towers, and (c) a space-based laboratory (e.g., Shuttle, Space Station). A rationale is developed for both minimum and desired requirement levels. The principal objective of the experimental effort is to validate a computational model of the enclosed liquid fuel pool during the preignition phase and to determine via measurement the role of gravity on the behavior of the system. Preliminary results of single-phase normal gravity experiments and simulations are also presented.

17. Key Words (Suggested by Author(s))	18. Distribution Statement
Microgravity Pool fires Combustion Thermocapillarity	Unclassified – Unlimited Subject Category 29

19. Security Classif. (of this report)	20. Security Classif. (of this page)	21. No of pages	22. Price*
Unclassified	Unclassified	128	A07

NASA FORM 1626 OCT 86

*For sale by the National Technical Information Service, Springfield, Virginia 22161